Agricultural and Forest Meteorology 306 (2021) 108402

Contents lists available at ScienceDirect

Agricultural and Forest Meteorology

journal homepage: www.elsevier.com/locate/agrformet

The effect of static pressure-wind covariance on vertical carbon dioxide exchange at a windy subalpine forest site

Sean P. Burns [*,a,b], John M. Frank [c], William J. Massman [c], Edward G. Patton [b], Peter D. Blanken [a]

[a] Department of Geography, University of Colorado, Boulder, USA
[b] National Center for Atmospheric Research, Boulder, Colorado, USA
[c] US Forest Service, Rocky Mountain Research Station, Fort Collins, Colorado, USA

ARTICLE INFO

Keywords:
Turbulent pressure transport
Net ecosystem exchange of CO_2
Wind profile
Subalpine forest ecosystem

ABSTRACT

Accounting for turbulent temperature and water vapor fluctuations on the vertical flux of CO_2 measured by an open-path infrared gas analyzer are commonly known as the Webb–Pearman–Leuning (WPL) corrections. Static pressure fluctuations also affect air sample density, but the magnitude and effect of these changes on CO_2 flux is not usually considered. In our study, the turbulent static pressure p and the vertical wind component w covariance $\overline{w'p'}$ from just-above a Rocky Mountain subalpine forest are examined. The magnitude of $\overline{w'p'}$ was highly correlated to the mean horizontal wind speed U with similar characteristics during the daytime and nighttime. The pressure term was calculated from $\overline{w'p'}$ and compared to other terms in the equation for the vertical net ecosystem exchange of CO_2 (NEE). We found the following: (1) for $U \lesssim 6$ m s^{-1}, the pressure term was small, (2) as U increased beyond 6 m s^{-1}, the pressure term became more and more important reaching a magnitude of ≈ 2 μmol m^{-2} s^{-1} at U of 12 m s^{-1} (for leaf area index LAI ≈ 2.6 m^2 m^{-2}), (3) for a more dense forest (LAI ≈ 4.8 m^2 m^{-2}), the magnitude of the pressure term at U of 12 m s^{-1} was ≈ 1 μmol m^{-2} s^{-1}, or about half the open forest value, and (4) based on 14 years of measurements, the interannual mean and standard deviation of the yearly cumulative pressure and NEE terms were -32.8 ± 24.5 g C m^{-2} year^{-1} and -147.4 ± 231.7 g C m^{-2} year^{-1}, respectively. Therefore, on average, including the pressure term in the NEE calculation reduces the annual carbon uptake by the GLEES forest from 147.4 g C m^{-2} year^{-1} to 114.6 g C m^{-2} year^{-1}. This implies that carbon uptake by forests in windy locations that ignore the pressure term can be overestimated by as much as 20%. However, the year-to-year variability of both NEE and the pressure term was large due to changes in the forest structure and LAI from beetle attack and tree die-off. Finally, we present results from sensor-manipulation experiments examining the effect of tilting the quad-disk pressure ports on the turbulent static pressure.

1. Introduction

Atmospheric static pressure fluctuations just-above a forest are affected by density changes to the air column above a location (i.e., hydrostatic changes) as well as vertical turbulent wind fluctuations interacting with the mean wind shear, the interaction of turbulence with itself, and the vertical gradient of temperature fluctuations (Albertson et al., 1998; Bradshaw and Koh, 1981; Katul et al., 1996; Patton and Katul, 2009; Schols and Wartena, 1986; Shaw et al., 1990). In low winds, the hydrostatic changes dominate, while in high winds the turbulent interactions became more important (Bedard et al., 1992). Coherent structures above a forest play an important role in shaping the interaction between static pressure and the wind field (Shaw and Zhang, 1992).

Ecosystem-scale fluxes of mass, momentum, and energy are typically measured using micrometeorological techniques over a 30-min time period (e.g., Aubinet et al., 2012; Baldocchi et al., 1988). Eddy covariance measurement of the vertical CO_2 flux is known to be influenced by the covariance of vertical wind and static pressure $\overline{w'p'}$, especially in windy locations (Massman and Lee, 2002). At a 26-m tall mixed-forest site in China, Zhang et al. (2011) showed that the so-called pressure correction term was on the order of 20% of the annual net ecosystem exchange of CO_2 (NEE). Burba et al. (2012) looked at nine different sites

* Corresponding author.
E-mail addresses: sean@ucar.edu, sean.burns@colorado.edu (S.P. Burns), john.frank@usda.gov (J.M. Frank), william.j.massman@usda.gov (W.J. Massman), patton@ucar.edu (E.G. Patton), peter.blanken@colorado.edu (P.D. Blanken).

https://doi.org/10.1016/j.agrformet.2021.108402
Received 28 August 2020; Received in revised form 10 March 2021; Accepted 14 March 2021
Available online 24 May 2021

(from grasslands to forests) and concluded that the effects of pressure fluctuations on NEE were typically small, but could be important for long-term cumulative sums of NEE at windy sites. In general, most studies do not account for the effect of pressure fluctuations on NEE (e.g., Polonik et al., 2019; Wang et al., 2016), which is primarily related to the challenges of measuring turbulent static pressure (see Section 3.2).

The theoretical underpinnings of NEE in relation to eddy covariance measurements and control volume analysis has been described elsewhere (e.g., Finnigan et al., 2003; Massman and Lee, 2002). If we neglect vertical and horizontal advection, and any dispersive fluxes, the equation describing NEE [μmol m^{-2} s^{-1}] in the vertical z direction is,

$$\mathrm{NEE} = \underbrace{\int_0^{h_f} \frac{\partial \overline{\rho_c}}{\partial t} dz}_{\mathrm{CO_2\ Storage}} + \underbrace{\overline{w'\rho_c'}}_{\mathrm{Covariance}} - \underbrace{\overline{\rho_c}(1+\overline{\chi_v})\frac{\overline{w'p_a'}}{\overline{p_a}}}_{\mathrm{Pressure\ Term}} + \underbrace{\overline{\rho_c}(1+\overline{\chi_v})\frac{\overline{w'T'}}{\overline{T}}}_{\mathrm{Temperature\ Term}} + \underbrace{\mu_v \frac{\overline{\rho_c}}{\overline{\rho_a}} \overline{w'\rho_v'}}_{\mathrm{Water\ Vapor\ Term}}, \quad (1)$$

where ρ_c, ρ_v, and ρ_a are the density of CO_2, water vapor, and dry air [kg m^{-3}], respectively. The molecular weight of CO_2 (44.01 g mole^{-1}) is used to convert ρ_c from kg m^{-3} to μmol m^{-3}. The vertical wind component is w [m s^{-1}], T is temperature [K], h_f is the height of the flux measurement, $\mu_v = 1.608$ is the ratio of the molecular weight of dry air to that of water, χ_v is the mole fraction of water vapor [mol H_2O mol^{-1}], and p_a is static pressure [Pa]. In Eq. (1), an overbar signifies the time-averaged mean and the prime are turbulent fluctuations about the mean over a 30-min averaging period (for simplicity, the overbar will not be used for mean values beyond Eq. (1)). For our study, an upper-case P represents the mean static pressure (i.e., $P \equiv \overline{p_a}$, usually called the barometric pressure) and a lower-case p is the turbulent static pressure. We assume the 30-min averaging period captures most of the low-frequency and all of the turbulent contributions to the flux (e.g., Vickers and Mahrt, 2003). The names of the various terms are shown above or below each term on the right-hand side of Eq. (1). We have neglected any higher-order terms which are discussed elsewhere (e.g., Burba et al., 2012; Fuehrer and Friehe, 2002; Massman and Lee, 2002). The water vapor and temperature terms are typically referred to as the Webb–Pearman–Leuning (WPL) corrections (Webb et al., 1980). Positive NEE indicates that the ecosystem is a net source of CO_2 from the land to the atmosphere. In our study, we focus on the pressure term. Unlike the WPL temperature and water vapor terms, positive $\overline{w'p'}$ decreases NEE, whereas negative $\overline{w'p'}$ increases NEE.

It is important to realize that the variables used in Eq. (1) depend upon whether an open-path or closed-path infrared gas analyzer (IRGA) is used to measure the fluctuations of CO_2 and H_2O (e.g., Haslwanter et al., 2009; Leuning and Judd, 1996; Massman, 2004). For an open-path IRGA, the atmospheric variables (T, ρ_v, and p) that exist within the instrument path are needed for Eq. (1). In some cases, the heat generated by the instrument affects the temperature within the IRGA path, which requires the so-called Burba or self-heating correction (Burba et al., 2008; Frank and Massman, 2020). To account for the self-heating, $\overline{w'T'}$ in Eq. (1), should be based on temperature fluctuations within the IRGA sampling volume, not within the (unheated) sampling volume of the co-located sonic anemometer.

In closed-path IRGAs, the water vapor term can be calculated from coincident high-frequency water vapor measurements within the sample cell to directly convert ρ_c to CO_2 dry mole fraction χ_c (e.g., Burba et al., 2012; Kowalski and Serrano-Ortiz, 2007; Nakai et al., 2011, among others). This technique uses the dilution properties of water vapor on the CO_2 measurement, though time lag differences between CO_2 and H_2O due to different constituent flow rates should be considered to calculate latent heat flux (e.g., Ibrom et al., 2007). For closed-path IRGAs, the temperature term is typically accounted for by either a fast-response measurement of cell temperature or through attenuation of the temperature fluctuations by the inlet and tubing (Burba et al., 2012; Leuning and Moncrieff, 1990; Massman, 2004). Nakai et al. (2011) showed that the covariance between w and pressure fluctuations in the closed-path sample cell was significant in high-wind near-neutral conditions. They used $\overline{w'p'_{\mathrm{cell}}}$ to determine the pressure term in Eq. (1) and correct a CO_2 density measurement to produce a CO_2 flux that compared well with the calculated dry mole fraction CO_2 flux.

Our study examines above-canopy (at $z \approx 1.5h$, where h is canopy height) co-located measurements of turbulent wind, static pressure fluctuations (using a Nishiyama-Bedard quad-disk pressure probe), and CO_2/H_2O from an open-path IRGA at the Glacier Lakes Ecosystem Experiments Site (GLEES) subalpine forest (Frank et al., 2014). The pressure measurements at GLEES started in January 2000 and we use the long-term record of $\overline{w'p'}$ to evaluate the effect of the pressure term on calculated NEE. During the measurement period, the forest surrounding the GLEES site suffered from a spruce beetle attack which killed most of the older, larger spruce trees and changed the forest structure. This has affected NEE (Frank et al., 2014), water vapor fluxes (Frank et al., 2019), and the mean wind profile (Chu et al., 2018). Our study examines the sensitivity of $\overline{w'p'}$ to such changes.

Forests exert primary control on the exchange of energy, water, carbon dioxide, and chemical species between the ground and atmosphere (Bonan, 2008; Finnigan, 2000; Raupach, 1987; Raupach et al., 1996; Raupach and Thom, 1981). Depending on their density, canopy elements often inhibit the interaction between above-canopy air and air in the subcanopy. Pressure is therefore thought to be an important mechanism which controls subcanopy air motion and turbulence (e.g., Baldocchi and Meyers, 1991; Dwyer et al., 1997; Holland, 1989; Shaw et al., 1990; Shaw and Zhang, 1992). Mixing of above-canopy air with subcanopy air is primarily achieved by canopy-scale coherent eddies created near the canopy top (at the inflection point in the vertical wind profile) that eject air from the subcanopy followed by a stronger sweep of downward-moving air into the subcanopy. Because the sweep and ejection motions associated with coherent structure above and within a forest occur within several seconds of each other, the magnitude and sign of a 30-min covariance of $\overline{w'p'}$ can be very sensitive to small temporal lags between the wind and pressure measurement (Shaw et al., 1990; Shaw and Zhang, 1992). With open-path instruments, lags exist because of the horizontal and vertical spatial separation between sensors (Horst and Lenschow, 2009), changes in wind speed and wind direction, as well as any electronic or systematic delays within the instruments or data system.

The paper is organized as follows: Section 2 describes the site, Section 3 has details about the instruments, the data processing, and our analysis methods, and Section 4 describes power spectra (Section 4.3), the coherence/phase between the wind and pressure measurements (Section 4.4), as well as the sensitivity of $\overline{w'p'}$ to time lags (Sections 4.5 and 4.6). The effect of stability on $\overline{w'p'}$ and comparisons with previous research is in Section 4.8. The pressure term is compared to other terms in the NEE equation at both the diel (Section 4.9) and annual (Section 4.10) time scales. The effect of measurement location and forest structure changes on the pressure term are discussed in Sections 4.11 and 4.12. Summary and conclusions are in Section 5. The appendices present: the method used to measure the systematic time lag between the pressure and wind (Appendix A), results from a sensor manipulation experiment that examines the effect of tilting the quad-disk port on the measured static pressure and $\overline{w'p'}$ (Appendix B), and justification for an ad-hoc correction applied to the WPL temperature term (Appendix C).

2. GLEES site description

The Glacier Lakes Ecosystem Experiments Site (GLEES; http://ameriflux.lbl.gov) is in a subalpine forest located in the Medicine Bow National Forest of the Rocky Mountains in southeastern Wyoming.

Table 1
Instrumentation and measurements relevant to our study at the GLEES AmeriFlux Site. Sensor heights are the distance above the ground.

Measured Variables[a]	Sensor type	Manufacturer[b] make/model	Serial No.	Sensor Resolution	Sensor Height [m]	Deployment Dates[c]	Reference / Additional Comments
Low-Frequency Pressure (P)	Diaphragm (Capacitive)	R. M. Young, 61202V	BP03468	10 Pa	22.65	Dec 2010 – present	R.M. Young Company (2001); the inlet port is an R. M. Young (model 61002). Prior to 2010, an A.I.R AIR-AB-2AX (Intellisensor II) sensor was used without any inlet port.
Turbulent Pressure (p)	Capsule (Differential Transducer)	Furness, FCO44	950329[d]	0.001 Pa (Transducer B)	27.1, 22.65	Nov 1999 – Oct 2003, Nov 2004 – Sep 2017	Furness Controls Limited (2008); also, see Sect. 3.3; the inlet port was usually a Qualimetrics Nishiyama-Bedard quad-disk.
3D Wind Components (u, v, w, T_s)	Sonic Anemometer	ATI, SATI/3Vx	971204[e], 971202, 971204	u, v, $w = 0.01$ m s^{-1}; $T_s = 0.01$ °C	27.1, 22.65, 6.5	Nov 1999 – Jan 2006, Oct 2004 – present, Oct 2012 – present	Applied Technologies (2016)
Turbulent CO_2 & H_2O[f] (ρ_c, ρ_v)	Infrared Gas Analyzer (IRGA)	NOAA IRGA, LI-COR LI-7500	2, 15; 75–0235, 75–1259, 75–1751	$\rho_c = 0.0001$ mg m^{-3}; $\rho_v = 0.001$ mg m^{-3}	27.1, 22.65	Nov 1999 – Jan 2006, Oct 2004 – present	LI-COR Inc. (2004), Frank and Massman (2020)

[a] Low-frequency (barometric) pressure is designated as P, whereas p refers to higher-frequency (turbulent) pressure; 3D wind components are measured with three dimensional sonic anemometer-thermometers where u, v, w, and T_s refer to the planar-fit streamwise, crosswind and vertical wind components, and sonic temperature, respectively. P was sampled at 0.5 Hz except in July 2017 when it was sampled at 1 Hz; all other variables were sampled at 20 Hz.

[b] Acronyms used: ATI: Applied Technologies Inc., Longmont, CO 80501 (http://www.apptech.com/); CSI: Campbell Scientific, Inc., Logan, UT 84321 (http://www.campbellsci.com); Furness: Furness Controls, Ltd., Bexhill-on-Sea, England TN39 3LG (http://www.furness-controls.com/); LI-COR: LI-COR Biosciences, Lincoln, NE 68504 (www.licor.com).

[c] Deployment dates refer to this particular instrument at this particular location.

[d] Transducer B was destroyed by a lightning strike in September, 2017. A second Furness FCO44 pressure transducer (Transducer A, SN 9301150) was used in the quad-disk manipulation experiments described in Appendix B.

[e] At times, SATI/3Vx SN 971202 was also used on the US-GBT tower.

[f] The NOAA IRGAs (SN 2 and 15) were the primary IRGAs used on the US-GBT tower, while LI-COR LI-7500s (SN 75–0235, 75–1259 and 75–1751) were mostly used on the US-GLE scaffold. The IRGA resolutions listed are for the LI-7500. Each IRGA was used during different periods on each tower. The list of IRGAs and dates used at US-GBT are: **SN 2**: Aug 2000 to Dec 2000, Jul 2002 to Sep 2002, Sep 2003 to Mar 2005, Dec 2005 to Jan 2006; **SN 15**: No. 1999 to Aug 2000, Dec 2000 to Jul 2002, Aug 2005 to Dec 2005; **SN 75–0235**: No. 2001 to Apr 2002, Jun 2002 to Oct 2003. The list of IRGAs and dates used at US-GLE are: **SN 75–0235**: Oct 2004 to Jan 2006, Mar 2006 to Jul 2007, Jul 2008 to Jul 2009, Jun 2010 to Mar 2011, Jun 2014 to Aug 2014; **SN 15**: Jan 2006 to Mar 2006; **SN 75–1259**: Jul 2007 to Jul 2008, Jul 2009 to Jun 2010; **SN 75–1751**: Mar 2011 to Jun 2014, Aug 2014 to present. Further details are in Frank and Massman (2020).

In the 1990s and early 2000s, flux measurements at GLEES were made at 27.1 m above the ground from the triangular-type Brooklyn Lakes tower (Massman and Clement, 2004; Zeller and Nikolov, 2000). For our study, we identify this location as site US-GBT (Massman and Frank, 1991–2006) and use static pressure data collected between years 2000 and late 2003 (at which time measurement errors occurred). In contrast, wind measurements were collected at US-GBT starting in 2000 and continued until the tower was removed in early 2006.

The US-GLE scaffold (Massman and Frank, 2004–present) has been used since October 2004, with above-canopy flux measurements made at 22.65 m above the ground (Frank et al., 2014). The US-GLE scaffold (41° 21′ 59.52″ N, 106° 14′ 23.82″ W, Elevation: 3190 m) is around 85 m north and 23 m west of the US-GBT tower. A satellite photo shows the patchiness of the GLEES forest and the positions of the two measurement locations (Fig. S1 in the supplementary material). The US-GBT tower was in a small clearing, whereas the US-GLE scaffold was located near/within a cluster of trees. Because US-GLE and US-GBT were so close together, we will use the term GLEES when discussing features common to both sites. Photos of the US-GBT tower and US-GLE scaffold along with corresponding instrumentation are shown in Fig. S2 within the supplementary material. We use the period when US-GBT and US-GLE were both collecting turbulent wind data (late 2004 to early 2006) to evaluate measurement differences between the two locations.

GLEES is within a heterogeneous forest of Engelmann spruce (*Picea engelmannii*) and subalpine fir (*Abies lasiocarpa*) comprised with trees of varying ages and heights. Starting around 2008 a spruce beetle outbreak decimated the GLEES forest (Frank et al., 2014), causing 75–85% mortality of the forested basal area (Fornwalt and Negron, 2010, unpublished data; Speckman et al., 2015). The two-sided leaf area index LAI at GLEES was reduced from a pre-beetle value of 4.7-4.9 to around 2.6 m^2 m^{-2} by around 2011 (Frank et al., 2019). In general, the forest has stem densities between 1330–2930 trees ha^{-1} with a wide range of tree sizes (mean diameter = 0.2 m, maximum diameter at breast height > 1 m), and heights (median = 7 m, inner quartile range = 8 m, maximum > 30 m, though trees near the US-GLE scaffold generally do not exceed 18 m) (Bradford et al., 2008, Fornwalt, 2010, unpublished data). The larger values in these ranges are representative of the forest prior to the beetle attack. West of the measurement locations is a gentle 4% slope downhill towards a streambed 0.5 km away, beyond which the slope rises at a 6% grade. The daytime and nighttime wind direction at GLEES is consistently out of the west. Further details about the GLEES site can be found in Musselman (1994) and Frank et al. (2014, 2019).

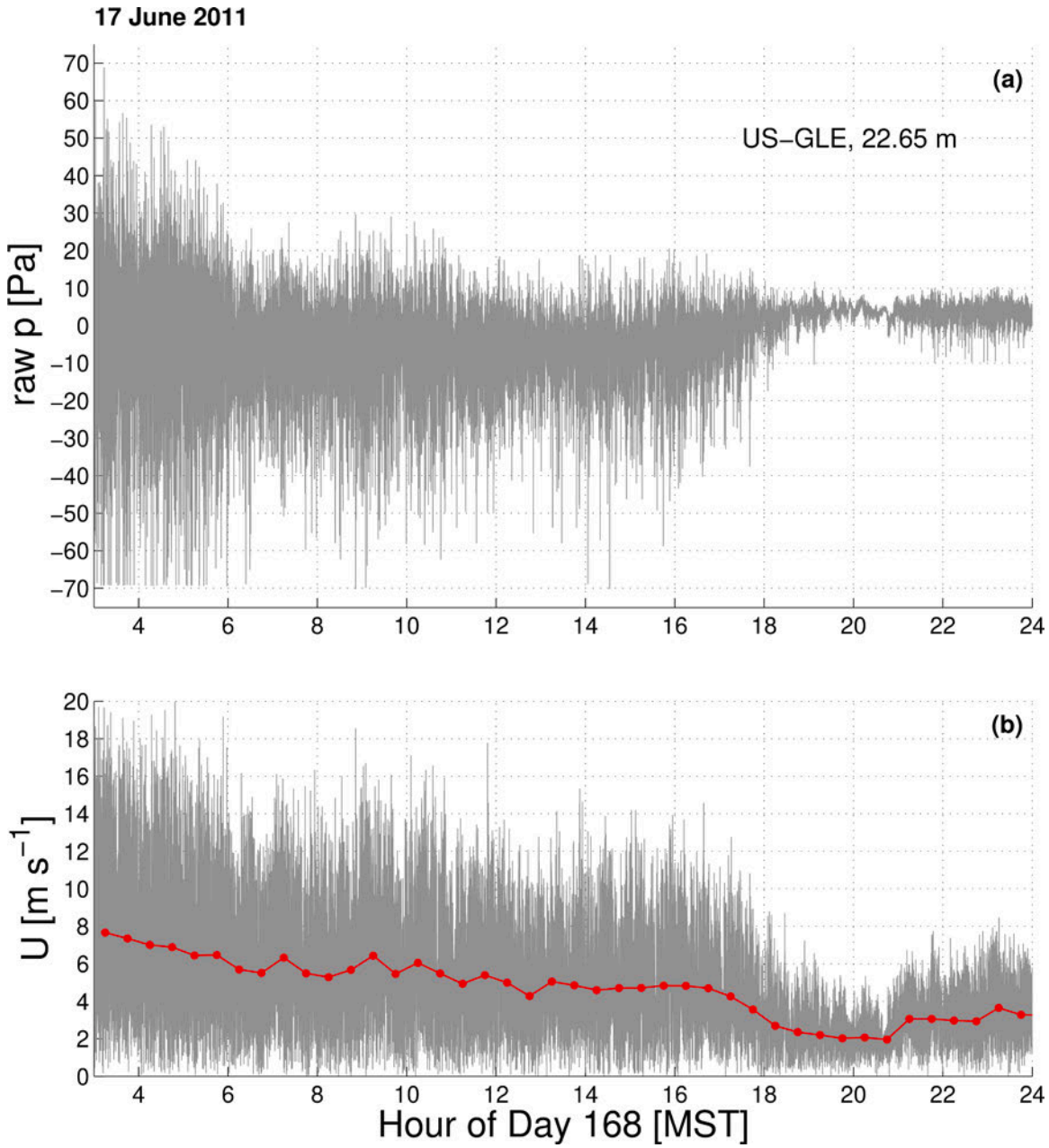

Fig. 1. Time series from the GLEES scaffold (US-GLE) on 17 June 2011 of above-canopy: **(a)** 20-Hz raw turbulent static pressure p_{raw}, and **(b)** 20-Hz horizontal wind speed U with 30-min mean values shown in red. In **(a)**, clipping of p_{raw} is apparent early in the time series (at a value of $p_{raw} \approx -70$ Pa) and a correction factor of 1.8 has been applied to account for the voltage divider; issues related to clipping and data processing are discussed in Section 3.3. (For interpretation of the references to color in this figure legend, the reader is referred to the web version of this article.)

3. Instrumentation and data processing

3.1. Wind measurements

Above-canopy wind and turbulence was measured with a 3-D sonic anemometer (Applied Technologies, model SATI/3Vx) mounted at 27.1 m on the US-GBT tower and 22.65 m on the US-GLE scaffold (Table 1). The 3Vx-probe includes a transducer shadowing correction algorithm (Kaimal, 1978). On the US-GBT tower, wind data were logged at 20 Hz using the ATI datapacker. On the US-GLE scaffold, the data system was changed to a Campbell Scientific CR3000 data logger in early 2009 (see Section 3.3 for details). To accommodate the primary wind direction at GLEES (i.e., from ≈ 280 degrees), the US-GBT and US-GLE booms were oriented toward the west at 270 degrees from true north. The planar-fit method (e.g., Wilczak et al., 2001) was used to convert the wind variables from the sonic anemometer coordinate system to the streamwise u, crossstream v, and vertical w wind coordinate system.

3.2. Static pressure measurement challenges

The atmosphere is a cacophony of sound and pressure-related phenomena. Everything from severe storms, to topography, to ocean waves generate atmospheric sound waves that exist just below the limit of human hearing (i.e., at frequencies smaller than around 20 Hz). These phenomena are called infrasound (e.g., Bedard and Georges, 2000; Gossard and Hooke, 1975; Hedlin et al., 2012; Le Pichon et al., 2010; Subramanian and Muschinski, 2011). In the infrasound community, the generation of static pressure fluctuations due to wind fluctuations masks

the weaker infrasound signals and is referred to as "wind-noise". Therefore, infrasound measurements use various filters and spatial-averaging techniques to try to eliminate (or minimize) the effect of wind fluctuations on the measured pressure (e.g., Raspet et al., 2019; Walker and Hedlin, 2010).

To correctly measure turbulent static pressure requires a proper static pressure port coupled to a transducer capable of covering a large signal range; as described by Wilczak and Bedard (2004), the turbulent fluctuations can be as small as 1 Pa with a mean atmospheric pressure on the order of 10^5 Pa. A turbulent pressure-measurement system needs fast time response and precision, but does not need to measure the low-frequency pressure. In contrast, a barometer only measures the low-frequency atmospheric pressure. In our study, we use instruments specifically designed for measuring either high-frequency turbulent static pressure p or the low-frequency (barometric) static pressure P (Table 1).

A long-standing challenge in atmospheric static pressure measurements has been avoiding the effects of dynamic pressure on static pressure (see Section S1 in the supplement for additional discussion). If the measurement goal is static pressure, then dynamic pressure generated by air motion (wind) can "contaminate" static pressure measurements. In wind tunnels or on solid objects, static pressure is typically measured by small pressure taps that are placed along surfaces perpendicular to, or streamlined, with the flow direction. To measure static pressure in the free atmosphere, probe designs are typically either flat plates with small pressure ports or cylinders with small ports along the circumference of the cylinder to take advantage of the symmetry of the flow around the cylinder (e.g., Benedict, 1984; Nishiyama and Bedard, 1991; Rossow, 1991). A primary concern with static pressure probes is how the angle of attack (and possible flow-separation) affects the measured static pressure, which is especially true near forests where large attack angles of the airflow are possible.

In the early 1990s NOAA developed the Nishiyama-Bedard quad-disk pressure probe (Nishiyama and Bedard, 1991) to meet these challenges. The resulting probe has been found to be fairly insensitive to errors due to dynamic pressure as well flow angle and wind direction (Lanzinger and Schubotz, 2012; Nishiyama and Bedard, 1991; Woo et al., 1989). The Nishiyama-Bedard quad-disk probe (or ports of similar design) have been used in a number of field experiments (e.g., Cuxart et al., 2002; Nieveen et al., 2001; Patton et al., 2011; Wilczak and Bedard, 2004) as well as the NASA InSight Mars landing (Banfield et al., 2019), and have been extensively tested in wind tunnels (e.g., Lanzinger and Schubotz, 2012; Nishiyama and Bedard, 1991; Oncley et al., 2008). Wyngaard et al. (1994) suggested that wind tunnel results from a quad-disk probe can be used to assess errors in atmospheric static pressure measurements relative to the turbulent kinetic energy budget. For our study, we assess the angle-of-attack sensitivity in a highly-turbulent (real-world) environment by performing a series of sensor manipulation/tilting experiments at the US-GLE scaffold. This effort tests the applicability of wind-tunnel results in field conditions (i.e., the sensitivity of $\overline{w'p'}$ to angle-of-attack errors). A more complete description and results from these experiments are in Appendix B.

3.3. Pressure measurements

Static pressure was measured using a Nishiyama-Bedard quad-disk that was co-located with the SATI/3Vx sonic anemometers on the US-GBT tower and US-GLE scaffold (Table 1, also Fig. S2 in the supplemental material). For both systems, the quad-disk port was attached via $\approx$ 2 m of tubing (Dekabon, 9.53 mm O.D., Synflex, Aurora, OH) to one differential input port of a differential pressure transducer (Furness Controls, Ltd., Bexhill-on-Sea, England, model FCO44), while the other differential port was connected to a known reference volume. The reference volume was also connected to the quad-disk port through flow resistors creating a resistance-capacitance (RC) time constant of 17.6 s (e.g., Hristov, 2008; Wilczak and Bedard, 2004) allowing it to high-pass filter the pressure signal. An example of the phase difference between the raw and processed pressure data is in Fig. S3 within the supplemental figures. The GLEES pressure-measurement system is a near-duplicate of the one described in Wilczak and Bedard (2004), and a schematic can be found in their paper. With this technique, (i) the resolution of the pressure measurement is very high (0.001 Pa) and (ii) the low-frequency portion of the pressure signal is lost. Hence, low frequency pressure at GLEES was obtained only from a slow-response barometer (Frank et al., 2014, Table 1).

As mentioned previously, data at the US-GBT tower (and initially at the US-GLE scaffold) were collected with the ATI datapacker (e.g., Zeller et al., 2001). In January of 2009 the data system at US-GLE transitioned from the ATI datapacker to a Campbell Scientific CR3000 data logger. The ATI datapacker had an analog input voltage range of $\pm$ 12 V while the range of the CR3000 was $\pm$ 5 V. Thus, a voltage divider was needed to collect the Furness transducer data with the CR3000. During data analysis for this paper, it was discovered (and confirmed by laboratory tests) that the voltage divider attenuated the Furness analog signal. This necessitated a gain-correction factor with a value of 1.8 be applied to the pressure data collected with the CR3000. Though the measurement range of the Furness FCO44 transducer is specified to be $\pm$ 20 Pa, we found that they operate beyond this range until clipping occurs. Details of the method used to determine the correction factor and other issues related to clipping of the pressure signal are in Sections S2 and S3 in the supplement.

Figure 1a provides an example of the above-canopy turbulent static pressure and above-canopy mean horizontal wind speed U measured at US-GLE during a day with both windy and low-wind conditions. As described above, the low-frequency portion of the pressure signal is removed leading to both negative and positive pressure fluctuations around zero. During the windy periods ($U > 6$ m s^{-1}), the peak-to-peak variations of the above-canopy turbulent pressure were on the order of $\pm$ 60 Pa. During low-wind periods, peak-to-peak p variations become as small as $\pm$ 1 Pa (for example, at around 20:00 MST in Fig. 1a).

3.4. NEE measurements at GLEES

In order to evaluate NEE at GLEES, the CO_2 storage, temperature, and water vapor terms in Eq. (1) are needed. At US-GLE, CO_2 storage was calculated from a vertical profile of CO_2 mixing ratio measurements (LI-COR, model LI-7000) at 8 equally spaced inlets throughout the canopy ranging from 22.65 m down to 0.1 m above the ground (with the lower inlet adjusted to the snowpack). There was no CO_2 storage measurement at the US-GBT tower, so we have neglected this term for our study (based on the US-GLE measurements, the CO_2 storage term is small). The fast-response CO_2 and water vapor measurements were from an open-path IRGA (either a NOAA IRGA or a LI-COR, model LI-7500, see Table 1 for details). At US-GLE, the IRGA was located 0.235 m east, 0.08 m south, and vertically aligned with the ATI sonic anemometer.

Post-processing applied median filter despiking, quality assurance and quality control, and calibration adjustment. The covariances were calculated using the planar-fit wind velocity components and time-lag adjusted scalars, with subsequent spectral correction following Massman (2000). As described in Frank and Massman (2020), between January 2009 and March 2011 the IRGA self-heating correction used fast-response temperature sensors placed within the IRGA measurement path. After March 2011, the IRGA surface temperature was used, and prior to 2009 a model of the IRGA path temperature was used. Further description of the GLEES measurements along with the ambient meteorological values associated with the pressure, temperature, and water vapor terms are in Frank and Massman (2020); Frank et al. (2014).

To supplement the NEE tower measurements we have included CO_2 fluxes from the US-GLE snowpack for years 2011–2016 in our analysis.

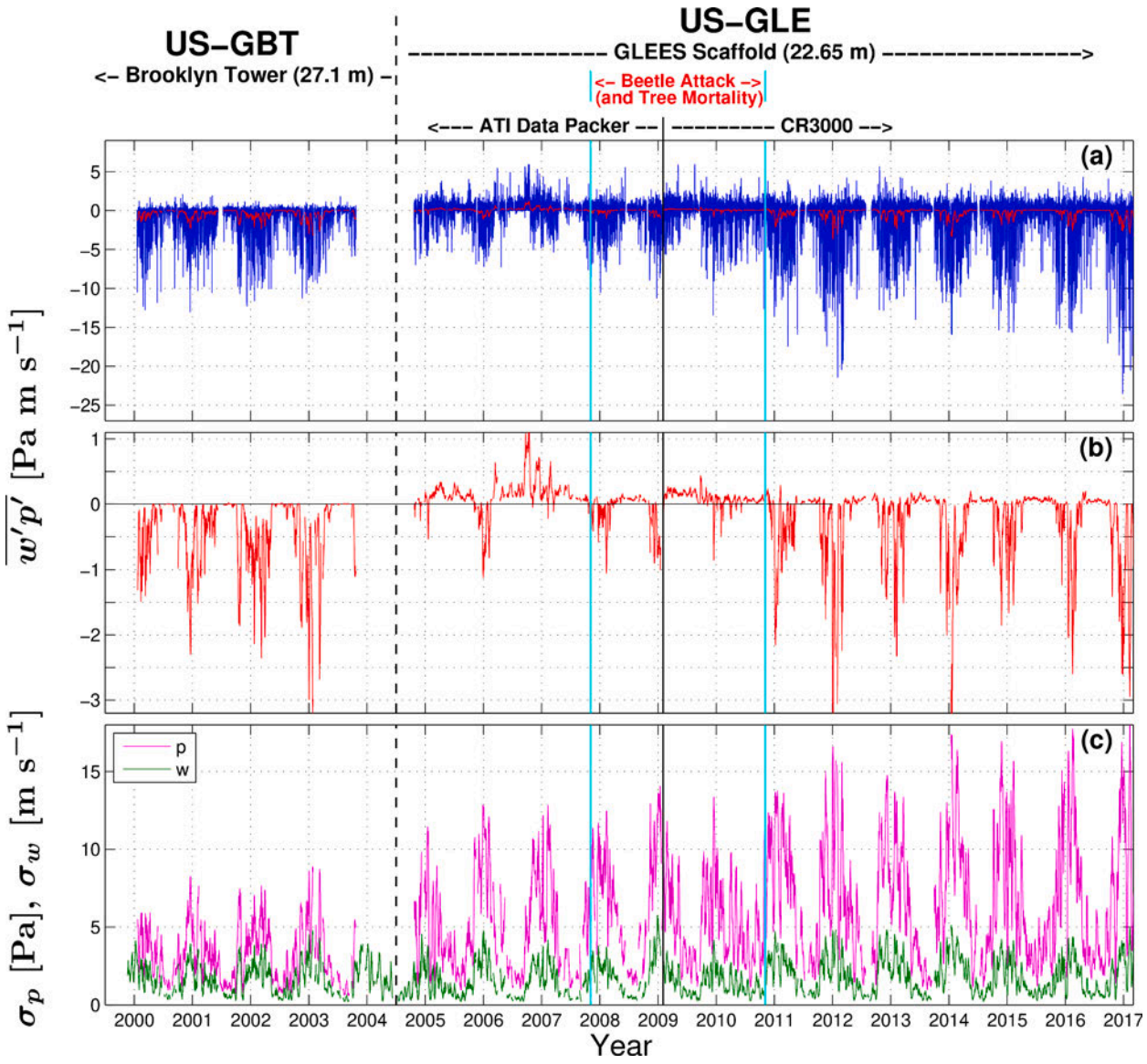

Fig. 2. Multi-year time series of **(a)** the 30-min vertical wind pressure covariance $\overline{w'p'}$ overlaid with $\overline{w'p'}$ smoothed by a 10-day sliding median window (red line), **(b)** only smoothed $\overline{w'p'}$, and **(c)** the smoothed standard deviation of turbulent static pressure σ_p and vertical wind σ_w. As indicated by the text above panel **(a)**, from late 1999 to mid-2004 measurements were made from the Brooklyn tower (US-GBT) while from late 2004 to 2017 they were made from the GLEES scaffold (US-GLE). The period between water years 2007 and 2010 is when the GLEES forest was attacked by spruce beetle and the forest structure was modified (indicated by the vertical cyan lines), and in January 2009 the data system at US-GLE was changed from the ATI datapacker to a Campbell Scientific CR3000 data logger (indicated by the vertical black line). (For interpretation of the references to color in this figure legend, the reader is referred to the web version of this article.)

These fluxes were calculated based on vertical CO_2 profiles within the snowpack with additional details described in Berryman et al. (2018). We use the snowpack flux data as an independent check of the winter-time above-canopy NEE measurements from the US-GLE scaffold.

3.5. Pressure data processing and calculation of $\overline{w'p'}$

Data processing of the pressure data is similar to that described by Wilczak and Bedard (2004). The raw 20-Hz turbulent pressure data were (i) median-despiked (Frank et al., 2014), (ii) low-frequency trends were removed by subtracting a locally estimated scatterplot smoothing (LOESS) time series based on a 10-min window for smoothing, and (iii) frequency-corrected to remove some of the effects of the physical high-pass filter. The latter was performed by gap filling via linear interpolation, Fourier transform, multiplying by the inverse transfer function of the equivalent RC high-pass filter, removing all frequencies below a cutoff of 0.00333 Hz (i.e., 5-minutes, chosen a priori because lower frequencies have too little signal-to-noise), inverse Fourier transform, and reinstating the median-despiked gaps. We use the term "processed" pressure for data based on steps (i)–(iii), whereas "raw" pressure data p_{raw} comes directly from the data logger where the only quality control was removing outliers and/or obviously bad samples.

The optimal time lag between turbulent pressure and vertical wind velocity for $\overline{w'p'}$ was determined by measuring the system lag time between p and w, and modeling the effective lag between sensors as a result of spatial separation (based on wind direction and speed). The latter was calculated from the half-hour average wind direction and velocity (Horst and Lenschow, 2009). By "system" lag we are referring to any aspect of the data-collection which caused delays in the measured signal, this includes items such as internal data-processing within the instrument, delays due to data logger sampling, delays due to signal transmission times, etc. The system lag (assumed constant) was added to the

separation lag to provide a total lag time that was used in the covariance calculation. It was determined at US-GLE by measuring the time between injecting a pulse of pressurized gas into the air stream of each sensor and measuring when it responded in the data stream; on average the p signal responded 0.048 s before w. For the ATI datapacker (used prior to January 2009) it was found that the p signal responded 0.076 s before w (this assessment was done in the laboratory rather than at the field site). Appendix A contains additional details about the system lag calculation and Fig. S4 in the supplemental material shows an example of the total lag used in the data-processing.

When we evaluate the effect of $\overline{w'p'}$ on NEE (see Section 4.9), we present results assuming a zero time lag in p as well as using the optimal lag (i.e., what is shown in Fig. S4). Unless noted otherwise, $\overline{w'p'}$ uses the optimal lag; the reason we include the zero lag case is to ascertain the importance of including the proper pressure time lag on our results.

The above description reflects the actual (measurable) time lag between two spatially-separated sensors—in our study we also use time lags as a tool for examining the sensitivity of various terms to lag effects. Such sensitivity tests help reveal differences in physical processes as well as exploring the parameter space of our results.

3.6. Analysis methods

The analysis will first confirm a few basic attributes of the pressure and wind measurements (namely the variance/standard deviation, spectra, and phase between w and p). Much of our analysis uses four different wind speed ranges which we define as: calm ($0 < U \leq 1.5$ m s^{-1}), low ($1.5 < U \leq 4$ m s^{-1}), medium (4 m s^{-1} $< U \leq 6$ m s^{-1}), and high ($U > 6$ m s^{-1}) winds. Because of the close relationship between wind and pressure, the effect of lags on $\overline{w'p'}$ (as well as $\overline{u'p'}$ and $\overline{v'p'}$) will be considered by shifting the pressure data one sample at a time and calculating the 30-min covariances. From the covariance, the correlation coefficient r_{xy} is calculated, where x and y are the variables of interest. For example, for $\overline{w'p'}$, the correlation coefficient is calculated by,

$$r_{wp} = \frac{\overline{w'p'}}{\sigma_w \sigma_p}, \quad (2)$$

where σ_w and σ_p are the standard deviations of w and p, respectively. The resulting curves of r_{wp} versus lag time reveal how sensitive the covariances are to lags, and, as we will show in Sections 4.6 and 4.8, the sign and magnitude of $\overline{w'p'}$ is particularly sensitive to time lags.

Following previous work (e.g., McBean and Elliott, 1975; Wilczak and Businger, 1984; Zhang et al., 2011), we examine how $\overline{w'p'}$ normalized by air density and cubed friction velocity u_* varies with atmospheric stability (based on the stability parameter, $\zeta = z/L$, where L is the Obukhov length). McBean and Elliott (1975) use the turbulent kinetic energy equation to show that the normalized pressure should only depend on ζ. We considered including the zero-plane displacement height d in the stability parameter definition (i.e., $\zeta = (z - d)/L$), but any effect of d on ζ was extremely small on our results, so we have used the simpler form for ζ.

In order to estimate the effect of the pressure term on annual NEE, yearly cumulative values for each term in the NEE equation are calculated for each water year (1 October through 30 September). Following conventions in the biogeosciences community, the NEE units for the diel cycle analysis are μmol m^{-2} s^{-1} while the cumulative annual NEE (over the water year) uses units of g C m^{-2} year^{-1}. Because cumulative annual sums requires continuous 30-min data, any missing data were replaced (or "gap-filled") with the corresponding value from the mean diel cycle calculated from a time period of ±10 days around missing samples. The exception to this is the pressure term, which was gap-filled based on a 2nd order polynomial fit to U for each water year. In our results we note that a difference exists between the annual value for gap-filled NEE compared to the sum of cumulative values of the gap-filled individual terms in Eq. (1). This issue and a discussion of the amount of gap-filling required for the pressure term is in Section 4.10.

4. Results and discussion

4.1. Time series of $\overline{w'p'}$ at GLEES

The 16-year time series of $\overline{w'p'}$ reveals changes to the sign and magnitude of $\overline{w'p'}$ over time (Fig. 2a, b). During this long period, there were two significant changes at GLEES which affected the pressure measurements. First, in 2004, the flux measurement location was moved from 27.1 m on the US-GBT tower to 22.65 m on the US-GLE scaffold (see Section 2 for details). Second, the forest surrounding the US-GLE scaffold was killed by beetles between years 2008 and 2010 reducing the forest LAI from a value of 4.7–4.9 m^2 m^{-2} prior to 2008 to around 2.6 m^2 m^{-2} by 2011 (Frank et al., 2019; Speckman et al., 2015). Because we have these two fairly distinct changes, we have broken our analysis of $\overline{w'p'}$ into three periods: (i) water years 2000–2004 measurements from the US-GBT tower, (ii) water years 2005–2009 measurements from the US-GLE scaffold (prior to beetle-induced changes in the forest structure), and (iii) water years 2011–2016 measurements from the US-GLE scaffold with a reduced canopy drag (or LAI). We do not include water year 2010 because it appears to be a time when the forest structure is in transition (i.e., the dead trees were losing needles, etc). As highlighted in Fig. 2a, $\overline{w'p'}$ on the US-GBT tower rarely went above zero which was not the case for the US-GLE scaffold. By smoothing $\overline{w'p'}$ (i.e., Fig. 2b) it is apparent that during the period of 2005 to 2009 the occurrence of large negative values of $\overline{w'p'}$ were reduced. Finally, from Fig. 2c, it can be seen that the standard deviation of turbulent pressure σ_p was smaller on the US-GBT tower compared to the US-GLE scaffold. In the subsequent sections we will explore (and attempt to explain) the reasons for the unique characteristics within each period.

4.2. Relationship between turbulent pressure and turbulent vertical wind with mean horizontal wind speed

Previous studies have shown that turbulent pressure fluctuations are proportional to the air density ρ times either the square of mean horizontal wind speed (e.g., Bedard et al., 1992; Mohr et al., 2016; Shaw et al., 1990; Sigmon et al., 1983; Tennekes and Lumley, 1972) or squared friction velocity u_* (e.g., Katul et al., 1996). In general, we found a fairly linear relationship between the turbulent pressure standard deviation σ_p and squared above-canopy horizontal wind speed U^2. As an example, a month of US-GBT data had a slope of 0.07 Pa s^2 m^{-2}, whereas that from US-GLE was around 0.22 Pa s^2 m^{-2} (Fig. 3a). Because air density at GLEES is very close to 1 kg m^{-3}, it had little effect on this relationship and we have not included it in Fig. 3a (this is also to be consistent in the comparison with other datasets which do not include density).

The difference in the slopes of σ_p versus U^2 between US-GBT and US-GLE shown in Fig. 3a is perplexing. A change in the character of σ_p when the measurement location was changed from US-GBT to US-GLE can be observed in Fig. 2c. Furthermore, the slope of σ_p versus U^2 over time is fairly constant at each location as seen in the full 16-year time series of the monthly σ_p slope (Fig. S5b, within the supplement).

As a contrast to σ_p, a similar comparison of the standard deviation of the vertical wind σ_w versus U is shown in Fig. 3b. There is also an increase in slope when the site was changed from US-GBT (slope of 0.22) to US-GLE (slope of 0.27). However, the percentage change in the slope for σ_w between US-GBT and US-GLE was not as large as that of σ_p, and the long term time series of the monthly σ_w slope shows fairly consistent values for each location (see Fig. S5a within the supplement). Between 2004 and 2005 wind measurements were made at both US-GBT and US-GLE, so we can directly compare U and σ_w,

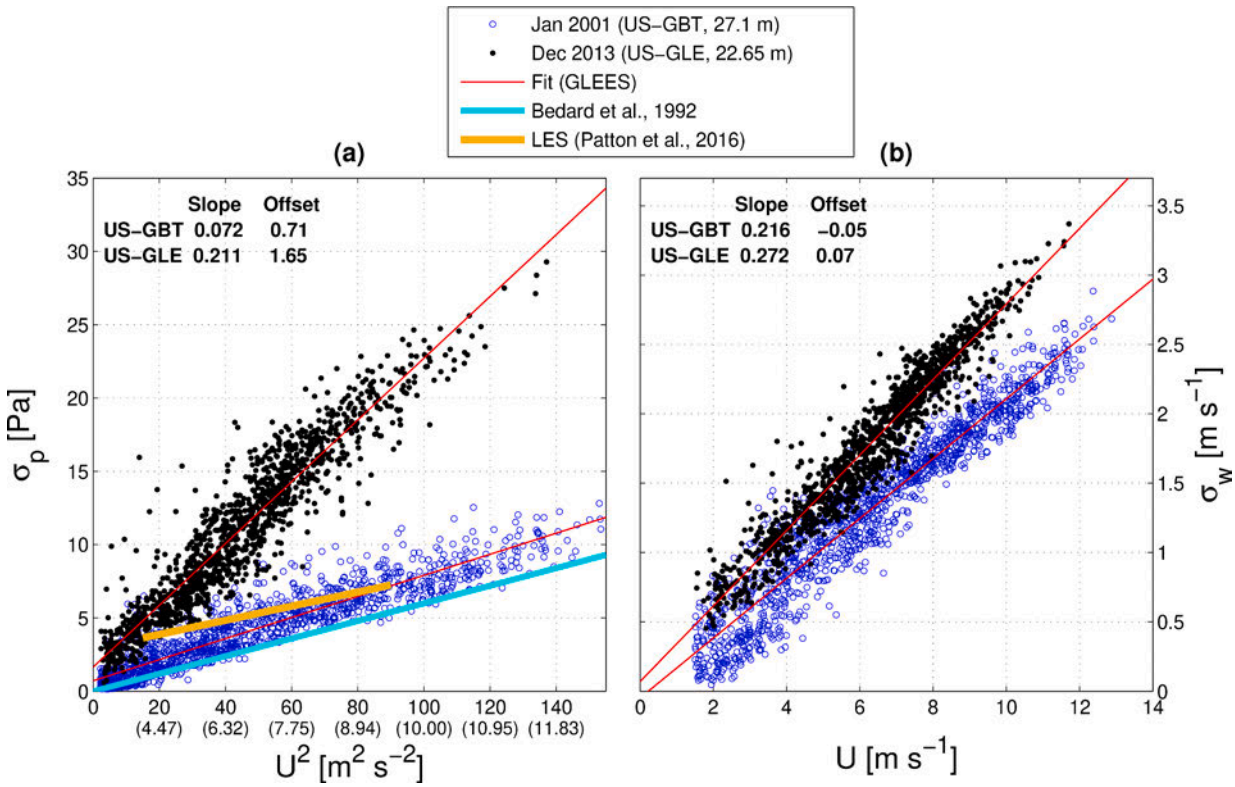

Fig. 3. Monthly relationships of **(a)** the 30-min standard deviation of static pressure σ_p versus the square of above-canopy mean horizontal wind speed U, and **(b)** the standard deviation of vertical velocity σ_w versus U for the US-GBT tower and US-GLE scaffold (see legend). The resulting slope and offset from a linear least-squares fit are shown in the upper-left corner of each panel. Periods with $U < 1.5$ m s^{-1} have been excluded for reasons described within the text (Section 4.7). In **(a)**, corresponding (un-squared) U is listed in parentheses below the x-tick marks and the relationships determined by Bedard et al. (1992) from a Colorado grassland site (slope $= 0.06$ Pa s^2 m^{-2}), and from a large-eddy simulation (LES) model over a forest (at $z = 2h$, slope $= 0.048$ Pa s^2 m^{-2}) by Patton et al. (2016) (their near-neutral case) are shown.

and find that σ_w at US-GBT was only 3% larger than σ_w at US-GLE, while the horizontal wind speed was 45% larger at US-GBT than at US-GLE (see Fig. S6 within the supplement). With similar σ_w values at each site, the larger US-GBT wind speed values explains why the slope of σ_w versus U is smaller at US-GBT (e.g., returning to Fig. 3b, it can be observed that, for a similar value of σ_w, the larger wind speed at US-GBT will lead to a smaller slope).

Unfortunately, there were not concurrent pressure measurements at US-GBT and US-GLE during the overlap period in 2004–2005. However, while US-GLE σ_p had maximum values near 25 Pa, US-GBT σ_p maximum values were on the order of 12 Pa (Fig. 3). Therefore, unlike σ_w, the increase in the σ_p slope at US-GLE is due to a combination of smaller U and larger σ_p. The field measurements of Bedard et al. (1992) and the LES of Patton et al. (2016) (as shown in Fig. 3a) are more consistent with σ_p from US-GBT than those from US-GLE, which suggests an elevated magnitude of US-GLE σ_p. The LES results are, of course, independent of any measurement issues or contamination by dynamic pressure. More discussion of the wind speed differences between US-GBT and US-GLE and possible explanations for the elevated values of σ_p at the US-GLE scaffold are in Section 4.11.

4.3. Spectral power of pressure and vertical wind

The above-canopy turbulent pressure power spectra fS_p in windy conditions at US-GLE shows a spectral peak at around 0.08 Hz (Fig. 4a). As wind speed decreases the spectral peak shifts toward lower frequencies and larger eddies. At frequencies larger than the peak (i.e., within the inertial subrange), the spectral slopes of fS_p changes from a value of -0.97 in high winds to -0.87 in calm winds. These inertial subrange slopes are about 30% steeper than those of Zhang et al. (2011) who found an average slope of about -0.5 with a range between -0.8 and -0.2, and Wilczak et al. (1992) who found a slope close to $-2/3$ (which is expected for velocity). For free shear flows, George et al. (1984) found a slope of $-4/3$ and pointed out that pressure should have a steeper spectral slope in the inertial subrange than vertical velocity. For a wall-bounded flow, Albertson et al. (1998) found an inertial fS_p slope of $-1/2$ in the surface layer. Possible reasons for these slope differences can be related to the surface type and height above the surface (see discussion in Zhang et al. (2011)) as well as interaction between the large and small scale pressure fluctuations (Albertson et al., 1998). We also note that there is a slight steepening of the fS_p slope to $-4/3$ for f larger than around 2 Hz (Fig. 4a).

In Fig. 4a, the effect of the high-pass filter and amplitude-compensation on the fS_p spectral shapes can be observed between f of 0.00333 Hz and ≈ 0.04 Hz, where the black lines are the frequency-corrected fS_p. For the calm-wind conditions ($U < 1.5$ m s^{-1}, highlighted in red), fS_p using raw p peaks at $f \approx 0.002$ Hz which is lower than the cut-off frequency. Furthermore, the shape of the raw pressure spectra does not attenuate with decreasing f as it does for the other wind speed ranges (and also does for calm vertical wind spectra fS_w, shown in Fig. 4b), which suggests that the peak in the raw fS_p spectra has shifted into the noise range of the pressure-measurement-system and that valid data may not be recoverable by the data processing (see Section 4.7 for further discussion).

Except for calm-wind conditions, the vertical wind spectra fS_w shown in Fig. 4b have characteristics similar to those of the pressure spectra. Unlike the pressure spectra, the spectral peak and shape of fS_w can be sensitive to the sign of the temperature gradient, especially in calm winds (e.g., Burns et al., 2006; Dupont and Patton, 2012; Kaimal et al., 1972). The w spectral slopes in the inertial subrange more closely follow

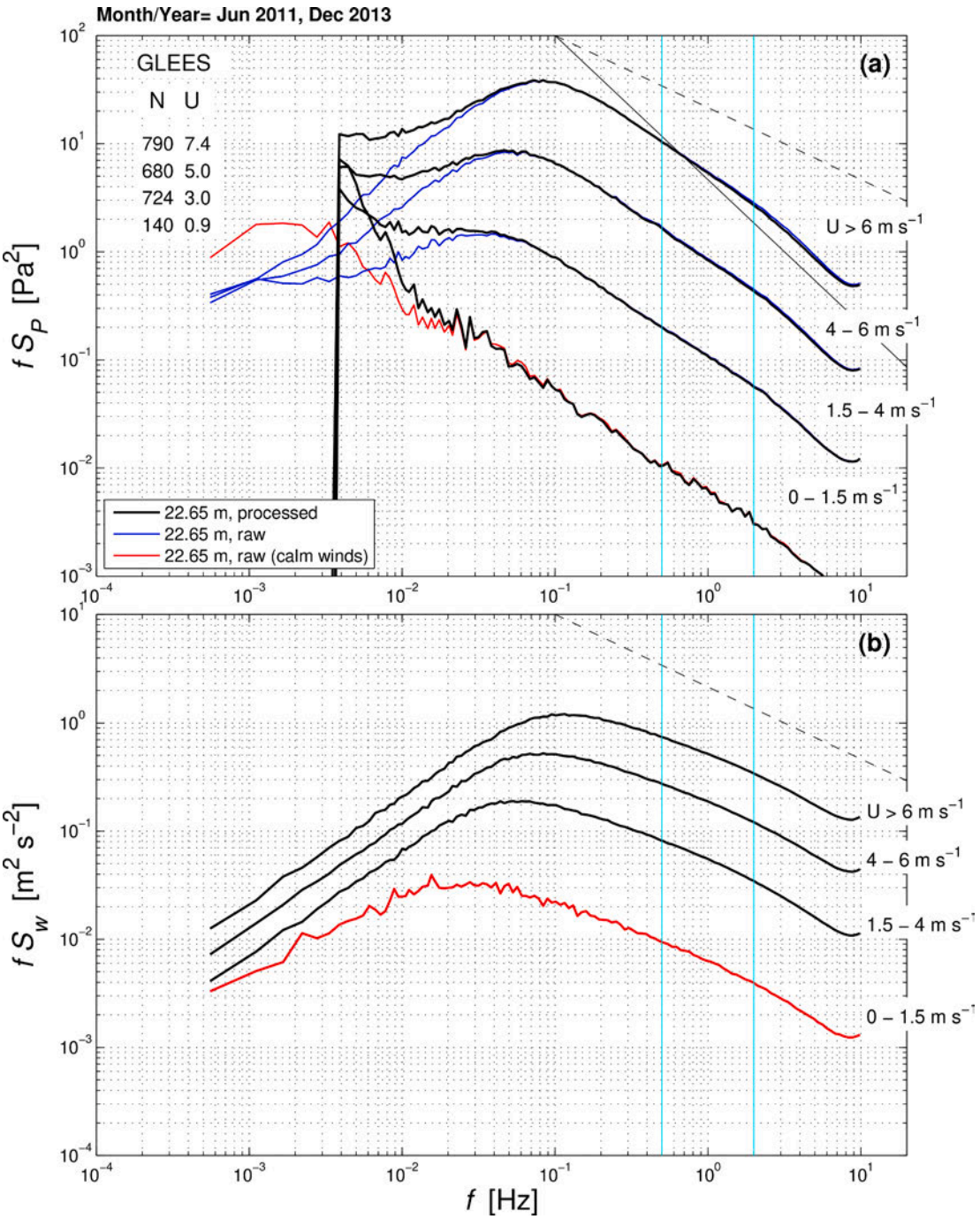

Fig. 4. Mean composite logarithmic spectra of above-canopy **(a)** turbulent static pressure S_p and **(b)** planar-fit vertical wind S_w versus frequency f. The 30-min periods are categorized by four different horizontal wind speed U ranges, as indicated to the right of each curve. In the upper-left corner of panel **(a)**, the number of 30-min time periods (N) and mean U (for each U range) are provided. In **(a)**, spectra from the raw and processed pressure data are shown as described in the legend. For clarity, the lowest wind speed case is shown as a red line in **(a)** and **(b)**. The dashed line in the upper-right corner shows a $f^{-2/3}$ slope while the solid line in **(a)** shows a $f^{-4/3}$ slope. The spectral slopes (estimated using 0.5 Hz$< f <$ 2 Hz, as indicated by the vertical cyan lines) for the highest to lowest wind speed ranges for fS_p are: -0.97, -0.95, -0.91, and -0.87; similarly, but for fS_w they are: -0.56, -0.59, -0.62, and -0.64. These are US-GLE data from June 2011 and December 2013. (For interpretation of the references to color in this figure legend, the reader is referred to the web version of this article.)

the $-2/3$ slope than those of pressure, with high wind w spectral slopes of -0.56 and calm wind slopes around -0.64. Note that for pressure, the spectral slope decreases as wind speed decreases, while for fS_w the slope increases as wind speed decreases. Also, for the higher wind speed conditions, the peak in fS_w appears to be at around 0.1 Hz, a slightly higher frequency than the 0.08 Hz of peak fS_p suggesting that the most energetic pressure fluctuations are at a slightly longer time scale than those of vertical wind.

For more insight into the differences in σ_p and σ_w between the US-GBT and US-GLE sites (as discussed in Section 4.2), we compared the pressure and vertical wind spectra between the two sites for three wind speed ranges. As shown in Figs. S7–S9 (in the supplement), it is apparent that US-GLE pressure spectra and vertical wind spectra both have higher energy than those from US-GBT, and the extra energy exists fairly evenly across the entire frequency range. This suggests that for similar mean winds, the wind shear is larger at US-GLE, leading to larger spectral

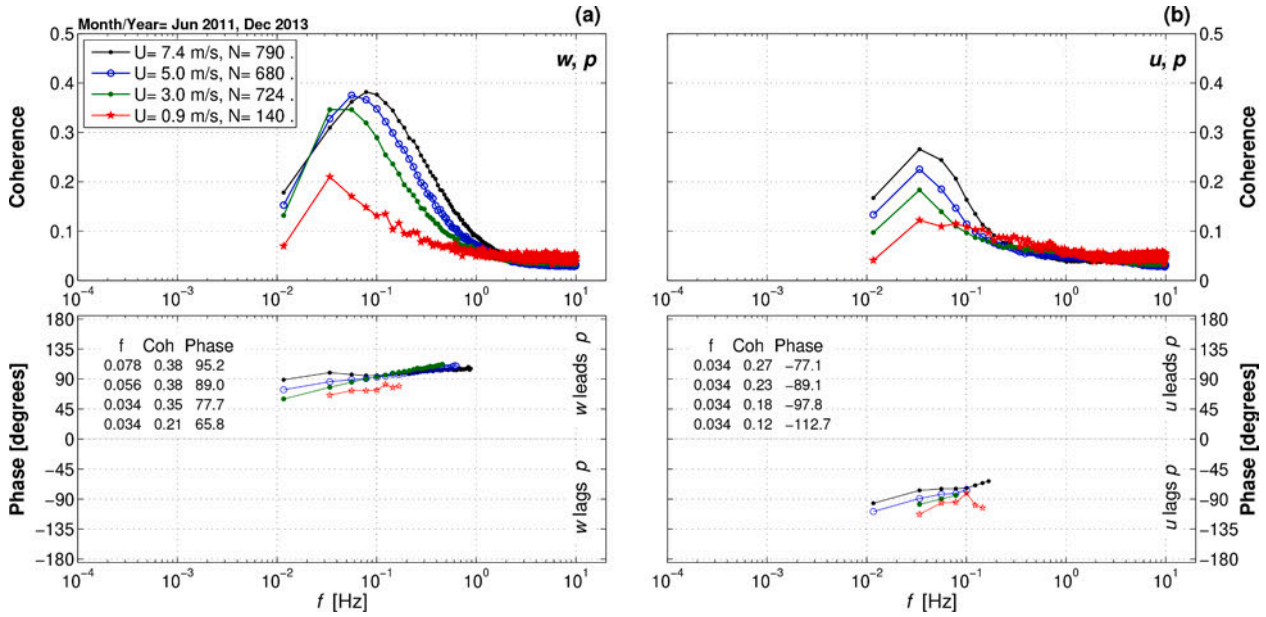

Fig. 5. Mean composite spectral coherence and phase at US-GLE scaffold of above-canopy **(a)** the planar-fit vertical wind w and static pressure p and **(b)** the streamwise wind velocity u and static pressure p versus frequency f. As described in the legend, the 30-min periods are categorized by different horizontal wind speed U ranges [0 – 1.5 m s^{-1}, 1.5 – 4 m s^{-1}, 4 – 6 m s^{-1}, and over 6 m s^{-1}], where the number of 30-min time periods (N) and mean U (for each U range) are provided. The phase is only shown for coherence > 0.1. A positive phase angle indicates that the wind component leads p as described in the phase panels. The values of f at the maximum coherence, the maximum coherence, and corresponding phase are shown in the lower panels. These are data from June 2011 and December 2013.

energy (turbulence) across all scales/frequencies.

To dig a little deeper, we normalized each spectra by it's own maximum value which reveals how different frequency bands (or time scales) behave relative to the peak value. For vertical wind, there is almost no difference between the normalized w spectra for US-GBT and US-GLE (e.g., Fig. S7b). However, for static pressure, the US-GBT spectral peak is shifted to a slightly lower frequency than that of US-GLE, and the relative energy in the low frequency range (0.004 Hz$< f <$ 0.04 Hz) at US-GBT is larger than that of US-GLE (e.g., Fig. S7a) which suggests that the pressure field has different characteristics at each site, but vertical wind is similar. If this was due to a phenomena related to the mean wind speed, such as tree sway which has a frequency that is typically in the range of 0.15 to 0.4 Hz (e.g., Bunce et al., 2019), one would expect this signal to diminish (or disappear) in lower wind conditions. However, we see the same low-frequency feature in similar plots for medium (Fig. S8) and low (Fig. S9) winds. Possible reasons for differences in the pressure fields at US-GBT and US-GLE are discussed in Section 4.11.

4.4. Spectral coherence and phase of pressure and wind

In high winds, the coherence between vertical wind and pressure reached a maximum of 0.38 at $f \approx 0.08$ Hz (Fig. 5a). For lower winds, the coherence drops and peaks at a lower frequency (consistent with the shift in the spectral peaks shown in Fig. 4). For high winds, the phase between w and p is at around $+$ 90 degrees indicating that they are nearly perfectly out of phase. We find that the vertical wind leads pressure, consistent with previous results over grasslands and tidal flats (e.g., Elliott, 1972; Kataoka et al., 1989); in contrast, the theoretical work by Lee (1997) looking at forest gravity waves and the observations by Zhang et al. (2011), both concluded that pressure leads w. The reason for this discrepancy is unknown, but Wilczak and Businger (1984) suggested that the phase between w and p in a convective boundary layer depends on measurement height above the surface and/or the relative proximity to the coherent structures.

The peak coherence between the streamwise wind u and pressure (Fig. 5b) is almost half that of the w,p coherence (Fig. 5a). The phase between u and p is generally around $-$ 90 degrees, with the streamwise wind lagging pressure (Fig. 5b). This is consistent with Zhuang and Amiro (1994) who showed that u lags p with a phase angle of around $-$ 86 degrees near the top of a forest and that the phase difference became smaller as one descends lower into the canopy. It is also qualitatively similar to McBean and Elliott (1978) who found that u lags p with a phase angle of around $-$ 40 degrees over a grassland. Fig. 5 infers that just-above the forest at GLEES, u and w have a phase angle of around 180 degrees. Lenschow and Sun (2007) found that the u,w phase is highly variable near the surface in a convective boundary layer over the ocean, with a typical values between 190 and 280 degrees.

The phase angles of $+$ 90 degrees for w and p and $-$ 90 degrees for u and p is consistent with an ejection (where w is positive and u decreases) occurring just-before a peak in static pressure, followed by a sweep (where w is negative, and u increases). The dynamics of these coherent structures just-above a forest and the close relationship they have with static pressure have been discussed in previous work (e.g., Finnigan et al., 2009; Shaw et al., 1990; Shaw and Zhang, 1992). This topic goes outside the scope of the current study; however, we have done some preliminary analysis on the interaction between static pressure and the coherent structures (i.e., Burns et al., 2017) which will be presented in a future paper.

4.5. Covariance sensitivity to time lags

To highlight the sensitivity that $\overline{w'p'}$ has to lags, we show the cospectra of pressure and the three wind components with different (constant) lags applied to the pressure data in high-wind conditions (Fig. 6a–c). We contrast this with similar plots for sonic temperature (Fig. 6d–f) and CO_2 density ρ_c (Fig. 6g–i). The range of lags was chosen to bracket any actual lags due to sensor separation. For pressure, it is clear that $(Co)_{wp}$ (and thus $\overline{w'p'}$) will be positive if lags of $-$ 0.5 s or $-$ 1 s are applied to the pressure data, whereas lags of 0 s, 0.5 s or 1 s result in negative $(Co)_{wp}$ (Fig. 6c). The range of frequencies affected by the lags is generally between 0.03–0.8 Hz. In contrast, the cospectra of w and sonic temperature $(Co)_{wT}$ (Fig. 6f) and w and CO_2 density (Fig. 6i) would only

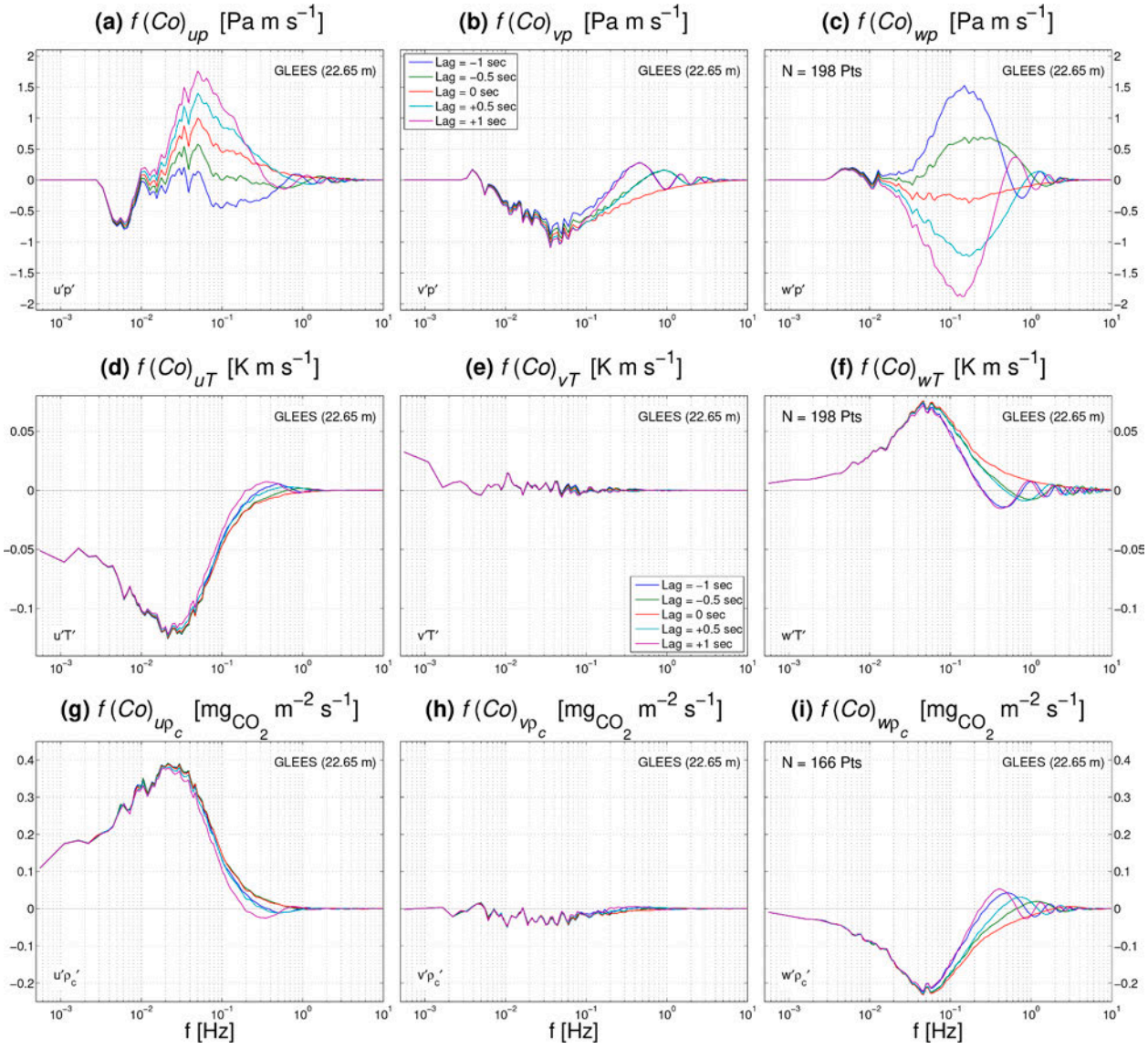

Fig. 6. Mean composite daytime values of frequency-multiplied cospectra of: **(a)** streamwise wind and pressure $(Co)_{up}$, **(b)** cross wind and pressure $(Co)_{vp}$, **(c)** vertical wind and pressure $(Co)_{wp}$, **(d)** $\overline{u'T'}$ cospectra $(Co)_{uT}$, **(e)** $\overline{v'T'}$ cospectra $(Co)_{vT}$, **(f)** $\overline{w'T'}$ cospectra $(Co)_{wT}$, **(g)** $\overline{u'\rho_c'}$ cospectra $(Co)_{u\rho_c}$, **(h)** $\overline{v'\rho_c'}$ cospectra $(Co)_{v\rho_c}$, and **(i)** $\overline{w'\rho_c'}$ cospectra $(Co)_{w\rho_c}$ versus frequency f (where T is sonic temperature and ρ_c is the CO_2 density with the units and variable name are listed above each panel). Each line has a different time lag applied to the scalar data, as specified in the legend of **(b)**. In the upper-left corner of **(c), (f)**, and **(i)**, the number of 30-min periods (N) used for each composite is shown. These are daytime periods from June 2011 selected for wind speed U greater than 5 m s^{-1} and less than 9 m s^{-1}.

be slightly affected (with no change of sign) if the same lags were applied to the temperature and ρ_c data. In a similar way, the cospectra of the streamwise wind and pressure $(Co)_{up}$ (Fig. 6a) is much more sensitive to lags than both $(Co)_{uT}$ (Fig. 6d) and $(Co)_{u\rho_c}$ (Fig. 6g).

The previous paragraph describes the *sensitivity* of the cospectra to a prescribed lag time, which is confounded by the actual time lags between the scalar and wind due to sensor separation (usually on the order of tenths of a second). High wind conditions were chosen for Fig. 6 so that the effect of sensor spatial separation is minimized. Because the sonic anemometer measures wind and temperature in the same air volume, we know the lag between T and w is zero, and we note that the oscillations in the cospectra for $f > 0.6$ Hz occur because the prescribed lag is incorrect. These oscillations in the cospectra are a telltale sign that the lag applied to a scalar in a flux calculation is incorrect. If we look again at $(Co)_{wp}$ in Fig. 6c such oscillations in the cospectra also exist which suggests that the 0.5-s and 1-s lags shown here are likely too large to be realistic.

Another take-away point from Fig. 6 is that the co-spectral peak for $(Co)_{wp}$ occurs at $f \approx 0.2$ Hz whereas that of $(Co)_{wT}$ and $(Co)_{w\rho_c}$ occur at a much lower frequency of around 0.07 Hz. This indicates that wind and pressure covary at scales related to the coherent structures, whereas the processes for temperature and CO_2 are more closely linked with surface-related source/sink phenomena driven by vertical scalar gradients. Entrainment also plays a role in the surface fluxes (e.g., Huang et al., 2008; Jonker et al., 1999; Vilà-Guerau de Arellano et al., 2004) which is not considered within the scope of the current study.

4.6. Correlation coefficient sensitivity to time lags

Another way to examine the sensitivity of the pressure-wind covariance to lags, is to plot the 30-min correlation coefficient as the pressure time series is shifted/lagged relative to the wind data. As an example, the 30-min correlation coefficient of vertical wind and pressure r_{wp} in windy conditions is shown in Fig. 7a. The $\overline{w'p'}$ curves are

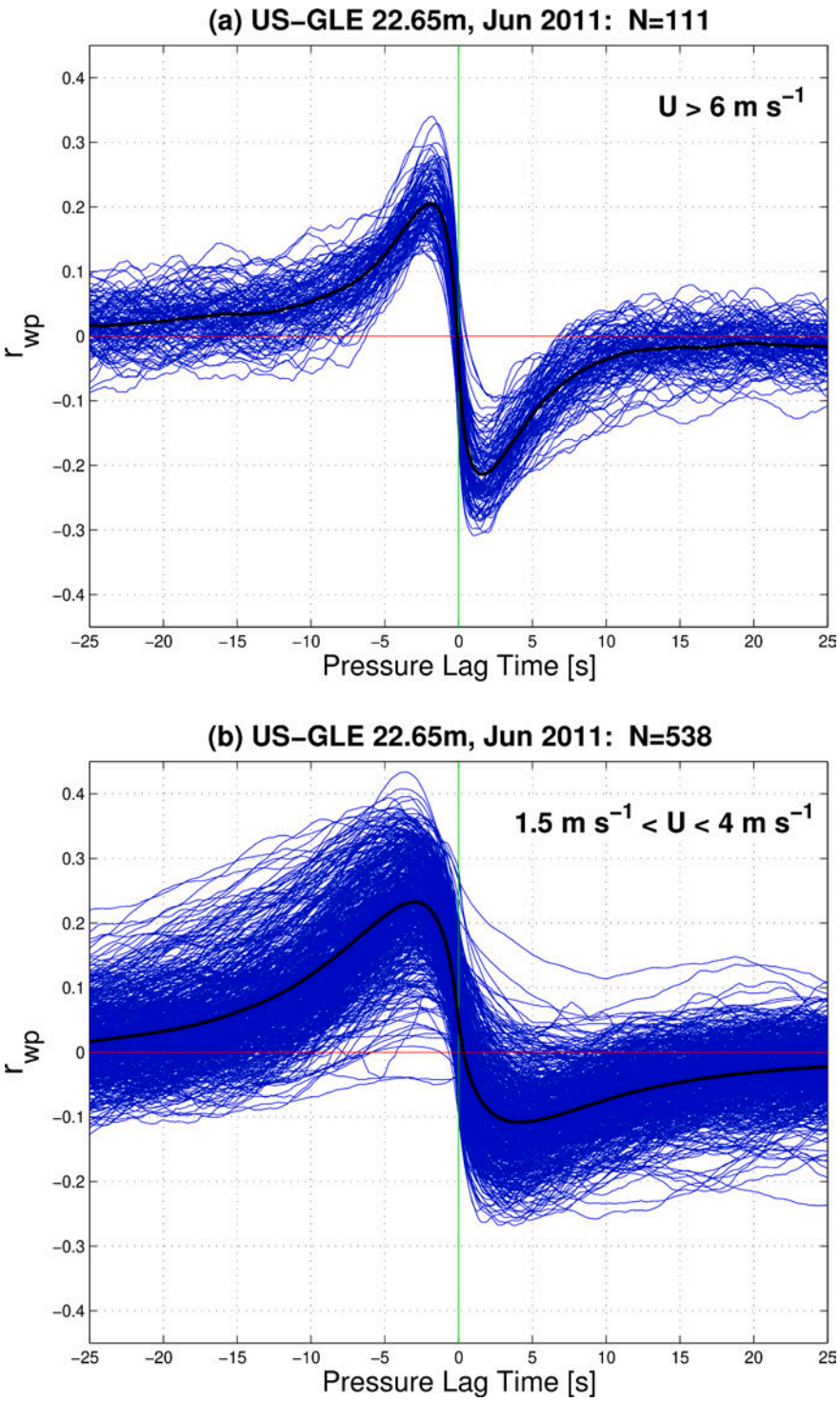

Fig. 7. The correlation coefficient r_{wp} of $\overline{w'p'}$ as the pressure lag is varied for **(a)** high and **(b)** low wind conditions. A positive lag time corresponds to pressure being shifted to a later time. Each blue line represents the results from an individual 30-min time period and the black line is the composite mean value. These data are from June 2011 and the number of 30-min periods (N) used is listed in each title. (For interpretation of the references to color in this figure legend, the reader is referred to the web version of this article.)

extremely steep around a lag of zero. For high wind conditions, the composite mean curve of r_{wp} crosses zero at a lag time of $-$ 0.1 s (in Fig. 7a, this is just to the left of the vertical line marking a pressure time lag $= 0$) which contrasts with the low-wind conditions where the zero crossing is at a lag time of 0.8 s (to the right of the vertical zero line in Fig. 7b). By looking at the individual 30-min periods (shown as blue lines), it is clear that the variability for the lower wind conditions is much larger than that of the high wind conditions (and there are both positive and negative zero crossings). The sensitivity of $\overline{w'p'}$ to lags was pointed out by Shaw et al. (1990), and is caused by the close interaction between wind and pressure in the coherent structures near the top of a forest. This means that any uncertainty in the estimated lag can significantly change both the magnitude and sign of $\overline{w'p'}$.

Our method for determining the lags due to the spatial separation of the quad-disk and sonic anemometer is described in Section 3.5. Because we assume that the air sample is advected by the mean wind past each sensor, the lag time is a strong function of mean horizontal wind speed U and wind direction (Fig. S4 in the supplement). For high winds ($U > 6$ m s^{-1}) the absolute value of the lag is on the order of 0.024 s, whereas in low winds ($U \approx 3$ m s^{-1}) the average absolute lag is 0.112 s. Even though high wind speeds lead to larger sensitivity of $\overline{w'p'}$ to a time lag in

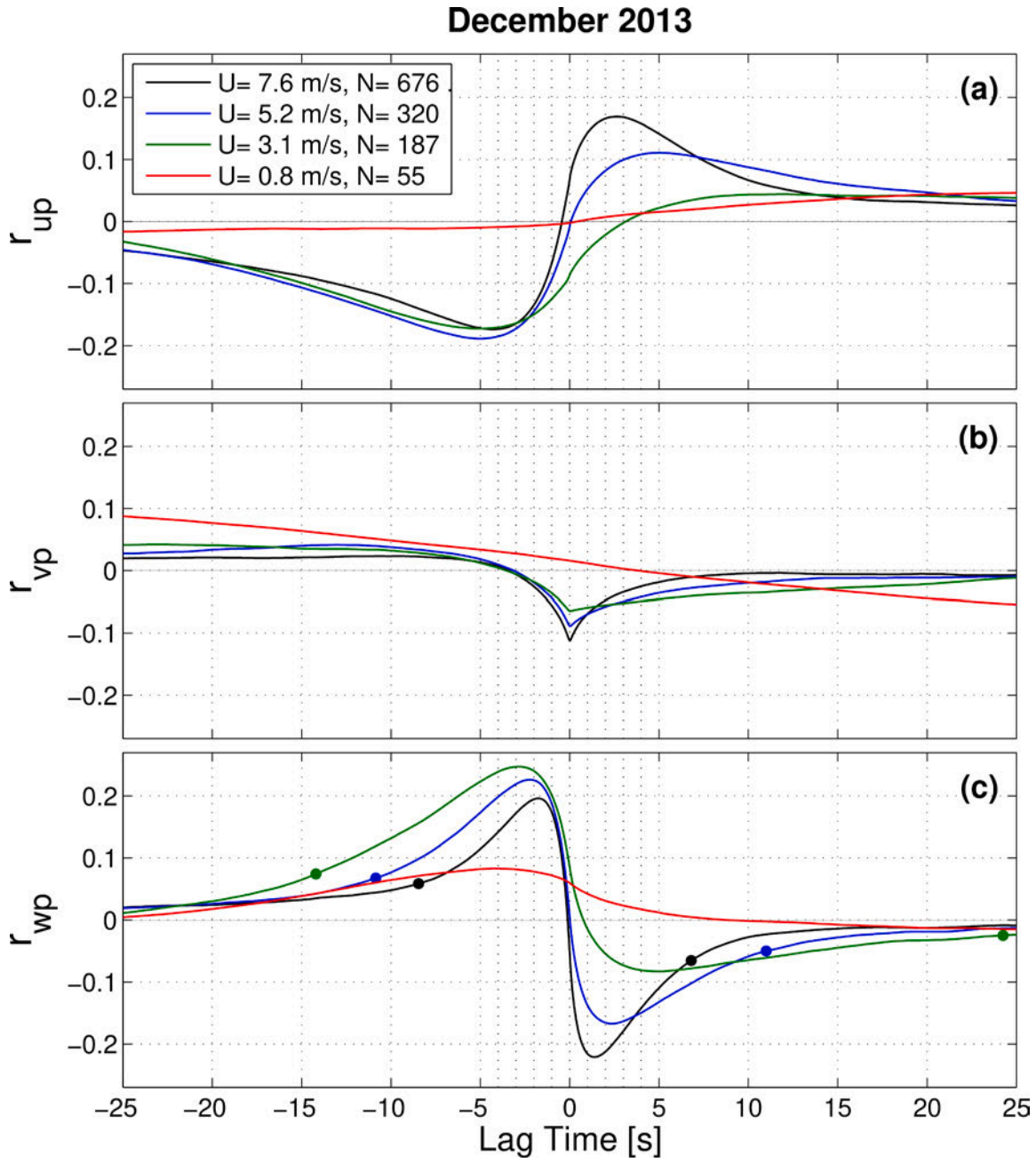

Fig. 8. The mean composite of the correlation coefficient between fluctuations of turbulent pressure p and the planar-fit wind components: **(a)** streamwise r_{up}, **(b)** crosswind r_{vp}, and **(c)** vertical r_{wp} as a time lag is applied to the pressure data. A positive time lag corresponds to pressure being shifted to a later time. These results are from December 2013 for four different wind speed U ranges [0 – 1.5 m s^{-1}, 1.5 – 4 m s^{-1}, 4 – 6 m s^{-1}, and over 6 m s^{-1}]. The legend in panel **(a)** lists the number of 30-min periods (N) and mean U for each composite. In **(c)**, the approximate time scale of the coherent structures is estimated based on the time between the 30% of peak values in r_{wp} and shown by the closed circles on the r_{wp} curves; the resulting time-scales are 15 s, 22 s, and 35 s for the high, medium, and low wind speed ranges (results were not well-defined for calm winds).

p (Fig. 7a), the estimated lags are smaller because the air sample will be more closely sampled (in time) by the wind and pressure instrument.

In Fig. 8 we examine how the correlation coefficient between each of the three wind components (u, v, and w) and pressure are affected by time lags in pressure for four ranges of wind speed. For clarity, only the mean composite values are shown. As wind speed decreases, the location that r_{up} and r_{wp} crosses the x-axis shifts toward the right (i.e., larger values of pressure time lag). For example, the r_{wp} curves in the high and medium wind ranges are similar and cross the x-axis at a slightly negative pressure lag time of around −0.1 seconds (Fig. 8c); however, in low and calm winds, the zero crossing is a positive lag time. The value of the pressure lag at the x-axis crossing by the correlation coefficient, determines the sign of $\overline{u'p'}$ and $\overline{w'p'}$. The crosswind-pressure covariance $\overline{v'p'}$ has a weaker correlation and does not appear to be strongly affected by pressure lags (Fig. 8b).

As the pressure time lag is varied in Fig. 8, it can be observed that $\overline{u'p'}$ and $\overline{w'p'}$ mirror each other. This is most evident in the high wind conditions. For example, as the pressure time lag increases from zero, $\overline{u'p'}$ becomes more positive, peaks, and then tapers to a small positive value, whereas $\overline{w'p'}$ becomes more negative, peaks, and tapers to a small negative value. This trend is consistent with the phase relationships

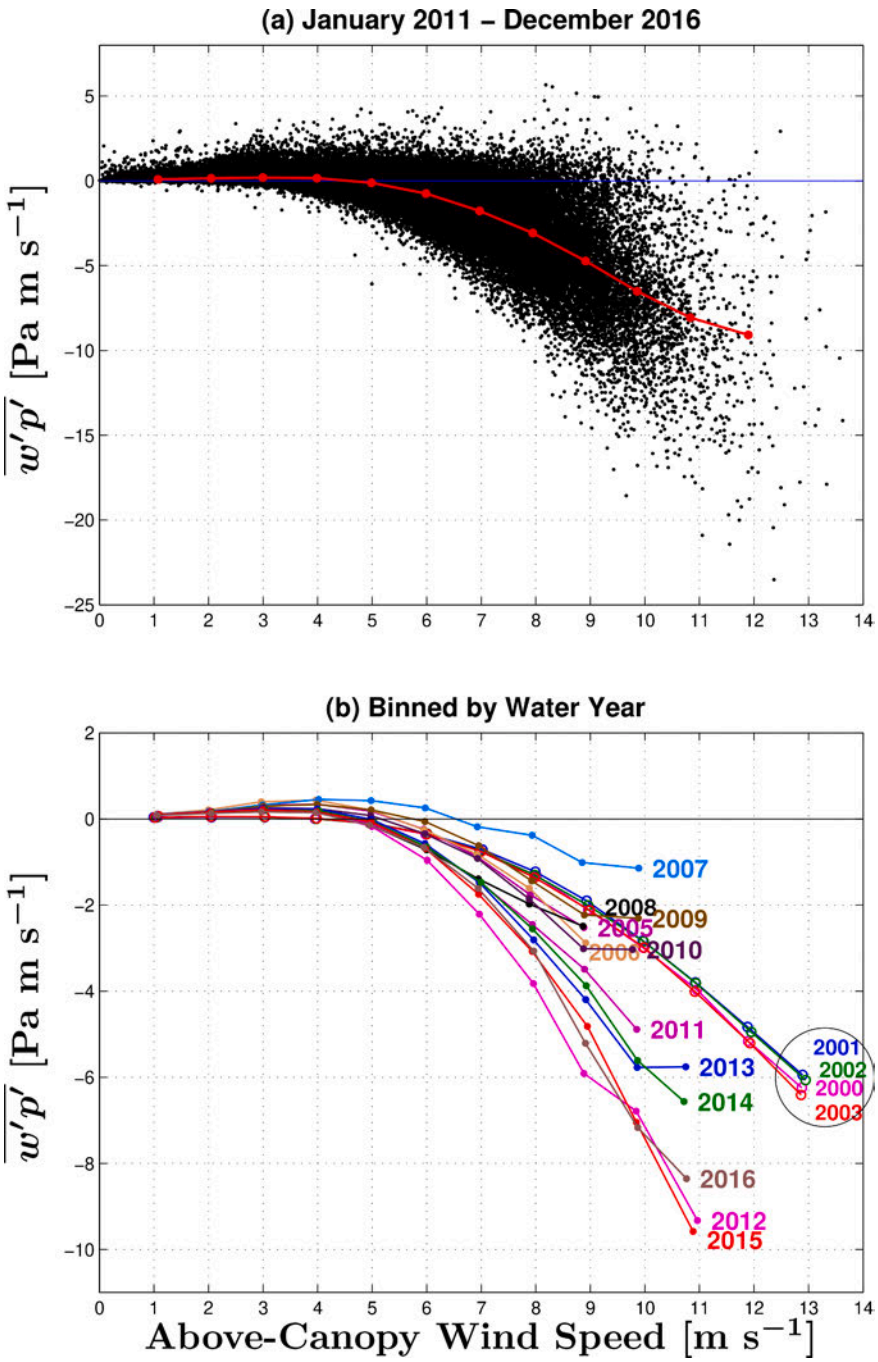

Fig. 9. **(a)** The vertical wind and pressure covariance $\overline{w'p'}$ versus above-canopy wind speed U for data collected between years 2011 to 2016. Each point represents a single 30-min $\overline{w'p'}$ value and the red line is the bin-average of $\overline{w'p'}$ versus wind speed. In **(b)**, the binned values of $\overline{w'p'}$ versus U for each water year (only bins containing more than 40 points are shown). The label for each year is to the immediate right of the highest wind speed value for each curve, and the color of the text matches the corresponding curve. Curves from US-GLE (water years 2005–2016) are shown as filled circles while the US-GBT curves (water years 2000–2003) are shown as open circles (and further identified by the large black circle). (For interpretation of the references to color in this figure legend, the reader is referred to the web version of this article.)

shown in Fig. 5 (i.e., that u, p and w, p are 180 degrees out of phase with each other) and consistent with the signature of coherent structures (as discussed at the end of Section 4.4). Characteristics of the coherent structures and their relation to wind speed are revealed in Fig. 8c by the increase in the value of r_{wp} for pressure lags < 0 (i.e., the ejection region) and the decrease in r_{wp} for pressure lags > 0 (i.e., the sweep region). This means that as wind speed decreases, the sweep of a coherent structure weakens while the ejection gets stronger. The filled-circles in Fig. 8c, use 30% of the peak correlation value to estimate the scale of the structure for different wind speed ranges and suggest a time scale of around 15 s in high winds and 35 s in low winds. The dependence of the time-scale magnitude on U is related to the size and horizontal speed of the coherent structures.

A final question highlighted by Fig. 8: what is happening with r_{wp} for the calm-wind conditions? It appears that something has altered the typical pattern associated with coherent structures that exist in the high, medium, and low wind cases as shown in Fig. 8c. It is likely that insufficient shear no longer supports the formation of canopy-scale structures (and other phenomena, such as gravity wave or buoyant plumes emanating from the canopy elements begin to dominate).

4.7. Pressure measurements in calm winds

As mentioned in Section 4.3, there was concern that the pressure signal in calm-wind conditions was not being properly measured. We compared correlation coefficients between the raw and processed turbulent pressure data (Fig S10 in the supplement), and the US-GLE turbulent pressure spectra with spectra from the US-GLE R. M. Young barometer as well as the pressure measured just-above the US-NR1 subalpine forest in Colorado (Fig S11). The low frequency portion

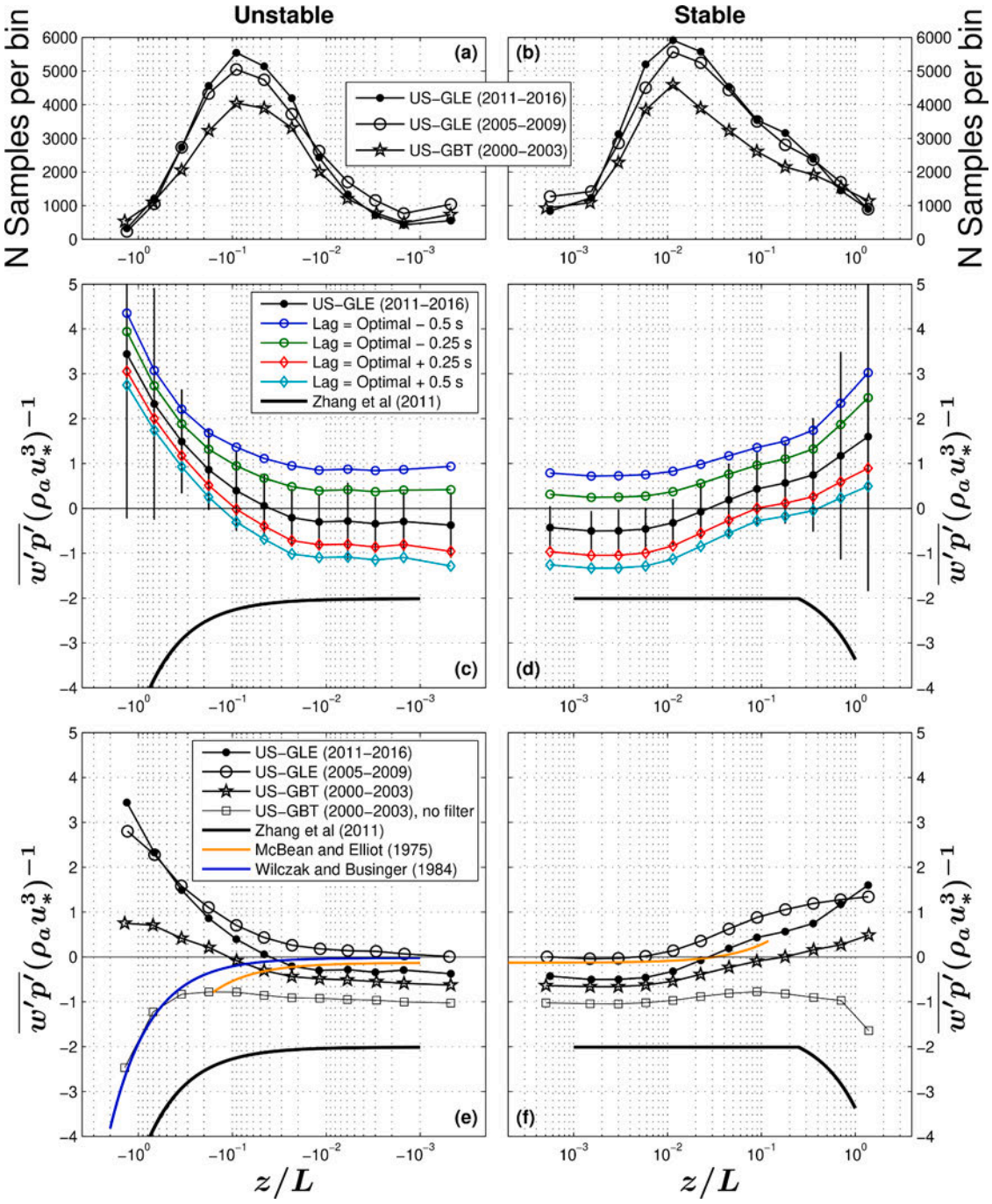

Fig. 10. The vertical wind and pressure covariance $\overline{w'p'}$ normalized by the air density ρ_a and friction velocity u_* cubed versus the stability parameter $\zeta = z/L$ for **(a, c, e)** unstable and **(b, d, f)** stable conditions. Panels **(a)** and **(b)** show the number of 30-min values that are within each bin for 22.65 m at US-GLE from years 2011–2016 and 2005–2009 and 27.1 m at US-GBT for years 2000–2003 (see legend). In the middle panels (**(c), (d)**), normalized $\overline{w'p'}$ from US-GLE for years 2011–2016 are shown for the optimal p lag time as well as with four alternate lag times applied to the pressure (see legend), along with the relationship determined by Zhang et al. (2011) (showing their "Whole Dataset" relationship). The black vertical bars show plus-minus one standard deviation of normalized $\overline{w'p'}$ for the optimally-lagged pressure data within each stability bin. The lowest two panels (**(e), (f)**) show the mean relationships for the two different US-GLE periods, and the US-GBT tower (both with and without the high-pass filter applied to the pressure data). Also shown are the relationships from Zhang et al. (2011), McBean and Elliott (1975), and Wilczak and Businger (1984).

(i.e., $f < 0.01$ Hz) of the pressure spectral slope should follow a value of $-4/3$ (Wilczak et al., 1992). From these comparisons, we make the following observations: (i) for calm winds, the correlation coefficient between p and p_{raw} was generally below 0.4, while in low wind conditions it was closer to 0.8 (Fig S10), (ii) in high winds, the pressure spectra between GLEES and US-NR1 agree well with each other and near $f \approx 0.01$ Hz the spectral shapes for P and p are similar (Fig S11a), (iii) in calm winds, the barometric P spectra and US-NR1 pressure spectra have low-frequency spectral slopes which are fairly close to $-4/3$ (Fig S11b), however the low-frequency spectral slope of the processed Furness pressure fS_p is much steeper than $-4/3$ indicating that p from the Furness transducer are likely in error. For these reasons, we feel the processed pressure during calm-wind conditions is incorrect and, when possible, we will leave these data out of our analysis. However, as shown in

Fig. 8c, calm-wind $\overline{w'p'}$ is generally small and $U < 1.5$ m s^{-1} only accounts for around 10% of the yearly 30-min periods (Table 3). Therefore, in our annual cumulative calculations, we have left the calm-wind $\overline{w'p'}$ values as-measured.

4.8. Effect of wind speed and stability on $\overline{w'p'}$

A scatter plot of 30-min $\overline{w'p'}$ measurements versus mean above-canopy wind speed U shows the variability of $\overline{w'p'}$ (Fig. 9a). Below around 5 m s^{-1} the majority of the $\overline{w'p'}$ values were above zero and the bin-averaged mean of $\overline{w'p'}$ (shown by the red line) was around 0.1 Pa m s^{-1}. As wind speed increased, the sign of $\overline{w'p'}$ became negative and reached values as large as around -20 Pa m s^{-1} for the strongest winds. However, for strong winds, there was a large amount of scatter around the bin-averaged mean values; for example, for a wind speed of 10 m s^{-1} $\overline{w'p'}$ had a mean value and standard deviation of -6.5 ± 3.6 Pa m s^{-1}.

In order to appreciate the changes in $\overline{w'p'}$ over the 16 years of pressure measurements at GLEES, the individual bin-averaged curves for each water year are shown in Fig. 9b. The four years of measurements at the US-GBT tower (highlighted by the large black circle) were very consistent from year-to-year. It is also apparent from Fig. 9b that the wind speeds measured at 27.1 m on the US-GBT tower were higher than those from the US-GLE scaffold. The curves for the US-GLE scaffold during the period 2005–2009 cluster along a similar curve as those from US-GBT, but the US-GLE wind speeds were much lower than those at US-GBT leading to smaller values of $\overline{w'p'}$. Starting around 2010, a change starts taking place. First, the mean wind speed starts increasing (presumably due to decreased wind drag by the beetle-damaged forest, as described in Section 4.1). This change is quantified in Table 3, where the percentage of 30-min periods with $U > 8.0$ m s^{-1} increased from around 2–3% for years 2005–2010 to 8–9% for years 2011–2016. Second, the slope of the $\overline{w'p'}$ curves with increasing U was steeper for years 2011–2016, leading to larger magnitude (i.e., more negative) values of $\overline{w'p'}$. These two observations highlight the primary $\overline{w'p'}$ differences between the 2005–2009 and 2011–2016 US-GLE periods; reasons for these differences are discussed in Section 4.12.

We compare the GLEES $\overline{w'p'}$ measurements to past research by plotting scaled $\overline{w'p'}$ versus the stability parameter $\zeta = z/L$ in Fig. 10. In near-neutral conditions, we found that the magnitude of $\overline{w'p'}(\rho_a u_*^3)^{-1}$ from US-GLE (2011–2016) was around -0.5 whereas that from Zhang et al. (2011) was closer to -2. The variations around the bin-averaged curve are provided by the black vertical lines in Fig. 10c, d, and by the scatter plot Fig. S12 in the supplement. Since we have previously shown that lag times in pressure can have a large impact on $\overline{w'p'}$ (i.e., Section 4.6), a range of lags between ± 0.5 s were added/subtracted to the optimal lag and then these curves were compared to the Zhang et al. curves (Fig. 10c, d). Though the scaled $\overline{w'p'}$ with the lags covers a range between -1.5 to $+1$, they did not become negative enough to reach the -2 scaled $\overline{w'p'}$ value from Zhang et al. (2011). Within the near-neutral stability range, the relationship between ζ and scaled $\overline{w'p'}$ from past projects (McBean and Elliott, 1975; Wilczak and Businger, 1984) agree fairly well with the GLEES results (Fig. 10e, f).

Zhang et al. (2011) showed that $\overline{w'p'}$ was virtually always negative (see their Fig. 5). A striking difference between the Zhang et al. (2011) and GLEES results is the trend of the scaled $\overline{w'p'}$ curves in low winds or large $|\zeta|$ (Fig. 10e, f). The sign of $\overline{w'p'}$ at GLEES was positive (and became more positive as conditions became more strongly stable or more strongly unstable), whereas for Zhang et al. (2011) it was negative and became more negative as conditions became more strongly stable or more strongly unstable. The curve from Wilczak and Businger (1984) has a similar shape as Zhang et al. (2011) in strongly unstable conditions; however, for the Wilczak study, pressure was inferred from temperature and velocity rather than measured directly.

In Fig. 10e, f we have included the GLEES relationship separated into the US-GBT and two US-GLE periods. Importantly, we have also included a US-GBT curve using the raw pressure for $\overline{w'p'}$ (i.e., without the high-pass filter, see Section 3.5). By comparing the two US-GBT lines in Fig. 10e, f, we observe the following: (i) in near-neutral conditions, using unprocessed pressure changes the value of scaled $\overline{w'p'}$ from around -0.6 to -1, and (ii) using raw pressure in strongly stable or strongly unstable conditions (i.e., for low winds) causes $\overline{w'p'}$ to be negative (and become more negative as the stability becomes more extreme) in a way that is very similar to the Zhang et al. curve. [The reason $\overline{w'p'}$ becomes negative using p_{raw} is shown in Fig. S13c, where $r_{wp_{raw}}$ is observed to cross zero at a pressure lag time of around –0.1 s, while r_{wp} crosses zero at a lag time of around 1 s. (i.e., the phase compensation in the pressure data processing shifts the location of the zero crossing of r_{wp} such that, on average $\overline{w'p'}$ is positive.)] The pressure measurements by Zhang et al. (2011) include a reference volume which they suggest acted as a high-pass filter, but they did not provide a description of the phase compensation which is a necessary part of such data processing (e.g., Wilczak and Bedard, 2004). Based on item (i) above, a lack of phase-compensation could explain why the Zhang et al. (2011) near-neutral scaled $\overline{w'p'}$ data are more negative than those from GLEES and other investigators. The above statements are speculative and another possible explanation is related to the distance above the surface—in Fig. 10e, f the near-neutral US-GBT scaled $\overline{w'p'}$ is more negative than the corresponding values from US-GLE (2011–2016) and US-GLE (2005–2009) which are both closer to the forest surface. Further discussion of the effect of measurement height on $\overline{w'p'}$ is in Section 4.11.

4.9. Effect of the pressure term on NEE at the hourly scale

For this section, the pressure term is calculated from $\overline{w'p'}$ and converted to the same units as NEE [μmol m^{-2} s^{-1}] following Eq. (1). For our open-path IRGA, NEE was primarily determined by the difference between the two largest terms in the NEE equation; the covariance $\overline{w'\rho_c'}$ and temperature term which were of opposite signs during the day and night (Fig. 11 and Table 2). On average, the spectral correction had a small ($\approx$ 2%) effect on $\overline{w'\rho_c'}$ covariance. The storage term was only important in the growing season during the morning and evening transition periods (which is why it is zero or near-zero in Table 2). The water vapor term was most significant during the growing season when forest transpiration occurs, however, even then, it was still only $\approx$ 4% of the covariance term (Table 2). We note that accounting for the IRGA heating was most important at mid-day when it increased the temperature term by around 2 μmol m^{-2} s^{-1} in summer (Fig. 11a) and 3 μmol m^{-2} s^{-1} in winter (Fig. 11b).

In winter, the forest is dormant and the primary source of CO_2 is respiration from microbes in the soil underneath the snowpack (Berryman et al., 2018; Bowling and Massman, 2011; Monson et al., 2006). In these conditions, the covariance and temperature term were nearly in balance (Fig. 11b) and NEE was small and positive (≈ 0.5 μmol m^{-2} s^{-1}). Winter is when the smaller terms can play a larger (relative) role in affecting calculated NEE, and the IRGA self-heating (or Burba correction) is most important. During the analysis for this paper we discovered that the mean mid-day wintertime NEE values between 2014 to 2016 were negative (Fig. A5). Therefore, we used the day and night NEE to determine an ad-hoc correction of 8% applied to the temperature term during this period (justification and details about the ad-hoc correction are in Appendix C). During daytime in the growing season, the main change from winter was that the negative covariance term becomes larger in magnitude than the temperature term, resulting in negative NEE values (Fig. 11a). Negative NEE indicates that photosynthetic

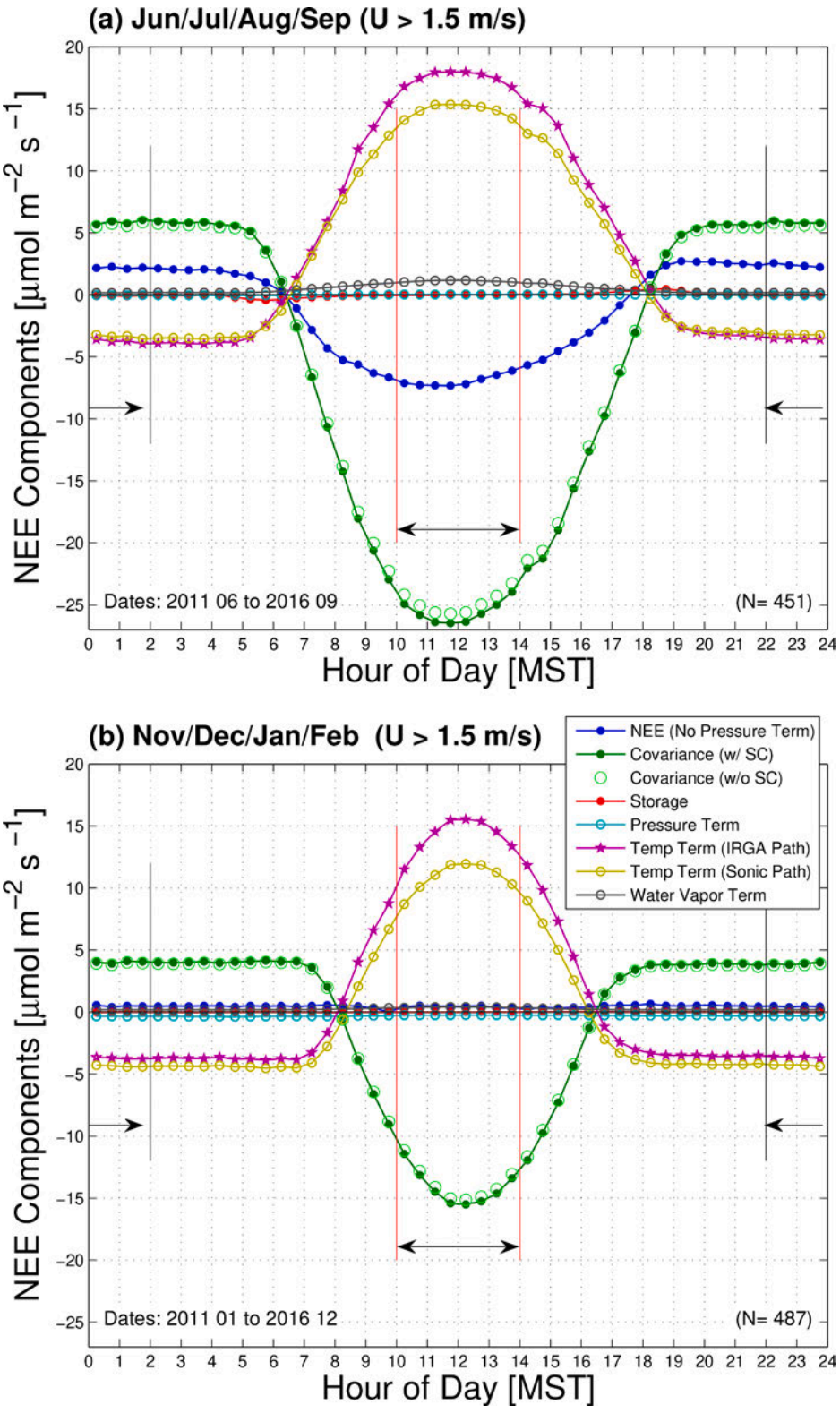

Fig. 11. The composite diel cycle of the terms in the NEE equation from the US-GLEE scaffold for years 2011–2016 during **(a)** the growing season (Jun/Jul/Aug/Sep) and **(b)** the dormant season (Nov/Dec/Jan/Feb). NEE is shown without the pressure term added to it; one temperature term is from within the LI-7500 sampling path and the other is within the path of the co-located sonic anemometer. The $\overline{w'\rho_c'}$ covariance is shown both with (filled circles) and without (open circles) the spectral correction (SC). For the scale of this plot, the storage and pressure terms are generally near the zero line (see discussion in the text). The vertical lines indicate the time periods used for calculating daytime and nighttime statistics shown in Table 2. The range of dates used and average number of samples (N) for each bin are shown in the lower left and right corners of each panel, respectively. Only 30-min periods when all measurements were available and the wind speed U was larger than 1.5 m s^{-1} were used for the composite.

Table 2
Daytime (10:00–14:00 MST) and nighttime (22:00–02:00 MST) mean statistics of the various terms in the equation for NEE (see Eq. (1) in the text) for the winter (dormant) and summer (growing) season. The diel statistics are from three periods: the US-GLE scaffold between January 2011 and December 2016 (US-GLE II), US-GLE between January 2005 and December 2009 (US-GLE I), and the US-GBT tower between November 2001 and September 2003. Statistics are only from periods when the mean horizontal wind speed was greater than 1.5 m s^{-1}. Values in bold are the terms used in Eq. (1) and shown in Fig. 11.

		Mean Values from the Diel Cycle [μmol m^{-2} s^{-1}]				
		Winter (Nov/Dec/Jan/Feb)		Summer (Jun/Jul/Aug/Sep)		
Variable	Notes	Daytime	Nighttime	Daytime	Nighttime	Location/Period
NEE[a]	No Pressure Term	**0.44**	**0.47**	**– 6.94**	**2.29**	US-GLE II
		1.15	0.41	– 9.80	2.40	US-GLE I
		0.49	– 1.51	– 7.81	1.18	US-GBT
CO_2 Storage		0	0	0	– 0.09	US-GLE II
		0	0	0	– 0.13	US-GLE I
		N.A.	N.A.	N.A.	N.A.	US-GBT
$\overline{w'\rho_c'}$	with Spectral Correction	**– 14.16**	**3.94**	**– 25.57**	**5.83**	US-GLE II
		– 10.07	2.98	– 24.69	5.42	US-GLE I
		– 9.68	1.77	– 21.59	4.25	US-GBT
$\overline{w'\rho_c'}$	no Spectral Correction	– 13.81	3.85	– 24.84	5.64	US-GLE II
		– 10.10	3.00	– 24.40	5.35	US-GLE I
		– 9.39	1.72	– 20.93	4.08	US-GBT
Temperature Term[a]	in IRGA Path	**14.21**	**– 3.66**	**17.52**	**– 3.61**	US-GLE II
		10.69	– 2.84	13.59	– 3.10	US-GLE I
		9.78	– 3.44	12.64	– 3.20	US-GBT
Temperature Term	in Sonic Path	10.89	– 4.30	14.91	– 3.25	US-GLE II
		8.85	– 3.52	12.82	– 3.08	US-GLE I
		8.04	– 2.97	11.78	– 2.29	US-GBT
Water Vapor Term		**0.39**	**0.18**	**1.11**	**0.16**	US-GLE II
		0.53	0.28	1.31	0.21	US-GLE I
		0.39	0.15	1.13	0.13	US-GBT
Pressure Term	with Optimal Lag	**– 0.25**	**– 0.32**	**0.03**	**– 0.03**	US-GLE II
		– 0.05	– 0.07	0.07	0.02	US-GLE I
		– 0.24	– 0.25	– 0.03	– 0.03	US-GBT
Pressure Term	with Zero Lag	– 0.19	– 0.25	0.04	– 0.02	US-GLE II
		0.01	– 0.02	0.08	0.03	US-GLE I
		– 0.22	– 0.23	– 0.02	– 0.03	US-GBT

[a] For US-GLE II, the ad-hoc correction to the temperature term described in appendix C has been applied.

uptake of CO_2 by the forest ecosystem is taking place.

At the scale of the mean diel cycle, the pressure term was relatively small compared to the other terms (e.g., in Table 2 the mean values for the pressure term were on the order of ± 0.02 μmol m^{-2} s^{-1} during summer and -0.25 μmol m^{-2} s^{-1} in winter, an order of magnitude smaller than the two dominant terms). Though small on average, the pressure term is very dependent on the magnitude of the mean horizontal wind speed. Therefore, the smaller terms from the NEE equation versus the mean above-canopy horizontal wind speed are plotted in Fig. 12 for US-GLE 2011–2016. When the mean wind speed reached around 8 m s^{-1}, the magnitude of the pressure term increased to $\approx$ 0.5 μmol m^{-2} s^{-1}. As highlighted by the rectangular boxes in Fig. 12, in winter around 10–15% of the 30-min periods had $U > 8$ m s^{-1} whereas in summer it was less than 1% of 30-min periods (for US-GLE, 2011–2016). This explains why the pressure term is especially important in winter at the GLEES site—winds are stronger and the respiration by the forest ecosystem is similar in magnitude to the pressure term. From Fig. 12, it is also clear that in windy conditions the pressure term was larger or of similar magnitude to the water vapor term, especially at night and in the winter.

Plots similar to Fig. 11 and Fig. 12, but for the US-GBT tower are shown within the supplemental material for the diel cycle (Fig. S14) and pressure term versus U (Fig. S15). For US-GBT, the magnitude of the pressure term was about 50% that of US-GLE (which is expected given the discussion in Section 4.8 and shown in Fig. 9b). However, the occurrence of high-wind conditions was more frequent at US-GBT (i.e., around 30% of 30-min periods in winter had $U > 8$ m s^{-1}, Fig. S15b, d) so the overall effect on the annual cumulative sums is similar to that of US-GLE 2011–2016 (see Section 4.10). At US-GBT, NEE was negative at night during the wintertime (Table 2, Fig. S14b and Fig. S15d). We attempted to apply the ad-hoc correction to the US-GBT NEE data, but it did not produce reasonable results (see Appendix C for details).

An important impact of including the pressure term is that wintertime NEE (and at night during the growing season) was largest during periods of high wind speeds (Fig. 12b, c, d). If the pressure term was not included in the NEE calculation, then NEE was nearly flat (or even slightly decreasing) at the higher wind speed values. Higher wind speed causing CO_2 to be flushed from the soil or snow surface is consistent with CO_2 isotope work that shows higher winds increase the ventilation of CO_2 from subalpine forest snowpacks (Bowling and Massman, 2011), a phenomena known as pressure pumping (e.g., Laemmel et al., 2019; Massman et al., 1997; Takle et al., 2004). In order to properly capture CO_2 pressure pumping from soil or snow with eddy covariance, including the pressure term in the NEE calculation is an important consideration. This becomes particularly important when the NEE

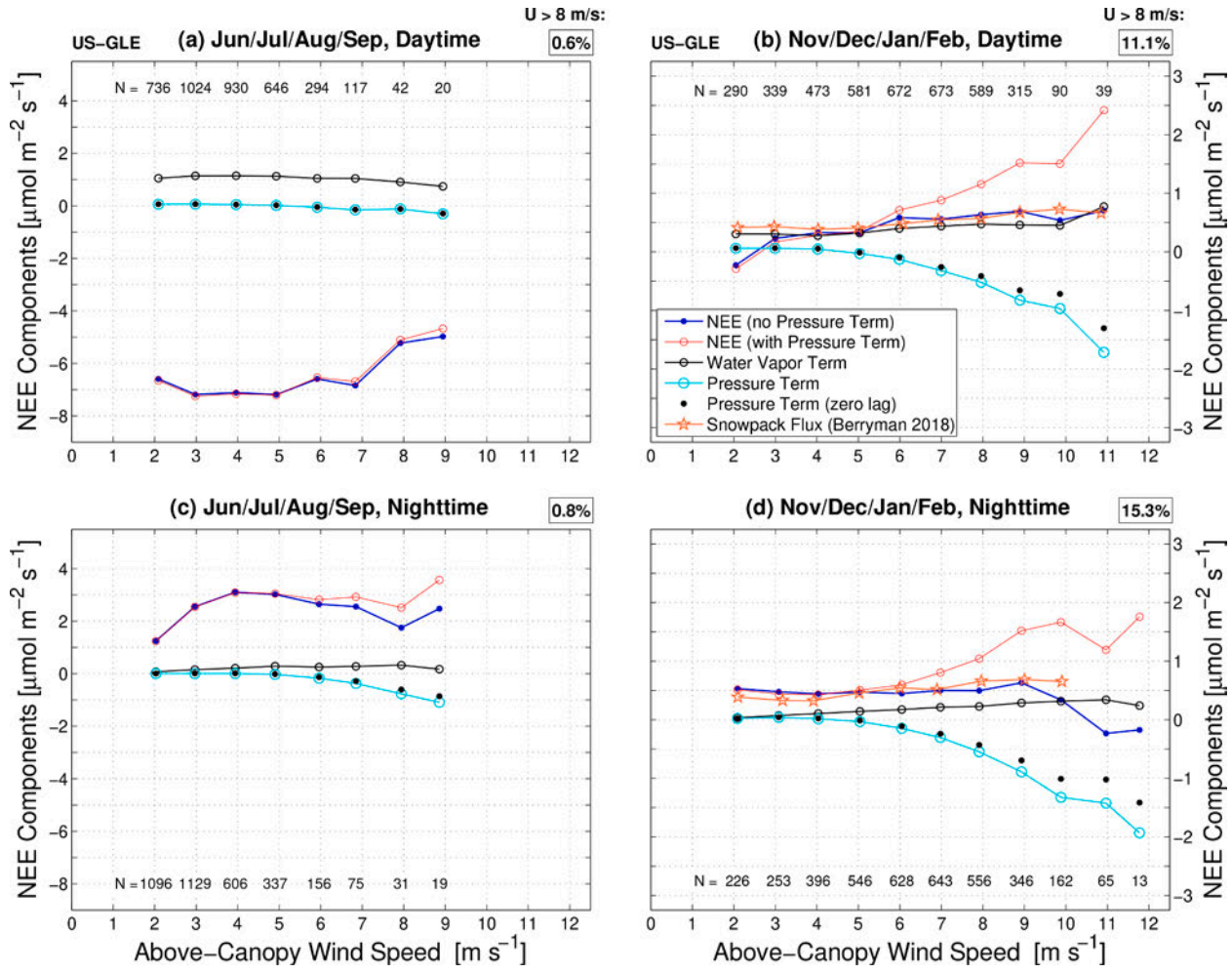

Fig. 12. The smaller terms in the NEE equation binned by the above-canopy mean horizontal wind speed U for **(a),(c)** the growing season (Jun/Jul/Aug/Sep), daytime and nighttime, and **(b),(d)** the dormant season (Nov/Dec/Jan/Feb), daytime and nighttime. Note that the y-axis limits are not the same for the summer and winter periods. As described in the legend, the variables plotted are NEE (with and without the pressure term), the water vapor term, and the pressure term (with optimal lag and assuming zero lag), and, for the winter periods only, CO_2 flux coming from the snowpack as determined by Berryman et al. (2018). CO_2 storage is very close to zero, so it is not plotted. The number of 30-min samples N within each U bin are shown either above or below each bin, and the percentage of 30-min samples with $U > 8$ m s^{-1} is shown in a box above each panel. These data are from the US-GLE scaffold for the period 1 January 2011 to 31 December 2016.

measurements are used to try and balance measurements of the CO_2 emitted from the soil under the snowpack (e.g., Berryman et al., 2018; Monson et al., 2006).

As an independent check of the NEE measurements, we use the CO_2 fluxes from the US-GLE snowpack (e.g., Berryman et al., 2018) as a function of wind speed in our analysis. As shown in Fig. 12b, d, there is a slight dependence of wind speed on the mean snowpack fluxes (increasing the snowpack flux from a value of around 0.3 μmol m^{-2} s^{-1} in low winds to 0.68 μmol m^{-2} s^{-1} in high winds), but this is much smaller than NEE with the pressure term included which reaches levels of around 2 μmol m^{-2} s^{-1} in high winds. In fact, the snowpack CO_2 fluxes agree much better to NEE without the pressure term. The reason for this mismatch is unknown, but a look at the physical process of wintertime fluxes (as related to wind speed) provides a bit of insight. As described by Berryman et al. (2018), the snowpack builds up CO_2 during periods of calm/low winds which is subsequently flushed out during the initial period of wind speed increase; however, for an extended period of high winds there is no CO_2 surplus within the upper snowpack so there is no corresponding increase in CO_2 flux. In contrast, the pressure term is omnipresent when the wind speed is high (i.e., independent of the amount of CO_2 within the snowpack).

Berryman et al. (2018) used a Bayesian model to estimate the 95% uncertainty level in the snowpack fluxes has a range on the order of $\pm$ 1 μmol m^{-2} s^{-1}. This suggests that wintertime NEE including the pressure term in high winds (Fig. 12b, d) is at the upper bounds of the snowpack fluxes uncertainty limit. Finally, we offer a few speculative reasons for the discrepancy between the snowpack fluxes and above-canopy NEE: (1) a bias in the Berryman et al. (2018) snowpack fluxes could exist due to a limited number of sampling sites, (2) the Berryman sampling locations did not include tree boles (which could act as "chimneys" that efficiently transport CO_2 between the lower snowpack and atmosphere), and (3) despite our best efforts, our calculated pressure term is over-estimated.

4.10. *Effect of the pressure term on NEE at the annual scale*

The yearly cumulative values for each term in the NEE equation are shown in Table 3 for water years 2000–2016. To do the annual sums, the gap-filling required for the pressure term ranged between 4–20%, excluding year 2000 when it was initially deployed (Table 3). If we consider each of our three time periods, the annual mean $\pm$ the interannual standard deviation of the pressure term were: $-$ 53.4 $\pm$ 7.7 g C m^{-2}

Table 3
The cumulative annual sums for each water year (1 October through 30 September) of the various terms in the equation for NEE (see Eq. (1) in the text). Notes for each variable are also described in Table 2. The interannual mean ± the standard deviation of NEE and the pressure term for three specific periods are shown in bold. Statistics related to ratio of the annual pressure term to annual NEE, gap-filling of the pressure term, and above-canopy horizontal wind are provided in the 5 lowest rows of the table.

	Annual Water Year Cumulative Sum [g C m^{-2} $year^{-1}$]																
Variable	2000[a]	2001[a]	2002	2003	2004	2005	2006	2007	2008	2009	2010	2011	2012	2013	2014	2015	2016
NEE (no pressure term)[b]	N.A.	N.A.	− 578.1	− 476.4	N.A.	− 427.4	− 301.2	− 131.1	18.3	− 7.8	219.1	183.2	− 82.6	− 75.8	− 104.2	− 150.1	− 149.4
NEE (no pressure term)[c]	N.A.	N.A.	− 659.8	− 534.2	N.A.	− 472.7	− 329.9	− 175.8	− 18.6	− 2.2	195.1	162.0	− 124.8	− 106.4	66.3	− 156.6	− 149.6
CO_2 Storage	N.A.	N.A.	N.A.	N.A.	N.A.	− 0.1	0.1	0.2	0.4	− 0.2	− 0.1	− 0.1	− 0.1	− 0.1	− 0.1	− 0.2	− 0.2
$\overline{w'\rho_c'}$ (with Spectral Corr.)	N.A.	N.A.	− 1600.9	− 1373.7	N.A.	− 1682.0	− 1520.0	− 1337.1	− 1259.9	− 1186.4	− 1074.5	− 1195.8	− 1678.3	− 1599.4	− 1245.3	− 1510.4	− 1455.3
Temperature Term (IRGA Path)[d]	479.6	694.6	840.1	750.9	N.A.	1061.3	1013.4	1007.0	1088.0	1042.3	1137.8	1233.5	1435.9	1372.2	1186.8	1240.2	1193.3
Temperature Term (Sonic Path)	546.9	608.9	707.9	617.9	N.A.	819.0	673.7	686.5	769.5	684.8	775.5	812.4	951.7	872.4	712.3	895.7	818.2
Water Vapor Term	85.5	128.9	101.0	88.6	N.A.	148.2	176.6	154.0	152.9	142.1	131.9	124.4	117.7	120.9	125.0	113.9	112.6
Pressure Term (zero lag)	− 38.9	− 38.9	− 51.5	− 53.5	N.A.	5.4	4.9	23.8	− 7.3	0.7	− 2.7	− 29.7	− 53.4	− 27.2	− 37.9	− 27.3	− 35.8
Pressure Term (optimal lag)	− 58.3	− 41.9	− 55.7	− 57.8	N.A.	− 5.6	− 9.1	12.7	− 22.0	− 10.9	− 12.7	− 44.1	− 67.6	− 41.5	− 54.1	− 40.2	− 51.0
Mean / Std Dev of:																	
NEE (no pressure term)	**– 527.25±71.9** (US-GBT, 2002–2003)					**– 169.8±191.5** (US-GLE, 2005–2009)							**– 63.1±124.8** (US-GLE, 2011–2016)				
Pressure Term (optimal lag)	**– 53.4±7.7** (US-GBT, 2000–2004)					**– 6.9±12.6** (US-GLE, 2005–2009)							**– 49.8 ±10.3** (US-GLE, 2011–2016)				
Percentages of:																	
Pressure Term / NEE	N.A.	N.A.	9.6%	12.1%	N.A.	1.3%	3.0%	− 9.7%	− 119.9%	139.6%	− 5.8%	− 24.1%	81.9%	54.8%	51.9%	26.8%	34.1%
Pressure Term Gap-filled	42.1%	12.2%	3.7%	20.3%	N.A.	16.2%	17.5%	15.7%	13.4%	12.8%	5.3%	15.4%	18.0%	8.1%	11.9%	7.7%	6.5%
Wind Statistics:																	
annual $\overline{U}$ (m s^{-1})	5.8	5.3	5.7	5.6	N.A.	3.5	3.8	3.9	4.0	4.3	4.1	4.6	4.4	4.5	4.8	4.3	4.4
$U < 1.5$ m s^{-1}	3.4%	6.6%	5.7%	5.4%	N.A.	13.1%	11.6%	11.3%	10.4%	8.6%	10.7%	7.3%	9.8%	9.3%	8.2%	9.3%	9.0%
$U > 8.0$ m s^{-1}	18.6%	18.4%	23.0%	18.7%	N.A.	1.7%	2.5%	2.9%	2.6%	5.4%	3.8%	7.1%	7.8%	8.4%	9.4%	6.1%	8.0%

[a] For water years 2000 and 2001, NEE data are excluded because the NOAA IRGA had indications of a CO_2 calibration drift (H_2O appeared ok).
[b] Missing NEE data are gap-filled using the method described in Section 3.6.
[c] The individual NEE terms are gap-filled and then the cumulative annual value for each term are added together to estimate NEE.
[d] The ad-hoc correction to the temperature term described in appendix C has been used for water years 2014, 2015, and 2016.

year^{-1} for US-GBT, -6.9 ± 12.6 g C m^{-2} year^{-1} for US-GLE (2005–2009), and -49.8 ± 10.3 g C m^{-2} year^{-1} for US-GLE (2011–2016). For the 14 years that NEE and pressure were both measured, the pressure term has a mean and standard deviation of -32.8 ± 24.5 g C m^{-2} year^{-1} while NEE has a value of -147.4 ± 231.7 g C m^{-2} year^{-1}. A negative sign for the annual pressure term means that, including the pressure term in Eq. (1), will increase NEE (positive NEE indicates that the ecosystem is a net source of CO_2 from the land to the atmosphere). The pressure term using the optimal lag compared to zero lag, increased the magnitude of the cumulative values by about 10% (Table 3).

As described in Section 3.6, the cumulative annual NEE values in Table 3 are shown using two gap-filling methods: gap-filling NEE itself and gap-filling individual NEE terms which are added together to formulate an annual NEE value. In a perfect world, these two methods would produce the same result. We found them to generally be within about 10% of each other. A better understanding of this issue is a topic worthy of dedicated study and outside the scope of the current paper.

As described by Frank et al. (2014), when healthy, the GLEES forest/ecosystem acts as a net sink of carbon from the atmosphere (NEE < 0) which is demonstrated during the US-GBT period with NEE ≈ -500 g C m^{-2} year^{-1} (Table 3). During the years when the forest was affected by the spruce beetles (2008–2011), the forest was either a weak source or sink of carbon to/from the atmosphere (Table 3). After the beetle attack and the forest was recovering (as in years 2015 and 2016) the ecosystem was a carbon sink, but with a smaller magnitude (NEE ≈ -150 g C m^{-2} year^{-1}) than that of the pre-beetle (US-GBT) forest. These dramatic changes in the carbon balance of the GLEES forest make the ratio of the pressure term to NEE (on an annual scale) vary widely from year-to-year.

How is it possible that the small pressure term at the hourly time scale can have such a significant impact on annual NEE? The primary reasons are as follows: (i) the dormant season (when daily NEE> 0) and growing season (daily NEE < 0) can cancel each other out over a full year, (ii) the pressure term is small for low winds, (iii) in high winds, the pressure term is consistently the same sign (negative) with a magnitude related to wind speed, and (iv) at the GLEES site, dormant, windy, snow-covered conditions persist for around 8 months of the year.

4.11. The impact of measurement location on the pressure term

In 2004, the pressure sensor was moved from 27.1 m above the ground on the US-GBT tower to 22.65 m on the US-GLE scaffold (a horizontal distance of about 90 m). There were important differences related to each location: (i) on the US-GLE scaffold the measurements were much closer to the surface elements (i.e., deeper within the roughness sublayer RSL), (ii) the US-GBT tower was located in the center of a small clearing while the US-GLE scaffold was within a patch of trees (Fig. S1), and (iii) the US-GBT triangular tower had a much smaller frontal surface area than the US-GLE scaffold (Fig. S2). This move occurred prior to the widespread spruce beetle attack (2007–2008), so we can assume that the forest was similar after the sensors were moved. While both towers were in place, a sonic anemometer at each location helped us evaluate the effect of the move on the wind statistics (Fig. S6). Moving the measurement location, affected the wind and pressure data in several ways.

First, and perhaps most fundamentally, the horizontal wind speed was ≈ 45% larger at US-GBT than at US-GLE (Fig. S6b) while wind shear (and turbulence) was higher at US-GLE than US-GBT. The standard deviation of the vertical wind was only 3% larger at US-GBT than US-GLE (see Section 4.2, Fig. S6a) suggesting that σ_w was less affected than the mean wind. Both measurement heights were close enough to the surface that the RSL will reduce vertical gradients in the mean wind profile (e.g., Harman and Finnigan, 2007; Shapkalijevski et al., 2017). The difference in mean wind speed between sites is further discussed in Section S4 of the supplemental material.

Second, the standard deviation of pressure σ_p approximately doubled on the US-GLE scaffold compared to US-GBT (Fig. 2c and Fig. 3a). We suggest a few possible explanations for why σ_p increased at US-GLE: (i) the US-GLE measurement level is closer to the rough, forested surface than US-GBT which leads to larger wind shear and larger angles of attack in the flow on the quad-disk producing larger dynamic pressure errors on p, (ii) a difference in the local character of the topography or surface roughness at each site, or (iii) the change from a low-profile triangular tower to a more dense scaffolding tower caused the increase in attack angles and/or distortion of the pressure field approaching the instruments (e.g., Barthelmie et al., 2016; Walker and Hedlin, 2010; Wyngaard, 1988). Note that there was a higher percentage of the 20-Hz angle of attack data outside of the optimal ± 20 degrees attack angle window (as suggested by wind tunnel tests) at the US-GLE scaffold compared to the US-GBT tower (i.e., Fig. A1). Our quad-disk in-situ tilt tests described in Appendix B, support the notion that larger attack angles lead to larger values of σ_p.

Third, despite larger σ_p at US-GLE, the magnitude of $\overline{w'p'}$ was drastically reduced at US-GLE compared to US-GBT (Fig. 2a). This appears to be an effect of the reduced wind speed at US-GLE, and in Fig. 9b it is apparent that US-GLE $\overline{w'p'}$ for years 2005–2008 falls on a similar curve as US-GBT; however, since the wind speed at US-GLE is lower the values of $\overline{w'p'}$ are smaller.

Fourth, in low wind conditions, $\overline{w'p'}$ at US-GBT was primarily negative whereas at the US-GLE scaffold there were more positive values (Fig. 2a). This difference between low-wind US-GBT and US-GLE (2005–2009) is very apparent in scaled $\overline{w'p'}$ plotted versus stability (Fig. 10e, f and discussed in Section 4.8). The reason for this different behavior in low winds is not known, but is likely related to differences in attack angle on the pressure port. Another possibility for the change in the character of $\overline{w'p'}$ is that the sensors were sampling different regions of the canopy-induced coherent structures which might lead to different characteristics of $\overline{w'p'}$. These questions, point out the need for a high resolution vertical profile of $\overline{w'p'}$ measurements.

4.12. The impact of forest structure changes on the pressure term

The spruce beetle attacks on the GLEES forest in 2007/2008 and subsequent changes to the canopy structure presented an opportunity to assess how $\overline{w'p'}$ was affected by changes to forest structure and/or distance above the roughness sublayer RSL. Different from the previous section, for the discussion here, the instruments were at a fixed location on the US-GLE scaffold and the forest properties below them changed.

As the LAI of the forest decreased, the relationship between $\overline{w'p'}$ and U changed—for a given U, the decrease in LAI increased the magnitude of $\overline{w'p'}$ by a factor of around 2 or 3. For example, for $U \approx 9$ m s^{-1} in Fig. 9b, $\overline{w'p'}$ is around -2 Pa m s^{-1} for years 2005–2009, while it is closer to -5 Pa m s^{-1} for years 2011–2016. Because there was only a single above-canopy measurement level, it is difficult for us to ascertain the reason for this change in the $\overline{w'p'}$ vs. U relationship. We suggest a few possible reasons here: (i) as the forest becomes more open, the canopy-scale coherent structures penetrate the full canopy rather than just the upper portion of the canopy, and (ii) the inflection point in the vertical wind profile might shift downward as LAI decreased, thereby shifting the vertical location and vertical scale of the coherent structures relative to the fixed measurement level.

Our study has looked at a forested site, but the effect of the pressure term should also be considered for other surface types. For example, NEE measurements from a windy alpine site suggest an annual net loss of carbon from the soil to the atmosphere (e.g., Knowles et al., 2019; 2016). If we were to apply the pressure term as-determined for the GLEES forest, it would imply that the alpine is an even larger source of carbon to the atmosphere than that shown by Knowles, et al. However, as we have shown in Fig. 10e, f, there is a large spread in the results (as well as sensitivity to LAI), and it would be reassuring to confirm the forest measurements apply to other surface types. This was also suggested by Zhang et al. (2011) who extrapolated their forest results to include grassland sites; however, the grassland measurements from McBean and Elliott (1975) are in closer agreement to our study than those of Zhang et al. (2011). Coherent structures are ubiquitous at a range of scales within the atmosphere (e.g., Barthlott et al., 2007; Hutchins et al., 2012; Träumner et al., 2015). The near-surface coherent structure dynamics over bare soil or grassland (e.g., Hommema and Adrian, 2003; Mahrt and Gibson, 1992; Schols, 1984; Sullivan et al., 2016; Wilczak and Businger, 1984) are not the same as over a forest, which suggests that additional pressure-wind measurements from grasslands and other surface types are needed to contrast the relationship between static pressure and wind at those locations compared to over a forest.

5. Summary and conclusions

We used a Nishiyama-Bedard quad-disk pressure probe coupled to a fast-response pressure transducer to calculate the covariance between turbulent static pressure and three-dimensional wind components at the windy, mountainous GLEES AmeriFlux site. Our first goal was to use the 16 years of $\overline{w'p'}$ data to improve our understanding of the mechanisms controlling the vertical wind and pressure covariance. Our second goal was to examine the effect of the pressure term on calculated net ecosystem exchange of CO_2 (NEE) from an open-path IRGA. In most NEE-related studies, the pressure term is unknown or neglected.

The magnitude of $\overline{w'p'}$ depended on mean horizontal wind speed U; however, two important events occurred during the 16-year measurement period that affected $\overline{w'p'}$. First, the measurement location, tower used, and measurement height (relative to the forest top) changed in 2004. Second, the forest surrounding the GLEES site was attacked by spruce bark beetle around 2007–2008, reducing the leaf area index LAI of the forest from around 4.7-4.9 $m^2\ m^{-2}$ in 2008 to 2.6 $m^2\ m^{-2}$ by 2011 (Frank et al., 2019). These two changes revealed that the magnitude and characteristics of $\overline{w'p'}$ are sensitive to the measurement location, as well as to changes in forest structure. The following list summarizes our findings:

(1) For $U \lesssim 6$ m s^{-1}, 30-min $\overline{w'p'}$ was slightly positive, with a value of around 0.1 Pa m s^{-1}. As U increased beyond 6 m s^{-1}, $\overline{w'p'}$ became negative reaching a value of around -3 Pa m s^{-1} for a wind speed of 8 m s^{-1} and -9 Pa m s^{-1} for wind speed around 11 m s^{-1} These values are for the open-forest time period (LAI = 2.6 $m^2\ m^{-2}$). For the denser-forest period (LAI = 4.8 $m^2\ m^{-2}$), the pattern with U was similar, however the magnitude of $\overline{w'p'}$ was about 50% smaller for a given wind speed (see Fig. 9 for details).

(2) The fairly linear relationship between the standard deviation of static pressure σ_p and U^2 proved to be a useful tool for assessing the static pressure measurements (Fig. 3a). Closer to the forest surface, the slope between σ_p and U^2 was on the order of 0.22 Pa $s^2\ m^{-2}$ while further above the forest the slope was closer to 0.07 Pa $s^2\ m^{-2}$. The smaller slope is in better agreement with previous measurements by Bedard et al. (1992) and the LES results from Patton et al. (2016). Reasons for these slope differences are discussed in Section 4.11.

(3) The phase angle between vertical wind and pressure was around 90 degrees (w leading p), which means that $\overline{w'p'}$ is sensitive to time lags between w and p (Fig. 8c). This feature of $\overline{w'p'}$ is unique compared to other scalar-wind covariances, such as heat, water vapor or CO_2 (Fig. 6) and reveals the different processes taking place. The covariance of vertical wind with temperature and CO_2 are primarily due to surface-related sinks and sources, whereas that of $\overline{w'p'}$ is related to atmospheric dynamics (i.e., coherent structures generated by the inflection point in the vertical wind profile).

(4) We considered time lags due to systematic delays within the measurement system as well as the physical separation between open-path wind and pressure sensors. For our particular system, the estimated time lag was on the order of 0.05–0.1 s; if we ignore the lag it changes the annual cumulative values of the pressure term by about 10% (Table 3). However, time lags on the order of 0.25 s can change the sign and double the magnitude of $\overline{w'p'}$ (Fig. 10). Our results show that understanding and properly applying time lags between p and w is critical for accurate measurements of $\overline{w'p'}$.

(5) The pressure measurement system did not work in calm wind conditions $U < 1.5$ m s^{-1} (see Section 4.7and Fig S10).

(6) Over an average diel cycle, the pressure term was an order of magnitude smaller than the larger NEE terms, such as the vertical wind and CO_2 density covariance, and the WPL temperature term (Fig. 11, Table 2). However, when considered as a function of U, the magnitude of the pressure term approached 0.5 μmol $m^{-2}\ s^{-1}$ for $U \approx 8$ m s^{-1} and 1.5 μmol $m^{-2}\ s^{-1}$ for $U \approx 11$ m s^{-1} (this is for LAI = 2.6 $m^2\ m^{-2}$, Fig. 12). For the denser forest (LAI = 4.8 $m^2\ m^{-2}$), the magnitude of the pressure term approached 0.25 μmol $m^{-2}\ s^{-1}$ for $U \approx 8$ m s^{-1} and 1 μmol $m^{-2}\ s^{-1}$ for $U \approx 11$ m s^{-1} (Fig. S15).

(7) In windy conditions, the pressure term increased calculated NEE, suggesting that ecosystem respiration would be underestimated if the pressure term is neglected. Including the pressure term was most significant to NEE at night or during the dormant season when ecosystem respiration dominates NEE (Fig. 12). In summer at GLEES less than 1% of 30-min periods had $U > 8$ m s^{-1} (Fig. 12a, c), so any effect of the pressure term on NEE was small.

(8) In winter, subalpine forests in the Rocky Mountains have been shown to be a small source of CO_2 to the atmosphere, with an average NEE on the order of 0.5 μmol $m^{-2}\ s^{-1}$ (e.g., Berryman et al., 2018; Burns et al., 2015; Monson et al., 2005). Our results imply that NEE would be enhanced by around 2 μmol $m^{-2}\ s^{-1}$ during high winds if the pressure term is included in the NEE calculation (Fig. 12). In contrast, CO_2 respiration fluxes through the GLEES snowpack by Berryman et al. (2018) were only enhanced by around 0.4 μmol $m^{-2}\ s^{-1}$ in high winds (Fig. 12b, d). We discuss differences between tower-based NEE and the snowpack CO_2 fluxes at the end of Section 4.9.

(9) Though we have neglected horizontal and vertical advection in our study, these are both low wind phenomena whereas the pressure term is most important during high wind periods.

(10) In-situ tests with a pair of co-located quad-disks found good agreement in σ_p (within 1%) when both quad-disks were upright and level, but σ_p increased by around 20% for a quad-disk that was tilted forward at a 22 ° angle. For $\overline{w'p'}$, the results were more

complicated and the phase between w and p was affected by the tilt (further details are in Appendix B).

(11) Over the 14 years of concurrent measurements, the pressure term had a mean and standard deviation of -32.8 ± 24.5 g C m^{-2} year^{-1} while NEE had a value of -147.4 ± 231.7 g C m^{-2} year^{-1}. This suggests that the pressure term comprised around 20% of NEE at the annual scale. However, the beetle-impacts on the GLEES forest drastically affected both the NEE (due to tree die-off) and the pressure term (due to changes in LAI). A more complete picture of the year-to-year variations is in Table 3 with discussion in Section 4.10.

Our suggestions for future pressure-wind covariance measurements are as follows: (1) measure static pressure and winds at multiple heights above and within a forest to provide insight into how different parts of the coherent structures influence $\overline{w'p'}$ (less expensive pressure sensors make this more feasible (e.g., Liberzon and Shemer, 2010; Mohr et al., 2020)) (2) a systematic way to regularly assess time lags between the wind and pressure sensors would lead to a better understanding of any temporal dependence or possible temperature effects on these lags, (3) perform a series of in-situ tilt tests (i.e., Appendix B) over flat terrain with smaller increments in the tilt angle and for longer time periods, (4) determine distortion effects on the turbulent static pressure (and wind) due to the tower structure, (5) measurements of $\overline{w'p'}$ over different surface types (e.g., bare soil, grasslands, or tundra) would lead to a better understanding of the relationship between coherent structures and $\overline{w'p'}$ for each surface type, and (6) it would be instructive to measure $\overline{w'p'}$ over a windy inert surface (such as a parking lot) to better assess the pressure term as has been done previously for the WPL terms (e.g., Ham and Heilman, 2003; Kondo and Tsukamoto, 2012). We should also note that using a closed-path IRGA minimizes/eliminates the need to include the pressure term with NEE (e.g., Nakai et al., 2011).

Important knowledge can also be educed from high-resolution LES models (such as that by Patton et al. (2016)) where the complications of measurement uncertainty and flow distortion are no longer an issue. A model-measurement synthesis of static pressure (and pressure-wind covariances) can lead to a deeper understanding of both the models and the measurements.

Declaration of Competing Interest

The authors declare that they have no known competing financial interests or personal relationships that could have appeared to influence the work reported in this paper.

Acknowledgements

The GLEES AmeriFlux site is supported by the USDA Forest Service. We are grateful for discussions with John Finnigan, Don Lenschow, Jim Wilczak, Roger Shaw, and Steve Oncley on the topic of atmospheric static pressure. Erin Berryman kindly provided the snowpack flux data. The useful comments from three anonymous reviewers are appreciated. S.P.B and P.D.B. were provided support for this work by the U.S. Department of Energy's Office of Science. E.G.P. acknowledges support for this work from the National Center for Atmospheric Research (NCAR) Geophysical Turbulence Program. NCAR is sponsored by the National Science Foundation.

Appendix A. Calculation of the system lag

To measure the system lag, an independent datalogger (with a time resolution of 0.05 s) controlled a solenoid switch which was connected to a small pressure tank. For the wind measurement, an enclosure was placed over the sonic anemometer with tubing running from the solenoid valve to one of the vertical wind transducers. The solenoid sent 22 pulses of air to the sonic, and the data logger recorded the following reaction times: 0.2 s for 13 pulses and 0.15 s for 7 pulses, giving a mean value and standard deviation of 0.18 ± 0.025 s. The same tubing was used to test the pressure sensor and the resulting delay was 0.132 ± 0.025 s. Therefore, we conclude that the pressure sensor responds approximately 0.048 s before the wind sensor. For the 20-Hz data sampling, this corresponds to a one sample difference. A similar test was done in the laboratory with the ATI datapacker and the lags were 0.113 ± 0.025 s for vertical wind and 0.037 ± 0.022 s for the Furness pressure sensor. Therefore with the ATI datapacker, pressure responded faster than wind, with a systematic lag time between them of around 0.076 s. These systematic lags were added to the spatial time lag determined by the 30-min wind speed and wind direction, creating the total time lag (Fig. S4 within the supplement) which was used for the static pressure and wind component covariance calculation.

Appendix B. Tilting of the pressure port

In wind-tunnel tests, static pressure probes are tilted to vary the angle of attack and the error in the probes is evaluated either as an absolute error, $P_{e,abs} = P_m - P_r$ where P_m and P_r are the measured and reference static pressures, respectively, or as a fractional error relative to the dynamic pressure, $P_{e,rel} = P_{e,abs} P_d^{-1}$ (Nishiyama and Bedard, 1991). Lanzinger and Schubotz (2012) compared four pressure ports in a wind tunnel and found that the Nishiyama-Bedard quad-disk performed quite well—it had less than a 1 Pa sensitivity to the flow direction approaching the probe and the sensitivity to angle of attack errors was the smallest of the four probes tested. In general, wind tunnel tests of the Nishiyama-Bedard quad-disk have shown that $P_{e,abs}$ is typically less than about 1 Pa (with $P_{e,rel}$ smaller than 1%) as long as the attack angles are within $\pm$ 20 degrees and wind speeds are less than 15 m s^{-1} (Lanzinger and Schubotz, 2012; Nishiyama and Bedard, 1991; Oncley et al., 2008). Outside of the $\pm$ 20 degrees attack angle range, the relative error rapidly grows to over -35% (Nishiyama and Bedard, 1991; Oncley et al., 2008), where a negative sign indicates that the measured static pressure is underestimated.

Because the instantaneous (i.e., 20-Hz) fluctuating angle of attack of the airflow within the upper part of the forest can often exceed angles of 20 degrees (Fig. A1), we were concerned about how these flows might affect our pressure measurements. In windy conditions, the following amounts of 20-Hz attack-angle data were outside of $\pm$ 20 degrees: $\approx$ 7% at 27.1 m on the US-GBT tower, 25% at 22.65 m on the US-GLE scaffold, and $\approx$ 50% at 6.5 m on the US-GLE scaffold (Fig. A1a1, a2). Even though we cannot account for any local surface differences between the US-GBT tower and US-GLE scaffold (i.e., such as fewer trees near the US-GBT tower), these values are consistent with the concept that being closer to the surface (or within the

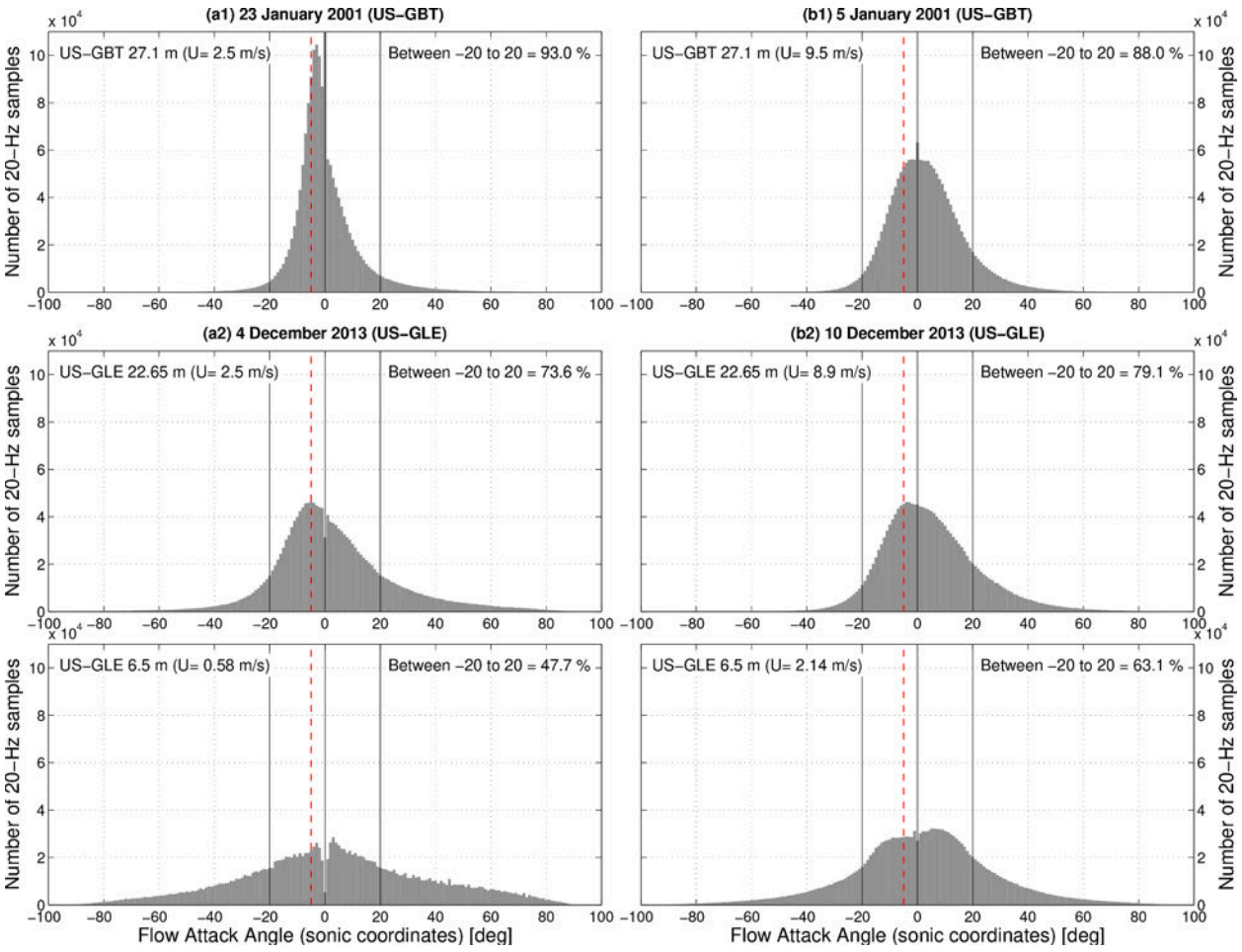

Fig. A1. Frequency distributions of 20-Hz flow angles estimated from the GLEES sonic anemometers during (left columns) low and (right columns) high winds at heights of **(a1), (b1)** 27.1 m on the US-GBT tower and **(a2), (b2)** 22.65 m and 6.5 m on the US-GLE scaffold. The bin size is 1 degree of attack angle. Each frequency distribution is from a 24-hour period for the date listed at the top of the panels and the mean wind speed over the period is shown in the upper-left corner of each panel. The vertical red-dashed line shows an angle of 5 degrees which is approximately the topographic slope at the US-GLE site. The vertical black lines are at attack angles of ± 20 degrees and the percentage of samples within that range is shown in the upper-right corner of each panel. (For interpretation of the references to color in this figure legend, the reader is referred to the web version of this article.)

canopy airspace), leads to a larger range of attack angles.

B1. Testing strategy

To perform the tests, one quad-disk was vertically mounted (relative to gravity) and fixed in place, while a second (co-located) quad-disk was periodically adjusted to different tilt angles. A digital level with 0.1 degree precision was used to set the tilt angles. Example photographs of the two

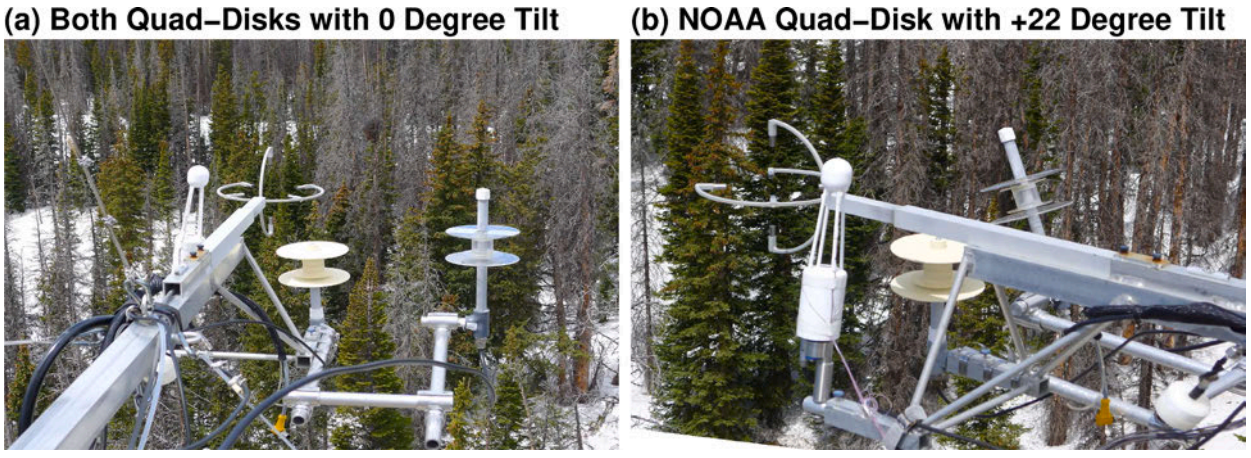

Fig. A2. Photos from 15 May 2017 when Qualimetrics and NOAA Nishiyama-Bedard quad-disk ports were co-located side-by-side for **(a)** no tilt to either port, and **(b)** with the NOAA quad-disk tilted forward at a 22 degree angle.

Table A1
A summary of the Nishiyama-Bedard quad-disk tilt tests performed at the US-GLE scaffold in 2017.

Period	Dates		Quad-Disk Tilt Angle[a]		
ID	Start	End	Qualimetrics	NOAA	Notes/Comments
					⟶ Experiment started on 25 April 2017.
1	25 April	2 May	0 (A)	0 (B)	Both quad-disks side-by-side at 22.65 m. The voltage divider for transducer A was removed.
2	2 May	15 May	0 (A)	0 (B)	Added voltage divider back to transducer A.
3	15 May	30 May	0 (A)	22 (B)	
4	30 May	13 June	0 (A)	41 (B)	
5	13 June	20 June	0 (A)	12 (B)	
6	20 June	27 June	0 (A)	−9 (B)	
7	27 June	4 July	0 (B)	0 (A)	Swapped transducers between the quad-disks.
8	4 July	11 July	N.A.	N.A.	Disconnected both quad-disks from the transducers (open tubing used as port).
9	11 July	25 July	0 (A, B)	N.A.	The Qualimetrics quad-disk was teed to both transducers.
					⟶ Experiment ended on 25 July 2017.

[a] These two columns describe the tilt angle in degrees of each of the quad-disks (one from Qualimetrics and one built for USFS by Al Bedard at NOAA). The letter in parenthesis refers to which of the two Furness FCO44 transducers the quad-disk was connected to (transducer A is SN 9301150 and transducer B is SN 950329). A positive tilt indicates the quad-disk port is tilted forward (see Fig. A2 for an example of the setup showing the positions of each quad-disk). The tilt angles listed are relative to a horizontal plane, not to the local ground surface which has a slope of around 4-6 degree.

quad-disks during the tilt tests are shown in Fig. A2. The chronology of the experiments is listed in Table A1, where each setting ran undisturbed for around 1–2 weeks. During period 1 transducer A was missing the voltage divider and for period 8 the quad-disks were disconnected from the transducers. These periods serve as extreme examples to our comparison. For the analysis, we compare the 20-Hz output from each transducer using x −y scatter plots, as well as the 30-min standard deviation of static pressure σ_p and $\overline{w'p'}$. Least-squares linear fits were used to assess the changes to the measured pressure due to tilting.

B2. Results

Before we discuss the tilt tests we present the results for three periods (1, 8, and 9) that did not involve tilting the sensors. Period 9 was when both transducers were connected to the same quad-disk, and used to determine the correction factor for transducer A of 1.98 (which is 10% larger than the transducer B value of 1.8, see the Section S2 in the supplemental material). All results presented in this section use these correction factors, and an example of the level of agreement in the 20-Hz samples is shown in Fig. S17d where the slope had a value of 0.99. In contrast, the raw 20-Hz pressure data during period 9 has a slope of 0.46 (Fig. S17c), which demonstrates how the data processing removes low-frequency differences between transducers A and B. Other statistics for period 9 are shown in Table A2.

Period 1 provides an example of raw pressure data without the voltage divider, which results in clipping of transducer A samples and a slope of 0.31 (Fig. S17a). While the clipping appears severe in Fig. S17a, only around 2.5% of the 20-Hz samples are missing. The clipping is a function of the mean wind speed and clipping-related issues are further discussed in the supplement, Section S3. Even with the clipping, the data processing still produces fairly agreeable results (Fig. S17b, slope of fit is 1.018). In contrast, when the quad-disks were removed from the transducers (period 8), the fit between transducers for the raw pressure (Fig. S17e) and the processed pressure (Fig. S17f) are almost identical and quite poor (slopes around 0.45).

Time series of the 30-min statistics for the standard deviation of static pressure σ_p, pressure and vertical wind covariance $\overline{w'p'}$, and the mean horizontal wind speed U are shown in Fig. A3. The gain (or slope) from linear fits between the co-located quad-disks are shown for the instantaneous (20-Hz) pressure measurements calculated for each 30-min period (Fig. A4a), the 30-min σ_p (Fig. A4b), and 30-min $\overline{w'p'}$ (Fig. A4c). The linear fit from

Table A2
Results from the Nishiyama-Bedard quad-disk tilt tests performed at the US-GLE scaffold in 2017. Additional details about each period are in Table A1. Statistics shown are: number of 30-min samples N, mean horizontal wind speed U, mean linear fits of the 20-Hz static pressure p (mean value ± standard deviation), the 30-min standard deviation of static pressure σ_p (mean value ± mean-squared error of residuals), and the 30-min covariance between vertical wind and pressure $\overline{w'p'}$ (mean value ± mean-squared error of residuals). Transducer A was connected to an upright quad-disk without any tilt; for all the linear fits transducer A is taken as the reference transducer. Transducer A and B used a correction factors of 1.98 and 1.8, respectively (see Section S2 in the supplement for details).

				Slopes from Linear Fits of Transducer B vs A			
Period ID	Tilt Angle	N	U [m s^{-1}]	20-Hz p	30-min σ_p	30-min $\overline{w'p'}$	Notes
1	0	50	1.59	1.01 ± 0.12	1.23 ± 0.26	0.95 ± 0.22	No voltage divider transducer A
2	0	572	2.87	0.92 ± 0.06	1.01 ± 0.00	0.82 ± 0.03	Voltage divider back to transducer A
3	22	541	3.68	0.88 ± 0.08	1.19 ± 0.97	−1.96 ± 12.7	
4	41	522	2.51	0.60 ± 0.27	1.59 ± 4.06	−0.90 ± 3.81	
5	12	114	4.61	0.85 ± 0.05	1.05 ± 0.37	−0.97 ± 71.5	
6	− 9	282	2.76	0.94 ± 0.05	1.00 ± 0.00	1.18 ± 0.05	
7	0	255	2.84	0.94 ± 0.06	1.01 ± 0.00	0.77 ± 0.10	Swapped quad-disk and transducers
8	N.A.	263	2.04	0.72 ± 0.23	0.90 ± 0.18	2.36 ± 2.00	No quad disk connected
9	0	596	2.02	0.96 ± 0.04	0.99 ± 0.00	1.10 ± 0.00	Teed to single quad-disk
				0.87 ± 0.04	0.90 ± 0.00	1.00 ± 0.00	A and B both with 1.8 correction factor

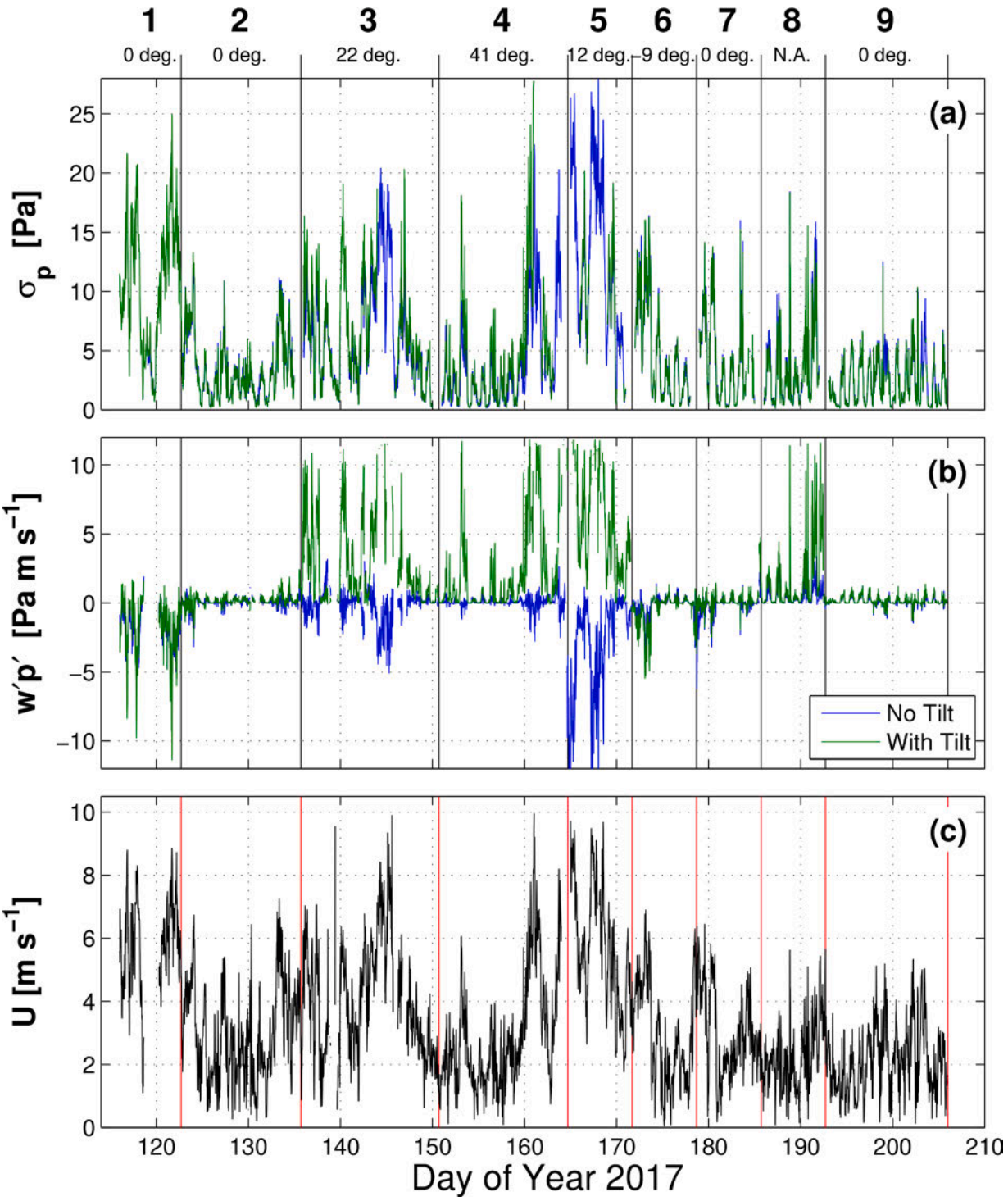

Fig. A3. Time series of 30-min values of **(a)** the standard deviation of turbulent static pressure σ_p, **(b)** the vertical wind and pressure covariance $\overline{w'p'}$, and **(c)** above-canopy mean horizontal wind speed U during the tilt tests at 22.65 m on the US-GLE scaffold. The Qualimetrics quad-disk was fixed in the vertical position (with zero tilt angle) while the NOAA quad-disk was tilted forward or backwards (see legend in panel **(b)**). The vertical lines indicate when the settings were changed (see Table A1 for details) and the time period ID and tilt angle are provided above panel **(a)**.

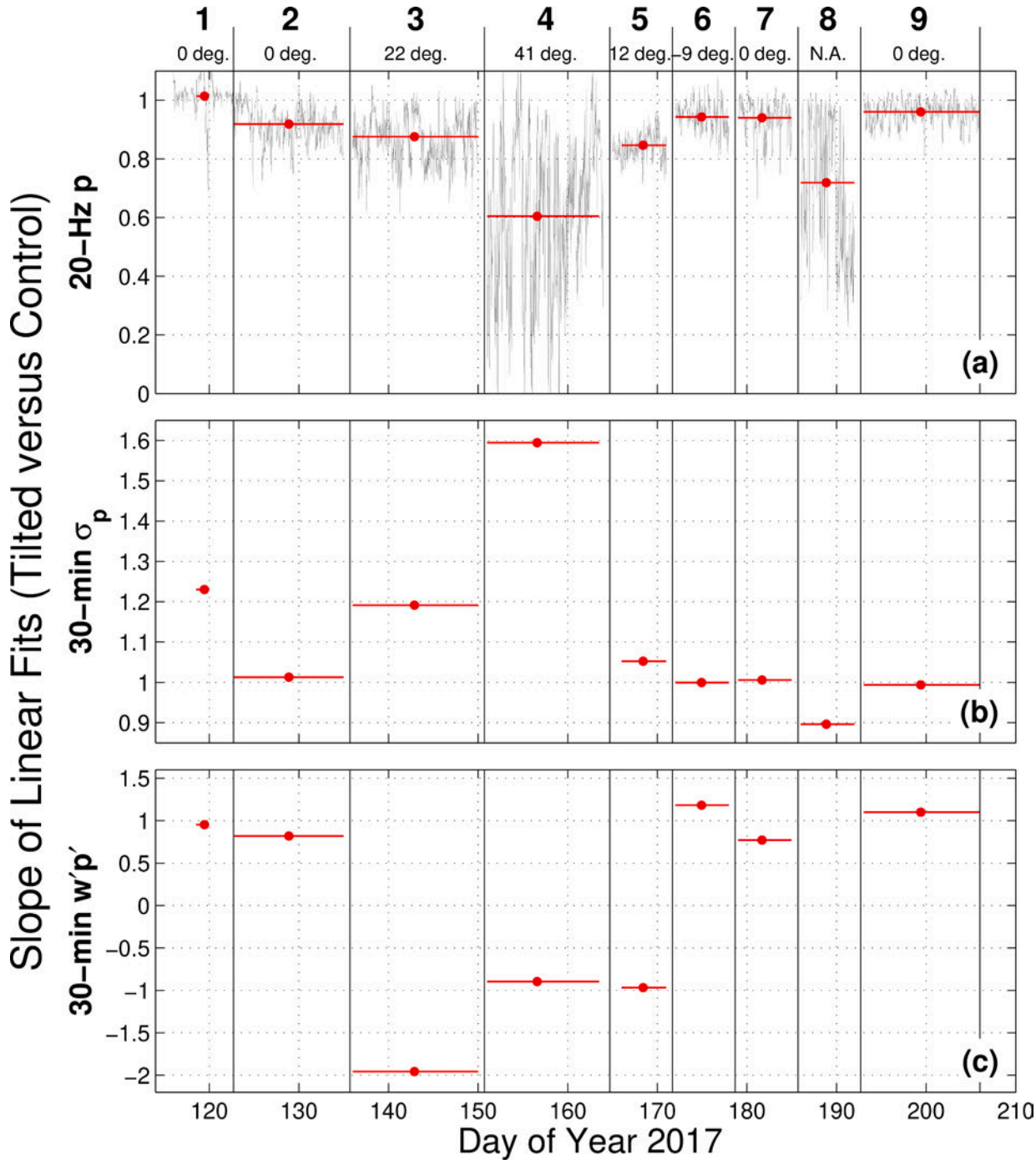

Fig. A4. Time series of linear fits between the two co-located Nishiyama-Bedard quad-disk ports of **(a)** the 20-Hz turbulent pressure p, **(b)**, the 30-min standard deviation of p σ_p, and **(c)** the 30-min vertical wind pressure covariance $\overline{w'p'}$. The vertical lines indicate when the settings were changed (see Table A1) and the time period ID and tilt angle are provided above panel **(a)**. The fit for the 20-Hz data was calculated every 30-min which is shown as the black line in **(a)**. The average values over each unique period are shown as horizontal red lines. Numerical values from this figure can be found in Table A2. (For interpretation of the references to color in this figure legend, the reader is referred to the web version of this article.)

the last two items were calculated over each unique period (1–9) and the mean-squared error of the residuals from each fit are listed in Table A2.

Next, we consider periods when both co-located quad-disks were upright (periods 2 and 7). The 20-Hz p_{raw} fit has a coefficient of 0.53 while the processed p fit has a slope of 0.93 (Fig. S18a, b). The statistics in Table A2 (and shown in Fig. A4), suggest consistent agreement for each of these periods with small variability in the 20-Hz data (period 2: 0.92±0.06, period 7: 0.94±0.06), as well for σ_p (period 2: 1.01±0.00, period 7: 1.01±0.00). In contrast, $\overline{w'p'}$, had smaller slopes from the linear fits (period 2: 0.82±0.03, period 7: 0.77±0.10), suggesting that $\overline{w'p'}$ from transducer B was about 20% smaller than those from transducer A. We should note that the quad-disks were connected to different transducers for periods 2 and 7, and the consistent results between these periods suggests that any differences in p (or $\overline{w'p'}$) are related to the transducer, not the specific quad-disk port. Furthermore, on 21 March 2017 we replaced the 22.65 m Qualimetrics quad-disk with the NOAA quad-disk, and subsequent data analysis of periods just-before and just-after the swap did not show any port-dependent effects (results not shown).

For periods when the NOAA quad-disk (connected to transducer B) was tilted we observe a dramatic effect on the slopes and increased variations for all three statistics (Fig. A4, Table A2). The increased spread in the 20-Hz samples due to tilting can be seen by comparing Fig. S18b with Figs. S18d, f where the slopes drop from 0.93 (no tilt) to 0.84 degree tilt) to 0.55 (41 degree tilt). Furthermore, for the case of a 41 degree tilt, the data processing does not improve the fit (Fig. S18e). For σ_p, the smaller tilt angles of 12 and −9 degrees suggest that tilting the quad-disk backwards (period 6, −9 degrees, slope of 1.0) leads to slightly better agreement than being tilted forward (period 5, 12 degrees, slope of 1.05). However, the tilt angles of 22 degrees (period 3, 1.19 ± 0.97) and 41 degrees (period 4, 1.59 ± 4.06) lead to increases of σ_p on the order of 20–60% with high variability. This is likely due to enhanced levels of flow separation on the tilted quad-disk causing highly unsteady, variable conditions in the air flow by the pressure ports. These results are qualitatively similar to wind tunnel results that show pressure measurement errors growing larger outside of ± 20 degrees (e.g., Lanzinger and Schubotz, 2012; Nishiyama and Bedard, 1991; Oncley et al., 2008; Woo et al., 1989).

The distortion of the $\overline{w'p'}$ statistics for a tilted quad-disk is more complex and $\overline{w'p'}$ from the tilted port becomes positive while $\overline{w'p'}$ from the upright disk is negative (Fig. A3b). This feature is apparent for tilt angles of 12 degrees, 22 degrees, and 41 degrees, but not for the angle of −9 degrees. Because $\overline{w'p'}$ between the reference and tilted transducer differ in sign, it makes the linear statistic between transducers a bit more difficult to decipher (Fig. A4c). This suggests that the phase of the $\overline{w'p'}$ measurement is highly sensitive to any tilts of the quad disk. This result could also be explained if transducer A and B had a different response time. To the best of our knowledge, both systems were setup exactly the same, but it is possible there were unknown internal differences between the transducers.

A lack of time and resources limited the duration and number of tilt angles we tested; however, our goal was to get a broad overview on the effect of tilting the quad disks on the measured static pressure and $\overline{w'p'}$. The overall conclusion from our experiments is that σ_p is enhanced by over 20% for a tilt angle of 22 degrees and $\overline{w'p'}$ is affected by tilt angles as small as 12 degrees, presumably due to the sensitivity in the phase between w and p. The impact of the 4–6 ° sloping terrain at GLEES means that the vertically-aligned quad-disks in our tests will have around a −5 degree flow angle bias in the flow attack-angle on the quad-disk. A similar side-by-side comparison over flat terrain would avoid this complication. Though our results are comparable for small tilt angles, the high-frequency fluctuations are clearly outside the ± 20 degrees attack angle range (Fig. A1), and further tests are needed to confirm how these affect $\overline{w'p'}$. Finally, since static pressure measurement errors in wind tunnels are sensitive to wind speed, we also examined the results for high and low wind speed conditions. We found that higher winds generally increased the magnitude of the errors (results not shown), however not all periods experienced high winds and we are lacking enough statistics to fully explore this aspect of the comparison.

Appendix C. Determination of an ad-hoc correction factor for the temperature term

When we initially examined the US-GLE wintertime NEE values, we found that starting around year 2014, the mean mid-day NEE was negative while the NEE values from the middle of the night remained positive (Fig. A5). During winter, subalpine forests are expected to have positive daytime and nighttime values which are approximately the same magnitude (e.g., Burns et al., 2015). According to Frank and Massman (2020), there is some level of uncertainty in the temperature term for the NEE equation. Therefore, we examined the effect of applying an ad-hoc correction to the temperature term on the winter NEE values (Fig. A6). As seen here, if the temperature term is used "as-is" the value of mid-day NEE is around 0.6 μmol m^{-2} s^{-1} while that of nocturnal NEE is −0.7 μmol m^{-2} s^{-1}. However, by applying a ad-hoc correction factor of 8% to the temperature term, the day and night NEE values come to a common value of around 0.4 μmol m^{-2} s^{-1} (i.e., where the daytime and nighttime lines cross in Fig. A6). The focus of this paper is on the pressure term; however, we deemed it appropriate to apply this simple correction to the temperature term for years 2014–2016 to obtain physically-reasonable values of wintertime NEE. In addition, the correction produces NEE values which, on average, are closer to the snowpack CO_2 fluxes described in Berryman et al. (2018) (as shown by the horizontal lines in Fig. A6). Of course, this correction could be accounting for errors related to other terms in the NEE equation. The ad-hoc corrected NEE data are shown in Fig. A5; they get used for the statistics in Tables 2 and 3 and in Figs. 11 and 12.

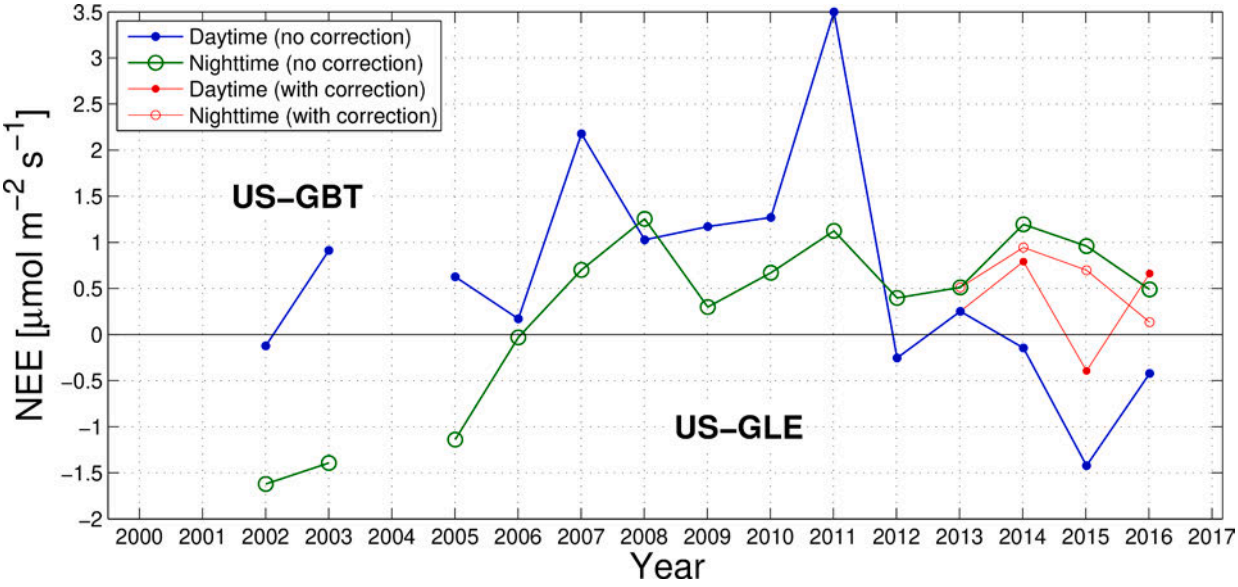

Fig. A5. The average winter (November–February) values of NEE during the daytime (10–14 MST) and nighttime (22–02 MST) where the values in red show the effect of an ad-hoc correction of 8% applied to the WPL temperature term. Measurements for years 2002 and 2003 are from the US-GLE tower; all other years are from the US-GLE scaffold. The ad-hoc correction is only used for years 2014, 2015, and 2016. (For interpretation of the references to color in this figure legend, the reader is referred to the web version of this article.)

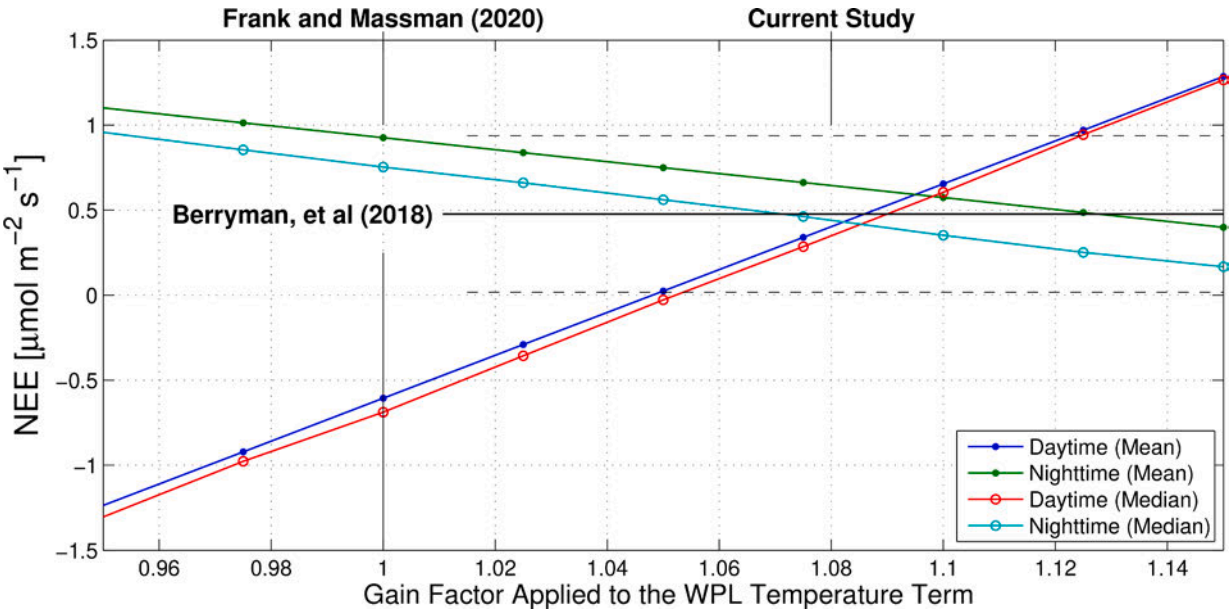

Fig. A6. The mean and median of the daytime (10–14 MST) and nighttime (22–02 MST) dormant-season NEE plotted as a function of an empirical ad-hoc correction to the WPL temperature term. The NEE data used are from between 1 November to 28 February for years 2014, 2015, and 2016. The horizontal solid line is the mean snowpack CO_2 fluxes from Berryman et al. (2018), with the horizontal dashed lines showing ± one standard deviation from the mean. The vertical lines show the value of the temperature term used by Frank and Massman (2020) and the ad-hoc correction of 8% used within the current study.

As shown in Fig. A5, the nighttime NEE was negative from the US-GBT tower and the first winter (2004–2005) at the US-GLE scaffold. This is suggestive of a problem with the NEE measurements; however, for the 2014–2016 period the ad-hoc correction was for negative *daytime* NEE, not nighttime NEE. When we attempted to use the same ad-hoc procedure on the US-GBT NEE data, it did not produce the same results and the crossing point was a negative value of NEE (rather than positive NEE as shown in Fig. A6). At US-GBT, an older LI-7500 (SN 75–0235) was used and LI-7500s from that vintage had additional errors beyond the self-heating correction, such as solar radiation and timing problems (e.g., Mauder et al., 2007). Therefore, we did not make any additional attempts to correct or better understand the US-GBT NEE data.

Supplementary material

Supplementary material associated with this article can be found, in the online version, at doi:10.1016/j.agrformet.2021.108402

References

Albertson, J.D., Katul, G.G., Parlange, M.B., Eichinger, W.E., 1998. Spectral scaling of static pressure fluctuations in the atmospheric surface layer: The interaction between large and small scales. Phys. Fluids 10, 1725–1732. https://doi.org/10.1063/1.869689.

Applied Technologies, Inc., 2016. Technical Description of a Sonic Anemometer/Thermometer (SATI Series). Rev. G, 6 pp.

Aubinet, M., Vesala, T., Papale, D., 2012. Eddy Covariance: A Practical Guide to Measurement and Data Analysis. Springer Atmospheric Sciences, Dordrecht, The Netherlands, 438 pp.. https://doi.org/10.1007/978-94-007-2351-1

Baldocchi, D.D., Hicks, B.B., Meyers, T.P., 1988. Measuring biosphere-atmosphere exchanges of biologically related gases with micrometeorological methods. Ecology 69, 1331–1340. https://doi.org/10.2307/1941631.

Baldocchi, D.D., Meyers, T.P., 1991. Trace gas-exchange above the floor of a deciduous forest: 1. evaporation and CO_2 efflux. J. Geophys. Res. 96, 7271–7285. https://doi.org/10.1029/91JD00269.

Banfield, D., Rodriguez-Manfredi, J.A., Russell, C.T., Rowe, K.M., Leneman, D., Lai, H.R., Cruce, P.R., Means, J.D., Johnson, C.L., Mittelholz, A., et al., 2019. InSight Auxiliary Payload Sensor Suite (APSS). Space Sci Rev 215, 4. https://doi.org/10.1007/s11214-018-0570-x.

Barthelmie, R.J., Wang, H., Doubrawa, P., Pryor, S.C., 2016. Best practice for measuring wind speeds and turbulence offshore through in-situ and remote sensing technologies. Technical Report to the DOE. Sibley School of Mechanical and Aerospace Engineering, College of Engineering, Cornell University, p. 47. https://doi.org/10.7298/X4QV3JGF.

Barthlott, C., Drobinski, P., Fesquet, C., Dubos, T., Pietras, C., 2007. Long-term study of coherent structures in the atmospheric surface layer. Bound.-Layer Meteor. 125, 1–24. https://doi.org/10.1007/s10546-007-9190-9.

Bedard, A.J., Georges, T.M., 2000. Atmospheric infrasound. Phys Today 53, 32–37. https://doi.org/10.1063/1.883019.

Bedard Jr., A.J., Whitaker, R.W., Greene, G.E., Mutschlecner, P., Nishiyama, R.T., Davidson, M., 1992. Measurements of Pressure Fluctuations near the Surface of the Earth. 10th Symposium on Turbulence and Diffusion, Portland, OR, September, pp. 293–296.

Benedict, R.P., 1984. Fundamentals of Temperature, Pressure, and Flow Measurements, third. John Wiley & Sons, Inc., New York, NY, 560 pp. https://doi.org/10.1002/9780470172698

Berryman, E.M., Frank, J.M., Massman, W.J., Ryan, M.G., 2018. Using a Bayesian framework to account for advection in seven years of snowpack CO_2 fluxes in a mortality-impacted subalpine forest. Agric. For. Meteor. 249, 420–433. https://doi.org/10.1016/j.agrformet.2017.11.004.

Bonan, G.B., 2008. Forests and climate change: forcings, feedbacks, and the climate benefits of forests. Science 320, 1444–1449. https://doi.org/10.1126/science.1155121.

Bowling, D.R., Massman, W.J., 2011. Persistent wind-induced enhancement of diffusive CO_2 transport in a mountain forest snowpack. J. Geophys. Res. 116, G04006. https://doi.org/10.1029/2011JG001722.

Bradford, J.B., Birdsey, R.A., Joyce, L.A., Ryan, M.G., 2008. Tree age, disturbance history, and carbon stocks and fluxes in subalpine Rocky Mountain forests. Global Change Biol. 14, 2882–2897. https://doi.org/10.1111/j.1365-2486.2008.01686.x.

Bradshaw, P., Koh, Y.M., 1981. A note on Poisson's equation for pressure in a turbulent flow. Physics Of Fluids 24. https://doi.org/10.1063/1.863442.777–777

Bunce, A., Volin, J.C., Miller, D.R., Parent, J., Rudnicki, M., 2019. Determinants of tree sway frequency in temperate deciduous forests of the Northeast United States. Agric. For. Meteor. 266–267, 87–96. https://doi.org/10.1016/j.agrformet.2018.11.020.

Burba, G., Schmidt, A., Scott, R.L., Nakai, T., Kathilankal, J., Fratini, G., Hanson, C., Law, B., McDermitt, D.K., Eckles, R., Furtaw, M., Velgersdyk, M., 2012. Calculating CO_2 and H_2O eddy covariance fluxes from an enclosed gas analyzer using an instantaneous mixing ratio. Global Change Biol. 18, 385–399. https://doi.org/10.1111/j.1365-2486.2011.02536.x.

Burba, G.G., McDermitt, D.K., Grelle, A., Anderson, D.J., Xu, L.K., 2008. Addressing the influence of instrument surface heat exchange on the measurements of CO_2 flux from open-path gas analyzers. Global Change Biol. 14, 1854–1876. https://doi.org/10.1111/j.1365-2486.2008.01606.x.

Burns, S.P., Blanken, P.D., Turnipseed, A.A., Hu, J., Monson, R.K., 2015. The influence of warm-season precipitation on the diel cycle of the surface energy balance and carbon

dioxide at a Colorado subalpine forest site. Biogeosciences 12, 7349–7377. https://doi.org/10.5194/bg-12-7349-2015.
Burns, S.P., Frank, J.M., Massman, W.J., Patton, E.G., Blanken, P.D., 2017. Static pressure-wind covariance and coherent structures at two subalpine forest sites. FLUXNET Conference 2017. Berkeley, CA. 7–9 June.
Burns, S.P., Sun, J., Oncley, S.P., Turnipseed, A.A., Yi, C., Lenschow, D.H., Monson, R.K., 2006. An evaluation of in-canopy flux measurements. Flux Measurements in Difficult Conditions, a Specialist Workshop by ILEAPS. International Geosphere-Biosphere Programme, Boulder, CO, 26–28 January, Poster.
Chu, H., Baldocchi, D.D., Poindexter, C., Abraha, M., Desai, A.R., Bohrer, G., Arain, M.A., Griffis, T., Blanken, P.D., O'Halloran, T.L., Thomas, R.Q., Zhang, Q., Burns, S.P., Frank, J.M., Christian, D., Brown, S., Black, T.A., Gough, C.M., Law, B.E., Lee, X., Chen, J., Reed, D.E., Massman, W.J., Clark, K., Hatfield, J., Prueger, J., Bracho, R., Baker, J.M., Martin, T.A., 2018. Temporal dynamics of aerodynamic canopy height derived from eddy covariance momentum flux data across North American flux networks. Geophys Res Lett 45, 9275–9287. https://doi.org/10.1029/2018GL079306.
R.M. Young Company, 2001. Model 61202V Barometric Pressure Sensor. 3 pp.
Cuxart, J., Morales, G., Terradellas, E., Yague, C., 2002. Study of coherent structures and estimation of the pressure transport terms for the nocturnal stable boundary layer. Bound.-Layer Meteor. 105, 305–328. https://doi.org/10.1023/A:1019974021434.
Dupont, S., Patton, E.G., 2012. Momentum and scalar transport within a vegetation canopy following atmospheric stability and seasonal canopy changes: The CHATS experiment. Atmos. Chem. Phys 12, 5913–5935. https://doi.org/10.5194/acp-12-5913-2012.
Dwyer, M.J., Patton, E.G., Shaw, R.H., 1997. Turbulent kinetic energy budgets from a large-eddy simulation of airflow above and within a forest canopy. Bound.-Layer Meteor. 84, 23–43. https://doi.org/10.1023/A:1000301303543.
Elliott, J.A., 1972. Microscale pressure fluctuations measured within lower atmospheric boundary layer. J. Fluid Mech. 53, 351–383. https://doi.org/10.1017/S0022112072000199.
Finnigan, J.J., 2000. Turbulence in plant canopies. Annu. Rev. Fluid Mech. 32, 519–571. https://doi.org/10.1146/annurev.fluid.32.1.519.
Finnigan, J.J., Clement, R., Malhi, Y., Leuning, R., Cleugh, H.A., 2003. A re-evaluation of long-term flux measurement techniques. Part I: Averaging and coordinate rotation. Bound.-Layer Meteor. 107, 1–48. https://doi.org/10.1023/A:1021554900225.
Finnigan, J.J., Shaw, R.H., Patton, E.G., 2009. Turbulence structure above a vegetation canopy. J. Fluid Mech. 637, 387–424. https://doi.org/10.1017/S0022112009990589.
Frank, J.M., Massman, W.J., 2020. A new perspective on the open-path infrared gas analyzer self-heating correction. Agric. For. Meteor. 290, 107986. https://doi.org/10.1016/j.agrformet.2020.107986.
Frank, J.M., Massman, W.J., Ewers, B.E., Huckaby, L.S., Negron, J.F., 2014. Ecosystem CO_2/H_2O fluxes are explained by hydraulically limited gas exchange during tree mortality from spruce bark beetles. J. Geophys. Res. 119, 1195–1215. https://doi.org/10.1002/2013JG002597.
Frank, J.M., Massman, W.J., Ewers, B.E., Williams, D.G., 2019. Bayesian analyses of 17 winters of water vapor fluxes show bark beetles reduce sublimation. Water Resour. Res. 55, 1598–1623. https://doi.org/10.1029/2018WR023054.
Fuehrer, P.L., Friehe, C.A., 2002. Flux corrections revisited. Bound.-Layer Meteor. 102, 415–457. https://doi.org/10.1023/A:1013826900579.
Furness Controls Limited, 2008. FCO44 Differential Pressure Transducer Users Guide, Issue 4. 7 pp.
George, W.K., Beuther, P.D., Arndt, R.E.A., 1984. Pressure spectra in turbulent free shear flows. J. Fluid Mech. 148, 155–191. https://doi.org/10.1017/S0022112084002299.
Gossard, E.E., Hooke, W.H., 1975. Waves in the atmosphere: Atmospheric infrasound and gravity waves – their generation and propagation. Developments in Atmospheric Science, vol. 2. Elsevier Scientific.456 pp.
Ham, J.M., Heilman, J.L., 2003. Experimental test of density and energy-balance corrections on carbon dioxide flux as measured using open-path eddy covariance. Agron J 95, 1393–1403. https://doi.org/10.2134/agronj2003.1393.
Harman, I.N., Finnigan, J.J., 2007. A simple unified theory for flow in the canopy and roughness sublayer. Bound.-Layer Meteor. 123, 339–363. https://doi.org/10.1007/s10546-006-9145-6.
Haslwanter, A., Hammerle, A., Wohlfahrt, G., 2009. Open-path vs. closed-path eddy covariance measurements of the net ecosystem carbon dioxide and water vapour exchange: A long-term perspective. Agric. For. Meteor. 149, 291–302. https://doi.org/10.1016/j.agrformet.2008.08.011.
Hedlin, M.A.H., Walker, K., Drob, D.P., de Groot-Hedlin, C.D., 2012. Infrasound: Connecting the solid earth, oceans, and atmosphere. Annu. Rev. Earth Planet. Sci. 40, 327–354. https://doi.org/10.1146/annurev-earth-042711-105508.
Holland, J.Z., 1989. On pressure-driven wind in deep forests. J. Appl. Meteor. 28, 1349–1355. https://doi.org/10.1175/1520-0450(1989)028<1349:OPDWID>2.0.CO;2.
Hommema, S.E., Adrian, R.J., 2003. Packet structure of surface eddies in the atmospheric boundary layer. Bound.-Layer Meteor. 106, 147–170. https://doi.org/10.1023/A:1020868132429.
Horst, T.W., Lenschow, D.H., 2009. Attenuation of scalar fluxes measured with spatially-displaced sensors. Bound.-Layer Meteor. 130, 275–300. https://doi.org/10.1007/s10546-008-9348-0.
Hristov, T.S., 2008. Correcting distortions in measurements of atmospheric pressure fluctuations. Bound.-Layer Meteor. 129, 497–507. https://doi.org/10.1007/s10546-008-9322-x.
Huang, J.P., Lee, X.H., Patton, E.G., 2008. A modelling study of flux imbalance and the influence of entrainment in the convective boundary layer. Bound.-Layer Meteor. 127, 273–292. https://doi.org/10.1007/s10546-007-9254-x.
Hutchins, N., Chauhan, K., Marusic, I., Monty, J., Klewicki, J., 2012. Towards reconciling the large-scale structure of turbulent boundary layers in the atmosphere and laboratory. Bound.-Layer Meteor. 145, 273–306. https://doi.org/10.1007/s10546-012-9735-4.
Ibrom, A., Dellwik, E., Larsen, S.E., Pilegaard, K., 2007. On the use of the Webb-Pearman-Leuning theory for closed-path eddy correlation measurements. Tellus Series B-Chemical And Physical Meteorology 59, 937–946. https://doi.org/10.1111/j.1600-0889.2007.00311.x.
Jonker, H.J.J., Duynkerke, P.G., Cuijpers, J.W.M., 1999. Mesoscale fluctuations in scalars generated by boundary layer convection. J. Atmos. Sci. 56, 801–808. https://doi.org/10.1175/1520-0469(1999)056<0801:MFISGB>2.0.CO;2.
Kaimal, J.C., 1978. Sonic anemometer measurement of atmospheric turbulence. In: Hansen, B.W. (Ed.), Proceedings of the Dynamic Flow Conference 1978 on Dynamic Measurements in Unsteady Flows. Springer Netherlands, Dordrecht, pp. 551–565. https://doi.org/10.1007/978-94-009-9565-9_29.
Kaimal, J.C., Izumi, Y., Wyngaard, J.C., Coté, R., 1972. Spectral characteristics of surface-layer turbulence. Quart. J. Roy. Meteor. Soc. 98, 563–589. https://doi.org/10.1002/qj.49709841707.
Kataoka, T., Mitsuta, Y., Tsukamoto, O., 1989. The development of a fast response static pressure instrument for field use. J. Meteor. Soc. Japan 67, 351–357. https://doi.org/10.2151/jmsj1965.67.3_351.
Katul, G.G., Albertson, J.D., Hsieh, C.-I., Conklin, P.S., Sigmon, J.T., Parlange, M.B., Knoerr, K.R., 1996. The "inactive" eddy motion and the large-scale turbulent pressure fluctuations in the dynamic sublayer. J. Atmos. Sci. 53, 2512–2524. https://doi.org/10.1175/1520-0469(1996)053<2512:TEMATL>2.0.CO;2.
Knowles, J.F., Blanken, P.D., Lawrence, C.R., Williams, M.W., 2019. Evidence for non-steady-state carbon emissions from snow-scoured alpine tundra. Nat Commun 10, 1306. https://doi.org/10.1038/s41467-019-09149-2.
Knowles, J.F., Blanken, P.D., Williams, M.W., 2016. Wet meadow ecosystems contribute the majority of overwinter soil respiration from snow-scoured alpine tundra. J. Geophys. Res. 121, 1118–1130. https://doi.org/10.1002/2015JG003081.
Kondo, F., Tsukamoto, O., 2012. Experimental validation of WPL correction for CO_2 flux by eddy covariance technique over the asphalt surface. J. Agric. Meteorol. 68, 183–194. https://doi.org/10.2480/agrmet.68.4.1.
Kowalski, A.S., Serrano-Ortiz, P., 2007. On the relationship between the eddy covariance, the turbulent flux, and surface exchange for a trace gas such as CO_2. Bound.-Layer Meteor. 124, 129–141. https://doi.org/10.1007/s10546-007-9171-z.
Laemmel, T., Mohr, M., Longdoz, B., Schack-Kirchner, H., Lang, F., Schindler, D., Maier, M., 2019. From above the forest into the soil - How wind affects soil gas transport through air pressure fluctuations. Agric. For. Meteor. 265, 424–434. https://doi.org/10.1016/j.agrformet.2018.11.007.
Lanzinger, E., Schubotz, K., 2012. A laboratory intercomparison of static pressure heads. Technical Conference on Meteorological and Environmental Instruments and Methods of Observation (TECO-2012), World Meteorological Organization. Brussels, Belgium, 16–18 October.P1(15), URL: https://www.wmo.int/pages/prog/www/CIMO/cimo-teco-meteorex.html
Le Pichon, A., Blanc, E., Hauchecorne, A., 2010. Infrasound Monitoring for Atmospheric Studies. Springer Netherlands, Dordrecht, 735 pp.. https://doi.org/10.1007/978-1-4020-9508-5
Lee, X., 1997. Gravity waves in a forest: A linear analysis. J. Atmos. Sci. 54, 2574–2585. https://doi.org/10.1175/1520-0469(1997)054<2574:GWIAFA>2.0.CO;2.
Lenschow, D.H., Sun, J., 2007. The spectral composition of fluxes and variances over land and sea out to the mesoscale. Bound.-Layer Meteor. 125, 63–84. https://doi.org/10.1007/s10546-007-9191-8.
Leuning, R., Judd, M.J., 1996. The relative merits of open- and closed-path analysers for measurement of eddy fluxes. Global Change Biol. 2, 241–253. https://doi.org/10.1111/j.1365-2486.1996.tb00076.x.
Leuning, R., Moncrieff, J., 1990. Eddy-covariance CO_2 flux measurements using open- and closed-path CO_2 analyzers: corrections for analyzer water-vapor sensitivity and damping of fluctuations in air sampling tubes. Bound.-Layer Meteor. 53, 63–76. https://doi.org/10.1007/BF00122463.
LI-COR Inc., 2004. LI-7500 CO_2/H_2O Analyzer Instruction Manual. Publication Number 984–06360, Revision 4, 155 pp., (Available at www.licor.com).
Liberzon, D., Shemer, L., 2010. An inexpensive method for measurements of static pressure fluctuations. J. Atmos. Oceanic Technol. 27, 776–784. https://doi.org/10.1175/2009JTECHA1352.1.
Mahrt, L., Gibson, W., 1992. Flux decomposition into coherent structures. Bound.-Layer Meteor. 60, 143–168. https://doi.org/10.1007/BF00122065.
Massman, W., 2004. Concerning the measurement of atmospheric trace gas fluxes with open- and closed-path eddy covariance system: the WPL terms and spectral attenuation. In: Lee, X., Massman, W., Law, B. (Eds.), Handbook of Micrometeorology, Atmospheric and Oceanographic Sciences Library, Vol. 29. Springer Netherlands, pp. 133–160. https://doi.org/10.1007/1-4020-2265-4_7.
Massman, W., Clement, R., 2004. Uncertainty in eddy covariance flux estimates resulting from spectral attenuation. In: Lee, X., Massman, W., Law, B. (Eds.), Handbook of Micrometeorology, Atmospheric and Oceanographic Sciences Library, Vol. 29. Springer Netherlands, pp. 67–99. https://doi.org/10.1007/1-4020-2265-4_4.
Massman, W.J., 2000. A simple method for estimating frequency response corrections for eddy covariance systems. Agric. For. Meteor. 104, 185–198. https://doi.org/10.1016/S0168-1923(00)00164-7.
Massman, W. J., Frank, J. M., 1991–2006. Data and Information for the AmeriFlux GLEES Brooklyn Tower Site (US-GBT), AmeriFlux Management Project, Lawrence Berkeley National Laboratory, California. doi:10.17190/AMF/1375200.
Massman, W. J., Frank, J. M., 2004–present. Data and Information for the AmeriFlux GLEES Scaffold Site (US-GLE), AmeriFlux Management Project, Lawrence Berkeley National Laboratory, California. doi:10.17190/AMF/1246056.

Massman, W.J., Lee, X., 2002. Eddy covariance flux corrections and uncertainties in long term studies of carbon and energy exchanges. Agric. For. Meteor. 113, 121–144. https://doi.org/10.1016/S0168-1923(02)00105-3.

Massman, W.J., Sommerfeld, R.A., Mosier, A.R., Zeller, K.F., Hehn, T.J., Rochelle, S.G., 1997. A model investigation of turbulence-driven pressure-pumping effects on the rate of diffusion of CO_2, N_2O, and CH_4 through layered snowpacks. J. Geophys. Res. 102, 18851–18863. https://doi.org/10.1029/97JD00844.

Mauder, M., Oncley, S.P., Vogt, R., Weidinger, T., Ribeiro, L., Bernhofer, C., Foken, T., Kohsiek, W., De Bruin, H.A.R., Liu, H., 2007. The energy balance experiment EBEX-2000. Part II: Intercomparison of eddy-covariance sensors and post-field data processing methods. Bound.-Layer Meteor. 123, 29–54. https://doi.org/10.1007/s10546-006-9139-4.

McBean, G.A., Elliott, J.A., 1975. The vertical transports of kinetic energy by turbulence and pressure in the boundary layer. J. Atmos. Sci. 32, 753–766. https://doi.org/10.1175/1520-0469(1975)032<0753:TVTOKE>2.0.CO;2.

McBean, G.A., Elliott, J.A., 1978. Energy budgets of turbulent velocity components and velocity-pressure gradient interactions. J. Atmos. Sci. 35, 1890–1899. https://doi.org/10.1175/1520-0469(1978)035<1890:TEBOTT>2.0.CO;2.

Mohr, M., Laemmel, T., Maier, M., Schindler, D., 2016. Analysis of air pressure fluctuations and topsoil gas concentrations within a scots pine forest. Atmosphere (Basel) 7. https://doi.org/10.3390/atmos7100125.

Mohr, M., Laemmel, T., Maier, M., Schindler, D., 2020. Inexpensive high-precision system for measuring air pressure fluctuations. Meteorol. Appl. 27, e1815. https://doi.org/10.1002/met.1815.

Monson, R.K., Burns, S.P., Williams, M.W., Delany, A.C., Weintraub, M., Lipson, D.A., 2006. The contribution of beneath-snow soil respiration to total ecosystem respiration in a high-elevation, subalpine forest. Global Biogeochem. Cycle 20, GB3030. https://doi.org/10.1029/2005GB002684.

Monson, R.K., Sparks, J.P., Rosenstiel, T.N., Scott-Denton, L.E., Huxman, T.E., Harley, P. C., Turnipseed, A.A., Burns, S.P., Backlund, B., Hu, J., 2005. Climatic influences on net ecosystem CO_2 exchange during the transition from wintertime carbon source to springtime carbon sink in a high-elevation, subalpine forest. Oecologia 146, 130–147. https://doi.org/10.1007/s00442-005-0169-2.

Musselman, R.C., 1994. The Glacier lakes ecosystem experiments site. Technical Report, RM-249. USDA Forest Service, Rocky Mountain Forest and Range Experiment Station.94 pp.

Nakai, T., Iwata, H., Harazono, Y., 2011. Importance of mixing ratio for a long-term CO_2 flux measurement with a closed-path system. Tellus Series B-Chemical And Physical Meteorology 63, 302–308. https://doi.org/10.1111/j.1600-0889.2011.00538.x.

Nieveen, J.P., El-Kilani, R.M.M., Jacobs, A.F.G., 2001. Behaviour of the static pressure around a tussock grassland-forest interface. Agric. For. Meteor. 106, 253–259. https://doi.org/10.1016/S0168-1923(00)00234-3.

Nishiyama, R.T., Bedard, A.J., 1991. A "quad-disk" static pressure probe for measurement in adverse atmospheres: With a comparative review of static pressure probe designs. Rev. Sci. Instrum. 62, 2193–2204. https://doi.org/10.1063/1.1142337.

Oncley, S.P., Massman, W.J., Patton, E.G., 2008. Turbulent pressure fluctuations measured during CHATS. 18th Symposium on Boundary Layers and Turbulence. Stockholm, Sweeden. American Meteorological Society.18A.3, URL: http://n2t.net/ark:/85065/d7js9pjw

Patton, E.G., Horst, T.W., Sullivan, P.P., Lenschow, D.H., Oncley, S.P., Brown, W.O.J., Burns, S.P., Guenther, A.B., Held, A., Karl, T., Mayor, S.D., Rizzo, L.V., Spuler, S.M., Sun, J., Turnipseed, A.A., Allwine, E.J., Edburg, S.L., Lamb, B.K., Avissar, R., Calhoun, R.J., Kleissl, J., Massman, W.J., Paw U, K.T., Weil, J.C., 2011. The Canopy Horizontal Array Turbulence Study. Bull. Amer. Meteor. Soc. 92, 593–611. https://doi.org/10.1175/2010BAMS2614.1.

Patton, E.G., Katul, G.G., 2009. Turbulent pressure and velocity perturbations induced by gentle hills covered with sparse and dense canopies. Bound.-Layer Meteor. 133, 189–217. https://doi.org/10.1007/s10546-009-9427-x.

Patton, E.G., Sullivan, P.P., Shaw, R.H., Finnigan, J.J., Weil, J.C., 2016. Atmospheric stability influences on coupled boundary layer and canopy turbulence. J. Atmos. Sci. 73, 1621–1647. https://doi.org/10.1175/JAS-D-15-0068.1.

Polonik, P., Chan, W.S., Billesbach, D.P., Burba, G., Li, J., Nottrott, A., Bogoev, I., Conrad, B., Biraud, S.C., 2019. Comparison of gas analyzers for eddy covariance: effects of analyzer type and spectral corrections on fluxes. Agric. For. Meteor. 272–273, 128–142. https://doi.org/10.1016/j.agrformet.2019.02.010.

Raspet, R., Abbott, J.P., Webster, J., Yu, J., Talmadge, C., Aberts II, K., Collier, S., Noble, J., 2019. New systems for wind noise reduction for infrasonic measurements. In: Le Pichon, A., Blanc, E., Hauchecorne, A. (Eds.), Infrasound Monitoring for Atmospheric Studies: Challenges in Middle Atmosphere Dynamics and Societal Benefits. Springer International Publishing, Dordrecht, The Netherlands, pp. 91–124. https://doi.org/10.1007/978-3-319-75140-5_3.

Raupach, M.R., 1987. A Lagrangian analysis of scalar transfer in vegetation canopies. Quart. J. Roy. Meteor. Soc. 113, 107–120. https://doi.org/10.1002/qj.49711347507.

Raupach, M.R., Finnigan, J.J., Brunet, Y., 1996. Coherent eddies and turbulence in vegetation canopies: the mixing-layer analogy. Bound.-Layer Meteor. 78, 351–382. https://doi.org/10.1007/BF00120941.

Raupach, M.R., Thom, A.S., 1981. Turbulence in and above plant canopies. Annu. Rev. Fluid Mech. 13, 97–129. https://doi.org/10.1146/annurev.fl.13.010181.000525.

Rossow, V.J., 1991. Probe systems for static pressure and cross-stream turbulence intensity. J. Aircraft 28, 750–755. https://doi.org/10.2514/3.46092.

Schols, J.L.J., 1984. The detection and measurement of turbulent structures in the atmospheric surface. Bound.-Layer Meteor. 29, 39–58. https://doi.org/10.1007/BF00119118.

Schols, J.L.J., Wartena, L., 1986. A dynamical description of turbulent structures in the near neutral surface layer: The role of static pressure fluctuations. Bound.-Layer Meteor. 34, 1–15. https://doi.org/10.1007/BF00120905.

Shapkalijevski, M.M., Ouwersloot, H.G., Moene, A.F., Vilà-Guerau de Arellano, J., 2017. Integrating canopy and large-scale effects in the convective boundary-layer dynamics during the CHATS experiment. Atmos. Chem. Phys 17, 1623–1640. https://doi.org/10.5194/acp-17-1623-2017.

Shaw, R.H., Paw U, K.T., Zhang, X.J., Gao, W., Den Hartog, G., Neumann, H.H., 1990. Retrieval of turbulent pressure fluctuations at the ground surface beneath a forest. Bound.-Layer Meteor. 50, 319–338. https://doi.org/10.1007/BF00120528.

Shaw, R.H., Zhang, X.J., 1992. Evidence of pressure-forced turbulent flow in a forest. Bound.-Layer Meteor. 58, 273–288. https://doi.org/10.1007/BF02033828.

Sigmon, J.T., Knoerr, K.R., Shaughnessy, E.J., 1983. Microscale pressure fluctuations in a mature deciduous forest. Bound.-Layer Meteor. 27, 345–358. https://doi.org/10.1007/BF02033744.

Speckman, H.N., Frank, J.M., Bradford, J.B., Miles, B.L., Massman, W.J., Parton, W.J., Ryan, M.G., 2015. Forest ecosystem respiration estimated from eddy covariance and chamber measurements under high turbulence and substantial tree mortality from bark beetles. Glob Chang Biol 21, 708–721. https://doi.org/10.1111/gcb.12731.

Subramanian, G.K., Muschinski, A., 2011. First observations of microbaroms with single absolute barometers. J. Atmos. Oceanic Technol. 28, 933–943. https://doi.org/10.1175/2011JTECHA1526.1.

Sullivan, P.P., Weil, J.C., Patton, E.G., Jonker, H.J.J., Mironov, D.V., 2016. Turbulent winds and temperature fronts in large-eddy simulations of the stable atmospheric boundary layer. J. Atmos. Sci. 73, 1815–1840. https://doi.org/10.1175/JAS-D-15-0339.1.

Takle, E.S., Massman, W.J., Brandle, J.R., Schmidt, R.A., Zhou, X., Litvina, I.V., Garcia, R., Doyle, G., Rice, C.W., 2004. Influence of high-frequency ambient pressure pumping on carbon dioxide efflux from soil. Agric. For. Meteor. 124, 193–206. https://doi.org/10.1016/j.agrformet.2004.01.014.

Tennekes, H., Lumley, J.L., 1972. A First Course in Turbulence. MIT Press, Cambridge, MA. 300 pp.

Träumner, K., Damian, T., Stawiarski, C., Wieser, A., 2015. Turbulent structures and coherence in the atmospheric surface layer. Bound.-Layer Meteor. 154, 1–25. https://doi.org/10.1007/s10546-014-9967-6.

Vickers, D., Mahrt, L., 2003. The cospectral gap and turbulent flux calculations. J. Atmos. Oceanic Technol. 20, 660–672. https://doi.org/10.1175/1520-0426(2003)20<660:TCGATF>2.0.CO;2.

Vilà-Guerau de Arellano, J., Gioli, B., Miglietta, F., Jonker, H.J.J., Baltink, H.K., Hutjes, R.W.A., Holtslag, A.A.M., 2004. Entrainment process of carbon dioxide in the atmospheric boundary layer. J. Geophys. Res. 109, D18110. https://doi.org/10.1029/2004JD004725.

Walker, K.T., Hedlin, M.A., 2010. A review of wind-noise reduction methodologies. In: Le Pichon, A., Blanc, E., Hauchecorne, A. (Eds.), Infrasound Monitoring for Atmospheric Studies. Springer Atmospheric Sciences, Dordrecht, The Netherlands, pp. 141–182. https://doi.org/10.1007/978-1-4020-9508-5_5.

Wang, W., Xu, J., Gao, Y., Bogoev, I., Cui, J., Deng, L., Hu, C., Liu, C., Liu, S., Shen, J., Sun, X., Xiao, W., Yuan, G., Lee, X., 2016. Performance evaluation of an integrated open-path eddy covariance system in a cold desert environment. J. Atmos. Oceanic Technol. 33, 2385–2399. https://doi.org/10.1175/JTECH-D-15-0149.1.

Webb, E.K., Pearman, G.I., Leuning, R., 1980. Correction of flux measurements for density effects due to heat and water vapour transfer. Quart. J. Roy. Meteor. Soc. 106, 85–100. https://doi.org/10.1002/qj.49710644707.

Wilczak, J.M., Bedard, A.J., 2004. A new turbulence microbarometer and its evaluation using the budget of horizontal heat flux. J. Atmos. Oceanic Technol. 21, 1170–1181. https://doi.org/10.1175/1520-0426(2004)021<1170:ANTMAI>2.0.CO;2.

Wilczak, J.M., Businger, J.A., 1984. Large-scale eddies in the unstably stratified atmospheric boundary layer. Part II: Turbulent pressure fluctuations and the budgets of heat flux, stress and turbulent kinetic energy. J. Atmos. Sci. 41, 3551–3567. https://doi.org/10.1175/1520-0469(1984)041<3551:LSEITU>2.0.CO;2.

Wilczak, J.M., Oncley, S.P., Bedard Jr., A.J., 1992. Turbulent pressure fluctuations in the atmospheric surface layer. 10th Symposium on Turbulence and Diffusion, Portland, OR, September, pp. 167–170.

Wilczak, J.M., Oncley, S.P., Stage, S.A., 2001. Sonic anemometer tilt correction algorithms. Bound.-Layer Meteor. 99, 127–150. https://doi.org/10.1023/A:1018966204465.

Woo, H.G.C., Cermak, J.E., Peterka, J.A.P., 1989. Calibration of atmospheric pressure sensor quad-disk probe. Technical Report, No. CER89-90HGCW-JEC-JAP7. Fluid Dynamics and Diffusion Laboratory, Department of Civil Engineering, Colorado State University.44 pp.

Wyngaard, J.C., 1988. The effects of probe-induced flow distortion on atmospheric turbulence measurements: Extension to scalars. J. Atmos. Sci. 45, 3400–3412. https://doi.org/10.1175/1520-0469(1988)045<3400:TEOPIF>2.0.CO;2.

Wyngaard, J.C., Siegel, A., Wilczak, J.M., 1994. On the response of a turbulent-pressure probe and the measurement of pressure transport. Bound.-Layer Meteor. 69, 379–396. https://doi.org/10.1007/BF00718126.

Zeller, K., Zimmerman, G., Hehn, T., Donev, E., Denny, D., Welker, J., 2001. Analysis of inadvertent microprocessor lag time on eddy covariance results. J. Appl. Meteor. 40, 1640–1646. https://doi.org/10.1175/1520-0450(2001)040<1640:AOIMLT>2.0.CO;2.

Zeller, K.F., Nikolov, N.T., 2000. Quantifying simultaneous fluxes of ozone, carbon dioxide and water vapor above a subalpine forest ecosystem. Environ. Pollut. 107, 1–20. https://doi.org/10.1016/S0269-7491(99)00156-6.

Zhang, J., Lee, X., Song, G., Han, S., 2011. Pressure correction to the long-term measurement of carbon dioxide flux. Agric. For. Meteor. 151, 70–77. https://doi.org/10.1016/j.agrformet.2010.09.004.

Zhuang, Y., Amiro, B.D., 1994. Pressure fluctuations during coherent motions and their effects on the budgets of turbulent kinetic energy and momentum flux within a forest canopy. J. Appl. Meteor. 33, 704–711. https://doi.org/10.1175/1520-0450(1994)033<0704:PFDCMA>2.0.CO;2.